

*Copyright © and Moral Rights for this thesis and, where applicable, any accompanying data are retained by the author and/or other copyright owners. A copy can be downloaded for personal non-commercial research or study, without prior permission or charge. This thesis and the accompanying data cannot be reproduced or quoted extensively from without first obtaining permission in writing from the copyright holder/s. The content of the thesis and accompanying research data (where applicable) must not be changed in any way or sold commercially in any format or medium without the formal permission of the copyright holder/s.*

*Thesis: Alexander Petrov (2020) “Multiphysics Finite Element Modelling of the AC Power Loss, Fault Response and Recovery of First Generation Superconducting Cables”, University of Southampton, Electronics and Computer Science, PhD Thesis, pagination.*

*Data: Alexander Petrov (2020) Data and COMSOL files supporting a PhD thesis in multiphysics finite element modelling of superconducting cables.*

<https://doi.org/10.5258/SOTON/D1461>

**University of Southampton**

Faculty of Engineering and Physical Sciences

Electronics and Computer Science

**Multiphysics Finite Element Modelling of the AC Power Loss, Fault  
Response and Recovery of First Generation Superconducting Cables**

by

**Alexander Petrov**

ORCID ID 0000-0003-4820-5227

Thesis for the Degree of Doctor of Philosophy

July 20, 2020



University of Southampton

Abstract

Faculty of Engineering and Physical Sciences  
Electronics and Computer Science

Thesis for the Degree of Doctor of Philosophy

Multiphysics Finite Element Modelling of the AC Power Loss, Fault Response and  
Recovery of First Generation Superconducting Cables

by Alexander Petrov

The fault response of superconducting cables is of significant importance to their wider adoption in power grids. In particular, it is useful to understand how to most efficiently and accurately simulate the fault response and time of recovery after a high through fault overcurrent. To achieve that, rigorous modeling techniques must be established, which is done over several steps. A successful numerical model of magnetic field dependent behaviour of a Bi-2223 superconducting tape has been demonstrated. This model has been used to redefine and verify a homogenization technique for multifilamentary tapes that decreases the computation time by simplifying the geometry with a minimum to no accuracy penalty. Afterwards, the simulation of AC power losses in twisted tapes and cables is investigated, with reference models coming from literature and custom-built 3D models. The investigation produced methods to efficiently estimate the losses of multi-layer twisted in 2D FEM without resorting to 3D. Finally by capitalizing on the techniques established prior, a multiphysics model is built — electro-magneto-thermal — in three different space domains in order to simulate the AC losses, temperature and heat transfer in all important cable components. It is shown this type of complex multiphysics model can be set up to run and may produce fairly accurate results. One FEM simulation of the multiphysics model takes no more than 3 days to complete on a standard PC.



# Contents

<b>List of Figures</b>	<b>vii</b>
<b>List of Tables</b>	<b>ix</b>
<b>Declaration of Authorship</b>	<b>xi</b>
<b>Acknowledgements</b>	<b>xiii</b>
<b>Nomenclature</b>	<b>xvii</b>
<b>List of Abbreviations</b>	<b>xx</b>
<b>1 Introduction</b>	<b>1</b>
<b>2 Theory of high temperature superconductors</b>	<b>5</b>
2.1 Brief theory of superconductivity . . . . .	5
2.2 Overview of superconducting materials for power applications . . . . .	8
2.2.1 1st Generation HTS – Bi-2223 and Bi-2221 . . . . .	9
2.2.2 2nd Generation HTS – YBCO . . . . .	10
2.2.3 $MgB_2$ . . . . .	11
2.2.4 Low temperature superconductors . . . . .	11
2.2.5 Why use HTS and not LTS? . . . . .	11
2.3 AC power loss mechanisms and their calculation . . . . .	12
<b>3 Literature review</b>	<b>13</b>
3.1 Chronological review of previous research into the simulation of overcurrent and fault response of HTS cables . . . . .	13
3.2 Overview and research questions . . . . .	18
3.3 Existing techniques for homogenization of multifilamentary tapes . . . . .	20
3.4 Existing techniques for estimating the losses in twisted tapes and cables . . . . .	21
<b>4 Numerical modelling of superconducting tapes using the finite element method</b>	<b>23</b>
4.1 Physics . . . . .	23
4.1.1 The Power Law . . . . .	23
4.1.2 Electromagnetics . . . . .	28
4.2 Implementation of 2D physics within COMSOL with focus on tapes . . . . .	30
4.2.1 H-formulation . . . . .	30
4.2.2 AC losses . . . . .	33
4.3 Verification of physics models . . . . .	34
4.3.1 Single filament, Bi-2223, Ag-sheathed tape . . . . .	34
4.3.2 Multifilamentary, Bi-2223, Ag-sheathed tape . . . . .	39

<b>5</b>	<b>The homogeneous multifilamentary domain</b>	<b>43</b>
5.1	Proposed homogenization technique . . . . .	44
5.2	2D verification of the homogenization technique . . . . .	45
5.2.1	61-filament, Bi-2223, Ag-sheathed tape — Amemiya <i>et al</i> . . . . .	46
5.2.2	55-filament, Bi-2223, Ag-sheathed tape — Choi <i>et al</i> . . . . .	52
5.2.3	Circular multi-tape conductors — Ryu <i>et al</i> . . . . .	53
5.3	The homogenization technique at currents above critical current . . . . .	57
5.3.1	Equivalent circuit modelling of a superconducting cable . . . . .	57
5.3.2	Verification of the homogenization technique for a single layer HTS cable subjected to currents above the critical current . . . . .	60
5.4	Summary . . . . .	63
<b>6</b>	<b>Estimation of power loss in twisted multi-layer Bi-2223 cables via 2D modelling</b>	<b>65</b>
6.1	Method for estimation of the power loss . . . . .	65
6.1.1	Method description . . . . .	65
6.1.2	Handling the critical current density's dependence of the magnetic field in twisted tapes in 2D and 3D . . . . .	68
6.1.3	Notes on layer twist . . . . .	69
6.2	Method verification . . . . .	70
6.2.1	Construction of sample 3D cables . . . . .	70
6.2.2	Construction of a 2D model based on a real cable . . . . .	72
6.2.3	Results analysis . . . . .	75
6.3	Summary . . . . .	79
<b>7</b>	<b>Transient fault simulations using COMSOL</b>	<b>81</b>
7.1	Further modelling theory . . . . .	82
7.1.1	Modelling of the fault current waveform . . . . .	82
7.1.2	Heat transfer in solids . . . . .	83
7.1.3	Heat transfer in fluids . . . . .	83
7.1.4	1D fluid flow approximation . . . . .	84
7.2	The AmpaCity cable . . . . .	84
7.3	Temperature profile of the AmpaCity cable . . . . .	85
7.3.1	Modelling of the coolant . . . . .	86
7.3.2	Modelling of the temperature along the total width and length of the cable . . . . .	90
7.3.3	Coupling of the coolant and cable body heat transfer physics . . . . .	92
7.3.4	Simulation of the steady state . . . . .	93
7.4	Overcurrent response of the AmpaCity cable . . . . .	94
7.4.1	Construction of the 3-phase cable and physics . . . . .	95
7.4.2	Equivalent resistance and temperature dependencies . . . . .	96
7.4.3	Solving for the duration of the fault . . . . .	99
7.4.4	Temperature distribution within the 2D-axisymmetric model . . . . .	101
7.5	Recovery of the AmpaCity cable . . . . .	104
7.5.1	Very little or no current during recovery . . . . .	106
7.5.2	Large current during recovery . . . . .	108
7.6	Summary . . . . .	110
<b>8</b>	<b>Conclusion</b>	<b>111</b>
	<b>References</b>	<b>115</b>

# List of Figures

1.1	A flowchart with an overview of the final model . . . . .	4
2.1	E-J characteristic of HTS . . . . .	8
2.2	First generation multifilamentary conductor, produced from Bi-2223 superconducting material (dark filaments) and filled with Ag or similar . . .	9
2.3	First generation multifilamentary conductor, produced from Bi-2212 superconducting material and filled with Ag or similar . . . . .	9
2.4	Second generation composite conductor, produced from REBCO . . . . .	10
2.5	Cross-sections of a MgB <sub>2</sub> wires . . . . .	11
2.6	The cross-section of most common LTS . . . . .	12
3.1	Structure of a Triax cable (1) . . . . .	14
3.2	Structure of a Triax cable (2) . . . . .	15
3.3	An electro-thermal coupled simulation program flowchart . . . . .	16
3.4	Photograph of an HTS cable . . . . .	17
3.5	The three options for spatial design of 3-phase HTS cables . . . . .	19
4.1	Power law resistivity and damped resistivity — comparison . . . . .	24
4.2	Spatial definitions for the 2D FEM model. . . . .	25
4.3	Spatial definitions for the 2D FEM model. . . . .	34
4.4	The 50x20 nodes mesh used for all simulations of the single filament . . .	35
4.5	Comparison between the simulated AC transport losses and the numerical results of Nibbio <i>et al</i> . . . . .	36
4.6	Comparison between the simulated AC transport losses in a DC magnetic field and the numerical results of Nibbio <i>et al</i> . . . . .	37
4.7	Comparison between the simulated and experimental values of the magnetization AC losses in perp. magnetic field without any transp. current .	37
4.8	Comparison between the experimental AC losses by Nibbio and those simulated for an applied AC magnetic field with a transp. current . . . .	38
4.9	The geometry of the multifilamentary tape used in verifications . . . . .	39
4.10	The mesh used in the case of multifilamentary tape, used in verifications .	39
4.11	Comparison between the measured values in Amemiya <i>et al</i> and those plotted with Equation 4.12, with $\beta = 1$ and $\gamma = 0.15$ . . . . .	40
4.12	Comparison between the simulated and measured values of the AC losses under applied transport current for a range of $i$ . . . . .	41
4.13	Comparison between the simulated and measured values of the AC losses in AC magnetic field . . . . .	42
4.14	Zoomed-in comparison between the simulated and measured values of the AC losses in parallel magnetic field for $i = 0.9$ and $i = 0.1$ . . . . .	42
5.1	The micrograph and homogenized model of Amemiya <i>et al</i> . . . . .	44



5.2	Comparison between mesh densities in Amemiya, as in Table 5.2 . . . . .	46
5.3	Micrographs of the tapes, by Amemiya and Choi . . . . .	47
5.4	Magnetic field dependency of $J_c$ measured by literature (Amemiya) . . . . .	47
5.5	Comparison between AC transport losses in Amemiya and simulations . . . . .	48
5.6	Predicted AC total losses in the Amemiya tape in applied external field . . . . .	49
5.7	Comparison between the current densities in the homogenized and multifilamentary model of Amemiya's tape . . . . .	50
5.8	Magnetic field dependency of $J_c$ measured by literature (Choi) . . . . .	51
5.9	Comparison between the AC transport losses in Choi and the simulations . . . . .	53
5.10	Magnetic field dependency of $J_c$ measured by literature (Ryu) . . . . .	54
5.11	The cross-section of the configuration of the 10-tape conductor . . . . .	54
5.12	Measured and simulated (original) AC losses in Ryu-A and Ryu-B . . . . .	56
5.13	The equivalent circuit arrangement of the MATLAB model. . . . .	57
5.14	The symmetry arrangement of the COMSOL model. . . . .	60
5.15	Simulation results of the homogenized model and the calculation of the analytical model with constant critical current. . . . .	62
5.16	Simulation results of the numerical models with interpolated magnetic field dependent critical current . . . . .	62
5.17	Simulation time of the homogenization and reference multifilamentary COMSOL model with field-dependent critical current . . . . .	62
6.1	An illustration of the difference between $I_t$ and $I_{t-2D}$ . . . . .	66
6.2	Visual description of the modification of the tape's width . . . . .	67
6.3	Illustration of the cross-section types used for approximating losses . . . . .	67
6.4	Illustration of the relationship between $H_{m-x}$ and $H_{m-y}$ . . . . .	69
6.5	Illustration of the twist and meshing of the two layers in Cable 2. . . . .	71
6.6	The two cross-section types as applied to the 2D cable . . . . .	73
6.7	The simulated AC losses from the 3D models and the 2D models . . . . .	74
6.8	Displaying the location of the points in Figure 6.9 . . . . .	75
6.9	$J$ at three points on the same position within a tape (cross-section) . . . . .	76
6.10	Current density at twelve points within the the twelve tapes . . . . .	77
6.11	Average magnetic field magnitude within the HTS material of all tapes . . . . .	78
6.12	The direction of current flow in Cable 3 . . . . .	78
6.13	Simulated total AC losses in the 2D cable, compared with measurements . . . . .	79
7.1	Circuit diagram of a power system under short circuit fault . . . . .	82
7.2	The AmpaCity cable . . . . .	85
7.3	The geometry of the physics in the 1D coolant simulation . . . . .	88
7.4	The geometry of the physics in the total width and length of the cable . . . . .	91
7.5	The coupling of the coolant and body temperatures . . . . .	93
7.6	The steady-state temperature along the AmpaCity cable . . . . .	94
7.7	The 2D cross-section including boundary conditions . . . . .	96
7.8	The simulated full and limited fault currents in the AmpaCity model . . . . .	100
7.9	The temperature distribution in each phase along the AmpaCity length (1) . . . . .	103
7.10	The temperature distribution in each phase along the AmpaCity length (2) . . . . .	104
7.11	The temperature recovery in each phase along the AmpaCity length . . . . .	105
7.12	The temperature recovery in the coolant along the AmpaCity length . . . . .	107
7.13	Estimated losses against temperature . . . . .	108
7.14	How the second phase drives re-quench . . . . .	108
7.15	Temperature over time, current applied at 20 s . . . . .	109
7.16	Temperature over time, current applied at 60 s . . . . .	109

# List of Tables

4.1	Different formulations utilized to solve Maxwell's equations . . . . .	28
4.2	Parameters for single filament verification . . . . .	35
4.3	Parameters for multifilamentary verification . . . . .	39
4.4	Properties of a filament for the multifilamentary verification . . . . .	40
5.1	Parameters for the tape by Amemiya <i>et al</i> . . . . .	48
5.2	Time and degrees of freedom required in simulations of the homogenized and multifilamentary model in Amemiya and Choi with transport current equal to the critical current, in self-field. * - the numbers are the same, which is coincidental and not an error. . . . .	49
5.3	Parameters for the tape by Choi <i>et al</i> . . . . .	52
5.4	Parameters for the tapes by Ma <i>et al</i> and Ryu <i>et al</i> . . . . .	55
5.5	Specification of the sample cable construction. . . . .	61
6.1	Specifications of the 3D cables used in verifying the 2D approximation method . . . . .	70
6.2	Specification of the real 2D cable used in verifying the 2D approximation method . . . . .	72
7.1	Geometric specification of the AmpaCity cable . . . . .	86
7.2	Operational specification of the AmpaCity cable . . . . .	87
7.3	Parameters of the corrugated tube in the AmpaCity cable . . . . .	87
7.4	Thermal parameters of the materials of the AmpaCity cable . . . . .	87



## Declaration of Authorship

Print name: ALEXANDER PETROV

Title of thesis: Multiphysics Finite Element Modelling of the AC Power Loss, Fault Response and Recovery of First Generation Superconducting Cables

I declare that this thesis and the work presented in it are my own and has been generated by me as the result of my own original research.

I confirm that:

1. This work was done wholly or mainly while in candidature for a research degree at this University;
2. Where any part of this thesis has previously been submitted for a degree or any other qualification at this University or any other institution, this has been clearly stated;
3. Where I have consulted the published work of others, this is always clearly attributed;
4. Where I have quoted from the work of others, the source is always given. With the exception of such quotations, this thesis is entirely my own work;
5. I have acknowledged all main sources of help;
6. Where the thesis is based on work done by myself jointly with others, I have made clear exactly what was done by others and what I have contributed myself;
7. Parts of this work have been published as:
  - (a) A. N. Petrov, J. A. Pilgrim, and I. O. Golosnoy, "Revisiting the homogenized domain model for fast simulation of AC transport power losses in first generation high temperature superconducting tapes and cables," *Physica C: Superconductivity and its Applications*, vol. 557, pp. 33-40, 2019/02/15/2019.
  - (b) A. N. Petrov, J. A. Pilgrim, and I. O. Golosnoy, "2D finite element modelling of the AC transport power loss in multi-layer Bi-2223 cables," *Journal of Physics: Conference Series*, vol. 1559, p. 012134, 2020/06 2020.

Signature:

Date: July 20, 2020



## Acknowledgements

Firstly, I would like to thank the University of Southampton for the opportunity to conduct research on a postgraduate level. I would also like to thank my supervisors Dr James Pilgrim and Dr Igor Golosnoy who have continuously provided helpful guidance and have been readily available when I needed it.

There are two other people besides my supervisors who had assisted me directly with my thesis. Thank you go to Dr George Callender for discussion and assistance regarding the meshing in areas with large heat gradient. Also special thanks to Dr Wesley Tiago Batista de Sousa from the Karlsruhe Institute of Technology for helpful discussions and for generously providing his research parameters on top of what is published in literature.

Finally, thank you to my parents Albena and Nickolay for everything they have done for me, particularly while on the path towards university. For being there for me despite the distance, thank you to all of my friends (whose names I will not enumerate in fear of missing someone). Thank you also to my girlfriend Michaela who endured me when I was stressed and provided much needed support. I love you all.



Do not go gentle into that good night.  
Rage, rage against the dying of the light.

— Dylan Thomas





# Nomenclature

$A$	Magnetic vector potential (Wb/m)
$A_c$	Hydraulic cross-sectional area (m <sup>2</sup> )
$A_s$	Hydraulic cross-sectional area of the supply flow channel (m <sup>2</sup> )
$A_r$	Hydraulic cross-sectional area of the return flow channel (m <sup>2</sup> )
$A_t$	Area of the tape's cross-section (m <sup>2</sup> )
$A_{hom}$	Area of the tape's homogenized domain (m <sup>2</sup> )
$A_{Ag}$	Area of the tape's actual matrix (silver) material (m <sup>2</sup> )
$A_{hts}$	Area of the tape's actual superconducting material (m <sup>2</sup> )
$A_k$	Cross-sectional area of phase k (2D-axisymmetric)(m <sup>2</sup> )
$B$	Magnetic field (T)
$B_{c2}$	Upper critical magnetic field (T)
$B_0$	Kim-Anderson parameter, such that $J_c(B_0) = J_{c0}/2$ (T)
$B_x$	Perpendicular (along $x$ -axis) component of the magnetic field (T)
$B_{\perp}$	Same as $B_x$ (T)
$B_y$	Parallel (along $y$ -axis) component of the magnetic field (T)
$B_{\parallel}$	Same as $B_y$ (T)
$B_{ext}$	Total external magnetic field (T)
$B_{\perp,max}$	Maximum (peak) value of the perpendicular applied magnetic field (T)
$C_p$	Specific heat capacity (J/kgK)
$C_{p,ln}$	Specific heat capacity of the liquid nitrogen (J/kgK)
$C_{p,hts}$	Specific heat capacity of the superconductor (J/kgK)
$C_{p,Ag}$	Specific heat capacity of the silver matrix (J/kgK)
$C_{p,con}$	Effective specific heat capacity of the monoblock (J/kgK)
$C_{p,hom}$	Effective specific heat capacity of the homogenized domain (J/kgK)
$c_k$	Layer circumference taken through the middle of the phase (m)
$d$	Hydraulic diameter (m)
$d_s$	Hydraulic diameter of the supply flow (m)
$d_r$	Hydraulic diameter of the return flow (m)
$E$	Electric field (V/m)
$E_c$	Electric field at the critical current criterion (V/m)
$f$	Frequency of AC current/magnetic field (Hz)
$F_s$	Corrugated pipe surface factor (m <sup>2</sup> /m)
$H$	Magnetic field strength (A/m)
$H_c$	Critical magnetic field strength (A/m)
$H_{c1}$	Lower critical magnetic field strength (A/m)
$H_{c2}$	Upper critical magnetic field strength (A/m)
$h_t$	Tape thickness (m)
$H_{m-x}$	Local parallel component of the magnetic field (A/m)
$H_{m-y}$	Local perpendicular component of the magnetic field (A/m)
$h_s$	Heat transfer coefficient for the supply flow (W/(m <sup>2</sup> K))

---

$h_r$	Heat transfer coefficient for the return flow (W/(m <sup>2</sup> K))
$h_s^*$	Modified heat transfer coefficient of the supply flow (W/(m <sup>2</sup> K))
$i$	Normalized current, $i = I_{transport}/I_c$ (A)
$I_c$	Critical current (A)
$I_{transport}$	Applied transport current (A)
$I_{c0}$	Critical current at self-field and temperature of 77 K (A)
$I_{t-2D}$	Peak applied current in a 2D cross-section of a twisted tape (A)
$I_k$	Instantaneous current flowing in each phase (A)
$J$	Current density (J/m <sup>2</sup> )
$J_c$	Critical current density (J/m <sup>2</sup> )
$J_{c0}$	Critical current density at self-field and temperature of 77 K (J/m <sup>2</sup> )
$J_n$	Normal current density/the vector sum of all current components (J/m <sup>2</sup> )
$k$	Thermal conductivity (W/mK)
$k_{ln}$	Thermal conductivity of the liquid nitrogen (W/mK)
$k_{hts}$	Thermal conductivity of the superconductor (W/mK)
$k_{Ag}$	Thermal conductivity of the silver matrix (W/mK)
$L_{grid}$	Inductance of the upstream power grid ( $\Omega$ )
$L_{HTS}$	Inductance of the superconducting cable ( $\Omega$ )
$l$	Cable model length (m)
$l_{dz}$	Length of each section in the cable model (m)
$l_k$	Actual length of each phase k=1;2;3 (m)
$n$	Power index (dimensionless)
$n_0$	Power index at self-field and temperature of 77 K (dimensionless)
$n_s$	Superelectron density
$P_c$	Hydraulic perimeter (m)
$P_{r-o}$	Perimeter of the inner cryostat wall (m)
$P_{r-i}$	Perimeter of the wall between the cable and the return flow (m)
$P_s$	Perimeter of the wall between the cable and the supply flow (m)
$Pr$	Prandtl's number (dimensionless)
$p_k$	Pitch length of each phase k=1;2;3 (m)
$Q_h$	Hysteresis (magnetization) AC loss (W/m <sup>3</sup> )
$Q_e$	Eddy current AC loss (W/m <sup>3</sup> )
$q$	Heat energy intake from neighbouring domains (J)
$Q_{leak}$	Heat lost through the cryostat of the cable (W/m)
$q_{leak}$	The heat flux lost through the cryostat of the cable (W/m <sup>2</sup> )
$q_{r-i}$	Heat flux crossing between the cable wall and the return flow (W/m <sup>2</sup> )
$q_s$	Heat flux crossing between the cable wall and the supply flow (W/m <sup>2</sup> )
$Q_{k,y}$	Heat generated in the c-section at a length y for phase k (W/m)
$Q_{k,axi}$	Heat generated along the cable length in each phase k (W/m <sup>3</sup> )
$R_{grid}$	Resistance of the upstream power grid ( $\Omega$ )
$R_{HTS}$	Resistance of the superconducting cable ( $\Omega$ )
$r_s$	Outer radius of former (m)
$r_{r-i}$	Inner radius of annular LN <sub>2</sub> channel (m)
$R_{r-o}$	Inner radius of cryostat (m)
$Re$	Reynolds number (dimensionless)
$Re_s$	Reynolds number of the supply flow (dimensionless)
$Re_r$	Reynolds number of the return flow (dimensionless)
$R_{k,hts}$	Average resistance/metre of the cable's HTS, k – phase ( $\Omega/m$ )
$R_{k,Ag}$	Average resistance/metre of the cable's Ag, k – phase ( $\Omega/m$ )
$R_k$	The resistance of each phase k=1;2;3 ( $\Omega$ )

$R_{k,tot}$	The total resistance in phase k including the cable and the grid ( $\Omega$ )
$S$	The surface on which the transport current is applied ( $m^2$ )
$S_{eq}$	Area of the filamentary-equivalent domain ( $m^2$ )
$S_{HTS}$	Area of a tape taken from a perpendicular cross-section ( $m^2$ )
$s_s$	Former (corrugated pipe) wall thickness (m)
$s_{hts}$	Fraction of superconductor in the tape's cross-section (dimensionless)
$s_{hom,ag}$	Fraction of silver within the homogenized domain (dimensionless)
$t$	Time (s)
$T$	Temperature (K)
$T$	Current vector potential (A/m)
$T_c$	Critical temperature (K)
$T_{LN_2}$	Temperature of liquid nitrogen (K)
$t_{gr}$	Former (corrugated pipe) groove depth (tube width) (m)
$T_s$	Temperature of the supply flow of liquid nitrogen (K)
$T_r$	Temperature of the return flow of liquid nitrogen (K)
$T_{wall,s}$	Temperature of the cable wall touching the supply flow (K)
$T_{wall,r}$	Temperature of the cable wall touching the return flow (K)
$T_{ln,s}$	Temperature of the liquid nitrogen in the supply flow (K)
$T_{ln,r}$	Temperature of the liquid nitrogen in the return flow (K)
$T_0$	Temperature of the cable in the 2D-axisymmetric model (K)
$T_{0(wall,i)}$	Temperature of the cable wall touching the supply flow (K)
$T_{0(wall,o)}$	Temperature of the cable wall touching the return flow (K)
$T_{LN_2}$	The reference temperature for critical current calculations (K)
$T_{hts}$	Temperature of the HTS material (2D cross-section) (K)
$T_{Ag}$	Temperature of the silver (2D cross-section) (K)
$T_{s,k}$	Temperature of the supply flow at length k (m)
$T_{r,k}$	Temperature of the return flow at length k (m)
$V$	Voltage (V)
$V_t$	Volume of interest ( $m^3$ )
$V_s$	Voltage source (circuit) (V)
$v$	Fluid velocity (m/s)
$v_s$	Coolant velocity in the supply flow (m/s)
$v_r$	Coolant velocity in the return flow (m/s)
$V_{s,k}$	Instantaneous supply voltage for each phase k=1;2;3 (V)
$w_s$	Filamentary-equivalent (superconducting) domain width (m)
$w_t$	Tape width (m)
$w_{t-2D}$	Width of the tape taken from a perpendicular cross-section (m)
$Z$	Impedance ( $\Omega$ )
$Z_{load}$	Steady-state load impedance ( $\Omega$ )
$\alpha$	Twist angle (rad)
$\rho_n$	Resistivity of the superconductor in normal state ( $\Omega m$ )
$\gamma$	Anisotropy factor (dimensionless)
$\beta$	Rapidity of reduction of $J_c$ (dimensionless)
$\sigma$	Conductivity (S/m)
$\sigma_{sc}$	Conductivity of superconductor (S/m)
$\sigma_{Ag}$	Conductivity of silver (S/m)
$\sigma_{fc}$	Flux creep conductivity (S/m)
$\Phi$	Electric scalar potential (V)
$\phi_r$	Angle of rotation (rad)
$\omega$	Magnetic scalar potential (H)

---

$\rho$	Resistivity ( $\Omega\text{m}$ )
$\mu$	Total magnetic permeability, $\mu = \mu_0\mu_r$ (H/m)
$\mu_0$	Magnetic permeability of free space (H/m)
$\mu_r$	Relative permeability (dimensionless)
$\nu_{LN_2}$	Viscosity of liquid nitrogen (Pa s)
$\rho_0$	Thermally activated flux flow resistance ( $\Omega\text{m}$ )
$\rho_{silver}$	Resistivity of silver ( $\Omega\text{m}$ )
$\rho_{ff}$	Flux flow resistivity (S/m)
$\rho_v$	Mass density ( $\text{kg}/\text{m}^3$ )
$\rho_{v,ln}$	Mass density of the liquid nitrogen ( $\text{kg}/\text{m}^3$ )
$\rho_{v,hts}$	Mass density of the superconductor ( $\text{kg}/\text{m}^3$ )
$\rho_{v,Ag}$	Mass density of the silver matrix ( $\text{kg}/\text{m}^3$ )
$\rho_{v,con}$	Effective mass density of the monoblock ( $\text{kg}/\text{m}^3$ )
$\rho_{v,hom}$	Effective mass density of the homogenized domain ( $\text{kg}/\text{m}^3$ )
$\rho_{v,ln}$	Mass density of liquid nitrogen ( $\text{kg}/\text{m}^3$ )
$\rho_{hts}$	Resistivity of the superconducting material ( $\Omega\text{m}$ )
$\rho_{plaw}$	Resistivity of the HTS material as defined by the power law ( $\Omega\text{m}$ )
$\rho_{hom}$	Resistivity of the mixed material within the homogenized domain ( $\Omega\text{m}$ )
$\rho_{Ag}$	Resistivity of the matrix (silver) material ( $\Omega\text{m}$ )
$\rho_n$	Normal state resistivity ( $\Omega\text{m}$ )
$\rho_{k,hts,ave}$	Avg. value of the resistivity within the homog. domain, k – phase ( $\Omega\text{m}$ )
$\rho_{k,Ag,ave}$	Avg. value of the resistivity within the silver material, k – phase ( $\Omega\text{m}$ )
$\lambda_{fr}$	Fraction of superconductor in the elementary region (dimensionless)

# List of Abbreviations

AC	alternating current;
BCS	Bardeen, Cooper, Schreiffer theory of superconductivity;
Bi-2223	see BSCCO;
BSCCO	Bismuth-Strontium-Calcium-Copper-Oxide, a type of material that is a high temperature superconductor;
CEPRI	China Electric Power Research Institute;
CFD	computational fluid dynamics;
CPU	central processing unit;
CSM	critical state model;
DC	direct current;
FEM	finite element model/modelling;
GB	gigabyte;
HTS	high temperature superconductor;
HTSC	high temperature superconducting cable;
IEEE	Institute of Electrical and Electronics Engineers;
IOP	Institute of Physics;
KIT	Karlsruhe Institute of Technology;
LIPA	Long Island Power Authority;
LN	liquid nitrogen;
LTS	low temperature superconductor;
MV	medium voltage;
ODE	ordinary differential equation;
PC	personal computer;
PDE	partial differential equation;
PPLP	Polypropylene Laminated Paper;
RAM	random access memory;
REBCO	Rare-Earth-Barium-Carbon-Oxide, a family of materials that are high temperature superconductors;
RL	resistor-inductor pair;
RMS	root mean squared;
TWh	terawatt hour;
YBCO	Yttrium-Barium-Carbon-Oxide, a type of material that is a high temperature superconductor;



# Chapter 1

## Introduction

An unavoidable power engineering problem is that all conducting materials possess inherent resistivity. Consecutively, the flow of current through power transmission and distribution lines produces Ohmic losses. In 2015, the House of Commons Energy and Climate Change Committee reported that these losses are between 3% and 10%, depending on the region [1]. In 2018, the total electricity losses amounted to 7.6% of electricity demand [2]. While this may appear to be negligible, it amounted to 27 TWh [2] — worth 2% of the entire UK greenhouse gas emissions for the same year [3]. Power lost in transmission not only does not offer anything useful to society like residential and industrial demand does, but it leads to financial losses and waste of resources. A decrease in either transmission or distribution losses could offer more cost-effective solutions, as well as conserve resources, thus decreasing the energy industry’s environmental impact.

Knowing this, part of the power engineering community had been excited to develop superconducting transmission cables with near-zero resistance. A serious research effort was in place during the 1960s and 70s to develop sustainable cables [4]. Despite the apparent technological success of certain projects, they were deemed too complex and expensive to put into practice. Their manufacturing costs and the serious cooling power required to keep the long cables at as low as 4.2 K, which was the highest practical superconductor temperature at the time, were not acceptable.

After the discovery of superconductors able to operate well over 77 K (the boiling temperature of liquid nitrogen), there was a renewed interest in superconducting cables. The increased current capacity means easier meeting of the increasing demand in urban areas, as well as the possibility of bringing the MV distribution voltage down and skipping the installation of otherwise expensive transformers. Furthermore, superconducting cables become highly resistive under large fault currents, which may be used to limit said currents.

Since the year 2000, over 25 projects [4] have sought to develop a superconducting cable primarily at distribution level, and half of those have been installed in a real grid. Only



a few projects, however, have been installed permanently. This is due to the relatively new superconducting technology, which network operators would be reluctant to install without sufficient knowledge of its unconventional operation. In particular, if a through fault is experienced by the cable, the fault current would generate heat that could be enough to push the superconducting material into its normal resistive state, which in turn would generate even more heat. After the fault is cleared, a conventional cable would be immediately ready to conduct electricity again. A superconducting cable, however, needs some time for the coolant to bring the temperature back into working range. How long this time is depends highly on individual cable designs, as well as the magnitude and duration of the fault current. Creating a practical study to experimentally determine the effect of those parameters would require a considerable amount of money in order to manufacture, install and test all possible combinations. The alternatives are two — analytical model or a numerical simulation. While analytical equations are fast and often reliable, they are not capable of describing the multiphysics at every point within the cable. Modern computational power provides a versatile tool, capable of calculating large numerical studies in a relatively short time. However, with the large nonlinearity of the superconducting material and the necessary mesh density, an accurate simulation is not the fastest, not only in 3D but also in 2D.

There is a need for multiphysics models that can simulate both steady-state and transient conditions within a reasonable amount of time [5]. Such efficient models may be useful for the commercial implementation of superconducting cables as they will facilitate the theoretical design and understanding of how a particular design will behave in all possible situations.

The aim of this work is to investigate ways to speed up the finite element modelling of the overcurrent response and recovery of first generation cables, as well as to show that it is possible to accurately simulate the entire range of transport currents (from zero to high transients) in one single model. To achieve that, it is shown how to efficiently simulate the AC power loss in multifilamentary first generation tapes, and then how to simulate them when these tapes are wound and twisted over a former to construct an actual cable. The final model is built as illustrated in Figure 1.1 and verified against literature.

Furthermore, the techniques used could serve as a stepping stone for future design studies of cables for installation in a particular grid section.

Thesis structure:

- Chapter 2 is a brief summary of the background theory of the superconducting phenomenon, important materials and loss mechanisms.
- Chapter 3 provides a literature review of the existing recent and relevant experimental and numerical works on superconducting cable fault response, quench and

thermal recovery, and identifies the research questions.

- Chapter 4 introduces the physics that are needed for FEM simulation within COMSOL, then proceeds to verify the models with existing peer-reviewed measurements and simulations.
- Chapter 5 proposes and verifies a homogenization technique for improving the computational time when simulating the AC loss in multifilamentary tapes.
- Chapter 6 discusses a technique for the 2D AC power loss estimation of tapes twisted around a former. The Chapter also discusses how to model the power loss in cables which are made of more than one layer and solves the problem of what length along the cable should a cross-section be taken. The proposed techniques are verified against 3D models and results from literature.
- Chapter 7 focuses on the overcurrent response and recovery of a power cable described in literature. Additional physics are discussed and implemented together in a complex multiphysics model in COMSOL and are accompanied by supplementary variables and equations.

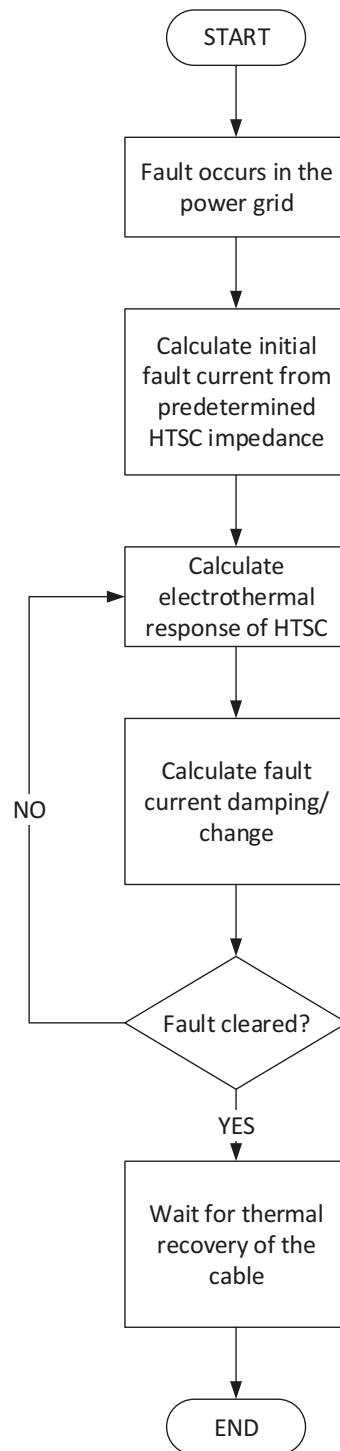


Figure 1.1: A flowchart with an overview of the final multiphysics model.

## Chapter 2

# Theory of high temperature superconductors

### 2.1 Brief theory of superconductivity

Superconductivity was first discovered in 1911 by Kamerlingh Onnes [6], who observed that a number of metals exhibit a significant drop of resistivity under a material-specific critical temperature  $T_c$ . That behaviour is called *superconducting state* in comparison to the otherwise common *normal state* [7]. Currents have been observed to travel unobstructed and unaided for years, which implies a *near-perfect conductivity* [8]. However, they are not perfect conductors and do not possess infinite conductivity — merely a very large one.

There is a large volume of physics trying to explain the microscopic behaviour of superconductivity. This work, however, is focused on macroscopic behaviour and as such, the following very brief background theory is provided primarily for understanding the underlying concepts that dictate how superconducting materials behave.

#### Summary of the Critical Variables

Superconductors have three important parameters, above which superconductivity is destroyed and the material enters a "normal" state — critical current  $J_c$ , dependent on temperature and magnetic field, critical magnetic field  $B_c$  (or upper critical field, which will be discussed later), also dependent on temperature, and critical temperature  $T_c$ . The critical current and the critical magnetic field are to an extent interchangeable variables due to the Maxwell Equations.

#### Meissner Effect

Perfect conductivity means that an already fully penetrating magnetic flux would be trapped inside while a newly applied one would be repelled by introducing screening

currents [7, 8]. In 1933, Meissner and Ochensfeld [4, 9] suggested experimentally that superconductors (type I, more on that further on) possess *perfect diamagnetism* (e.g.  $B = 0$  inside the superconductor). Perfect conductivity and perfect diamagnetism are different.

To establish the perfect diamagnetism property, Meissner and Ochensfeld performed the following two experiments. If a superconducting material in normal state is subjected to a constant magnetic field  $H$  and then cooled down below  $T_c$  (field-cooled experiment), the magnetic flux will be expelled entirely from the body of the superconductor once  $T = T_c$ . Furthermore, if a superconducting material is first cooled down to below  $T_c$  and then subjected to a constant magnetic field  $H$  (zero-field-cooled experiment), the magnetic flux will be expelled in the same manner.

In the zero-field-cooled experiment, a material in possession of (near-)perfect conductivity would repel the magnetic flux. Since a magnetic field is introduced to an already superconducting material, a field gradient  $dH/dt$  will be introduced [4]. This was verified to behave as predicted.

On the other hand, in the field-cooled experiment, the material is not in superconducting state once the field is applied. Thus the fully penetrating magnetic flux would be trapped inside if the material possessed only near-perfect conductivity. However, in practice a complete expulsion of the magnetic flux is observed.

The perfect diamagnetism of superconductors is called the Meissner Effect.

### **Bardeen-Cooper-Schrieffer Theory**

No proposed microscopic theory that explains the features of superconductivity has been universally accepted [4]. The first quantum mechanical theory was proposed by Bardeen, Cooper and Schrieffer (BCS) in 1957 [10], for which they received a Nobel prize in physics in 1972.

The BCS theory states that the mechanism of superconductivity is governed by an electron-lattice-electron interaction, activated by phonons in the material. If an electron deforms the lattice by interacting with it, another electron can detect the change of energy redistribution and readjust. Electrons experiencing this interact with each other in pairs, through the phonons, and these pairs are called Cooper pairs. It is believed any pairing mechanism is capable of inducing the attraction, and that it is likely something else in addition to phonons is behind it.

### **The Mixed State and Type II Superconductors**

Coherence length has been described as the distance that electrons can "see" each other to form a Cooper pair [11], the distance over which a Cooper pair can exist [4] and the distance over which the density of superelectrons varies from its maximum value (superconductivity) to zero (normal state) [7]. A considerable change in the density of

”superelectrons”  $n_s$  is only possible within the coherence length  $\xi$  [4].

Initially, superconductors had been observed to possess perfect diamagnetism up until their superconductivity is lost above a critical magnetic field  $H_c$ . New materials, called Type II superconductors, were discovered, which experienced a gradual increase in magnetic flux penetration above a lower critical magnetic field  $H_{c1}$  without losing superconductivity. This gradual increase of flux penetration lasts until an upper critical field  $H_{c2}$ , above which the material enters a normal state, losing all superconductivity. Thus, a magnetic field  $H$  such that  $H_{c1} < H < H_{c2}$  gives rise to a combination between the superconducting and normal states, called *mixed state* [12].  $H_{c1}$  and  $H_{c2}$  are also dependent on temperature [11]. Mathematically, the mixed state was first described by the Ginzburg-Landau theory. Superconductors can be classified, depending on the value of the Ginzburg-Landau parameter, which was introduced by Abrikosov in 1957 [13]:

$$\kappa = \frac{\lambda_L(T)}{\xi(T)} \quad (2.1)$$

where  $\lambda_L$  is the London penetration depth [11] – the distance from the surface of the superconductor at which the magnitude of the penetrating magnetic field has decreased to  $1/e$  from the value at the surface. For  $\kappa < 1/\sqrt{2}$ , the material is a Type I superconductor. For  $\kappa > 1/\sqrt{2}$ , the material is a Type II superconductor [4]. It should be noted that both the coherence length and the penetration depth are dependent on temperature [14] but that dependence is nearly identical [7].

Type I superconductors are only metallic elements, while type II can include metal alloys, pure metals and oxide compounds. Those with  $T_c < 30$  K are metals and metallic alloys, labelled low-temperature superconductors (LTS). Those with  $T_c \geq 30$  K are usually oxide compounds and are called high-temperature superconductors (HTS) [12]. High temperature superconductors are all Type II.

### Characteristics of Type II Superconductors

In the mixed state of type II superconductors, the magnetic flux penetrates the material in the form of what is described as flux tubes [7], or ”super-current vortices” [15], that carry an equal amount of magnetic flux, similarly to energy quanta. The magnetic field experiences what is called flux pinning — the flux vortices are not allowed to move under the Lorentz force. This allows large DC currents to flow without any resistance for a very long time; for an AC current and its corresponding magnetic field to exist, the vortices cannot remain stationary. In that case the pinning force must be overcome, which introduces some power loss which is called hysteresis loss [15] (a discussion about all loss mechanisms can be found in Section 2.3).

Flux pinning exists due to microscopic barriers that are usually structural imperfections, chemical impurities, or grain boundaries [11]. Somewhat counter-intuitively, the more impurities a superconductor has, the higher currents it would be able to sustain [12].

The flux vortices can also escape pinning centres under thermal activation [11]. Let the energy required for a flux vortex to jump from the energy potential well of a pinning centre to the closest position of energy equilibrium be  $\Delta W$ . Then, if  $\Delta W \gg kT$ , the mechanism of flux depinning is called *thermally activated flux creep*, which occurs at low temperatures; the simplest explanation of flux creep is in the work of Anderson and Kim [16], and a more complex vortex glass theory has been developed in [17]. If  $\Delta W \ll kT$ , the mechanism is called *flux flow*, which occurs at high temperatures and exhibits lower pinning energy, usually due to the Lorentz force overcoming the pinning strength [12]; the first theory of flux flow has been presented in [18].

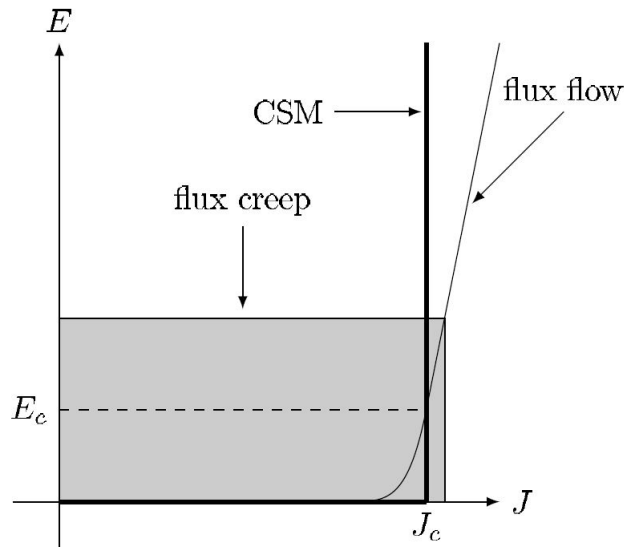


Figure 2.1: E-J characteristic of HTS [15] © 2014 IEEE.

### Critical State Model

The next step in the description of the electromagnetic behaviour of superconductors was the Bean Critical State Model (CSM) from 1962 [19]. It assumes that the current density within a superconductor can only be equal to  $\pm J_c$  in regions where  $B \neq 0$  T and 0 when  $B = 0$  T. This has been found useful for low-temperature superconductors with large power index  $n$ , but is not acceptable enough for HTS materials, which often have a smoother transition between superconducting and resistive state. Moreover, the CSM cannot model overcurrent [15] which is a chief reason the nonlinear E-J method is preferred in the present work. The CSM allows for analytical solutions using approximations and simple geometries [11] and is valid on a macroscopic scale that does not take into account individual flux pinning vortices [15].

## 2.2 Overview of superconducting materials for power applications

In 1987 the first HTS material with  $T_c$  above the boiling point of liquid nitrogen (77 K, LN<sub>2</sub>) was discovered. This is the material YBa<sub>2</sub>Cu<sub>3</sub>O<sub>7</sub> (“YBCO-123”) and it has



Figure 2.2: First generation multifilamentary conductor, produced from Bi-2223 superconducting material (dark filaments) and filled with Ag or similar [23] © 2004 IEEE.

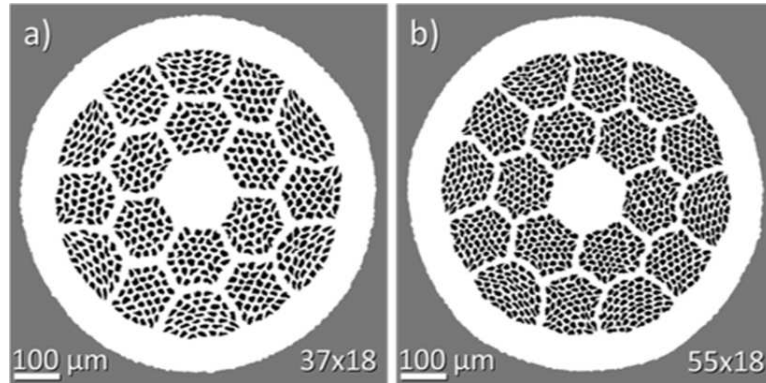


Figure 2.3: First generation multifilamentary conductor, produced from Bi-2212 superconducting material (dark filaments) and filled with Ag or similar [24] © 2019 IEEE. a) 18 groups with 37 filaments each; b) 18 groups with 55 filaments each.

a critical temperature of 93 K [20]. It has further been identified that the yttrium component in the above compound could be replaced successfully with any other rare earth material while the properties would not vary significantly [4]. Many other materials have been discovered to exhibit HTS properties [4]. The most notable ones are within the Bi-Sr-Ca-Cu-O system [21, 22]:  $\text{Bi}_2\text{Sr}_2\text{Ca}_2\text{Cu}_3\text{O}_{10+x}$  (Bi-2223) and  $\text{Bi}_2\text{Sr}_2\text{CaCu}_2\text{O}_{10+x}$  (Bi-2212).

### 2.2.1 1st Generation HTS – Bi-2223 and Bi-2212

Superconducting wires, produced from a composite between silver and Bi-2223 or Bi-2212 are referred to as First Generation. Typically, the structure of a Bi-2223 wire is in the area of 0.2 mm by 4 mm, constructed of between 30 and 61 tape-shaped Bi-2223 filaments, 10  $\mu\text{m}$  thick and up to 200  $\mu\text{m}$  wide each, embedded in a silver alloy matrix (Figure 2.2). Silver, or an alloy that includes silver, fills the gaps between the filaments and provides electrical and mechanical stabilization as well as facilitating the production process [23].

Meanwhile, the typical structure of a Bi-2212 conductor (Figure 2.3) is an isotropic round wire, consisting of a large number of superconducting filaments, arranged symmetrically in arrays and embedded in a matrix material. A typical diameter is around 1-1.5 mm [4].

Due to their microstructure, the Bi-2223 and Bi-2212 materials are spatially anisotropic, thus grains are required to be aligned in the direction of expected current flow. In



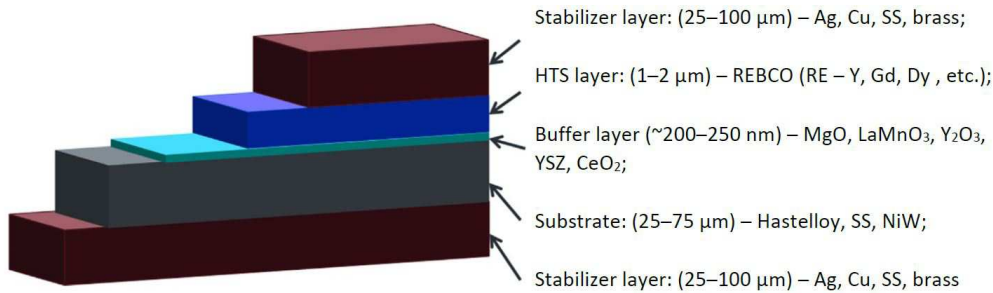


Figure 2.4: Second generation composite conductor, produced from REBCO superconducting material. Not to scale [4] © 2015 Elsevier.

industry, until 2004 the most widely accepted method for manufacturing Bi-2223 tapes was the ‘powder in tube’ technique [25], and after 2004, a technique called ‘controlled overpressure sintering’ gained substantial popularity [26, 27]. The notable similarity between the two is that the result of both is flat tapes. This is a direct link to the fact that grain alignment of Bi-2223 is easiest during the rolling process [4], which is the last stage of the aforementioned methods.

Despite this, research has shown that producing round Bi-2223 in laboratory conditions is possible [28]. Bi-2223 has intrinsic anisotropy of all of its electromagnetic properties [12].

The  $J_c$  of each wire is largely dependent on its size, manufacturer and manufacturing process. Typical engineering  $J_c$  of first generation wire are 130-180 A/mm<sup>2</sup> [23, 29] and 350-400 A/mm<sup>2</sup> for Bi-2212 [29, 30], however these numbers are likely to increase with the advancement of technology.

### 2.2.2 2nd Generation HTS – YBCO

Second generation superconducting wires are based on REBa<sub>2</sub>Cu<sub>3</sub>O<sub>7-x</sub> (REBCO) family where RE is any Rare Earth material, commonly yttrium. 2G is reported to have a higher current density and better price forecast than first generation [4]. YBCO is less anisotropic than Bi-2223 [12]. All coated conductors include a flexible substrate, preferably of strong and nonmagnetic or weakly magnetic metal, on top of which is a multifunctional oxide barrier or buffer layer, on top of which is the superconducting YBCO layer. A thin protective Ag layer and a thicker Cu protection and stabilization layer must also appear [23].

Stabilization layers are used to carry the burden of overcurrent and thus protect the superconducting layer from damage once it has “quenched” – i.e. become highly resistive due to the overcurrent. Despite that superconductivity in REBCO was discovered before superconductivity in Bi-2223, manufacturing of sufficiently long wires had been a difficult challenge for decades. In 2003, it was proven via different methods that wires of length can be produced of lengths up to 50 metres, in a configuration, based on the one displayed in Figure 2.4; this length has increased in the subsequent years. An observed tape

engineering  $J_c$  is 205 A/mm<sup>2</sup> for YBCO 2G [4, 26].

Counter-intuitively, the "generation" does not refer to better quality or bigger potential for the material. It simply refers to the fact that the first time YBCO has been put in tapes was after Bi-2223.

### 2.2.3 MgB<sub>2</sub>

The Magnesium diboride superconductor possesses a critical temperature of 39 K, which puts it in the unique position of sitting between HTS and LTS, but it is still classified as low temperature. Its superconductivity was discovered in 2001. Similarly to Bi-2212, for applications the typical shape of a MgB<sub>2</sub> wire is usually round (but may take the shape of a tape, Figure 2.5), containing superconducting filaments, embedded in a conducting matrix made of metallic material or alloy. For cable applications, round wires can be prepared by the power-in-tube technique, mentioned above [4, 26].

### 2.2.4 Low temperature superconductors

Some of the most common LTS materials still in use are Niobium-Titanium (NbTi) and Niobium-tin (Nb<sub>3</sub>Sn), each with a critical temperature of 10.2 K and 18.3 K, respectively. LTS have been used for decades and are still widely adopted due to being relatively cheap and easy to manufacture [4]. Cross-sections of the two most common materials can be seen in Figure 2.6.

### 2.2.5 Why use HTS and not LTS?

A large barrier to the integration of LTS materials, including MgB<sub>2</sub>, into power grid applications is the low critical temperature (20-30 K) far under the operational temperature of liquid nitrogen (65-78 K). This prevents the deployment of cryogenic systems with liquid nitrogen and instead forces the use of supercooled or liquid helium, which

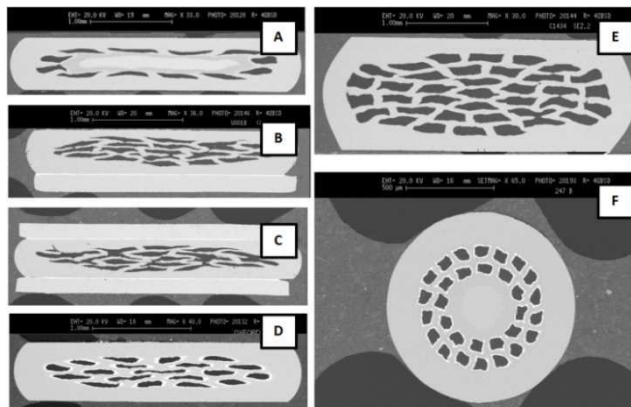


Figure 2.5: A selection of MgB<sub>2</sub> cross-sections. A) Flat tape conductor; B) and C) Sandwich type conductor; D) low-AC loss multifilamentary tape; E) high current tape conductor; and F) Round wire for cable application [26].

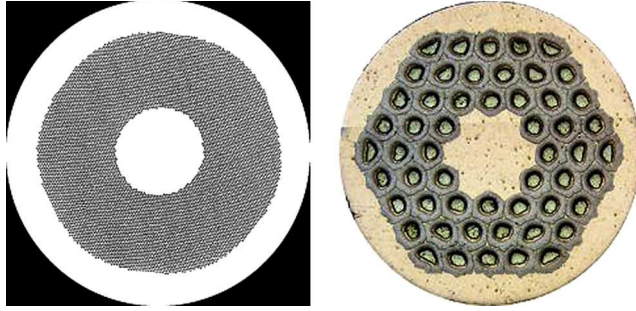


Figure 2.6: The cross-section of a NbTi wire (left) and a Nb<sub>3</sub>Sn wire (right). Diameter roughly 0.8 mm, wires are multifilamentary. [4]

introduces a large cost of refrigeration and handling of ambient heat as well as heat from AC losses [4]. The vast majority of power grid superconducting cable projects and research are now done with HTS materials.

### 2.3 AC power loss mechanisms and their calculation

Four primary AC loss mechanisms have been identified in high temperature superconducting tapes [15]. Analytical calculations of hysteresis losses in particular are extensively described in [14] and [15].

**Magnetization (*hysteresis*) loss.** As discussed in Section 2.1, hysteresis losses arise from the phenomenon where the oscillation of the applied magnetic field (through the applied current) must overcome the pinning of the flux vortices.

Instantaneous power dissipation at a point in a Type II superconductor can be calculated numerically by  $Q_h = J \cdot E$  [15];

**Eddy current loss.** Eddy currents are induced in the conducting materials within superconducting tapes (copper, silver, etc.) by an applied AC magnetic field or the self-field of an applied AC transport current. Thus, Ohmic (resistive) losses are accumulated [12] and  $Q_e = J \cdot E$  is used to numerically calculate the instantaneous losses at a point;

**Coupling loss.** This occurs when under the effect of a sufficiently high time varying magnetic field, a current loop jumps through the metal matrix between individual filaments, thus generating Ohmic (resistive) losses. Simulations in this work deal with transport currents and as such the resulting magnetic field is not significant enough and the coupling losses may be considered negligible [15];

**Ferromagnetic loss.** Arises from the presence of ferromagnetic materials within the tape structure.  $\mu_r$  [15]. Simulations in this work do not include ferromagnetic materials, thus this loss mechanism has not been investigated.

## Chapter 3

# Literature review

### 3.1 Chronological review of previous research into the simulation of overcurrent and fault response of HTS cables

The study performed by a research group in Tohoku University, Japan (Hu *et al* [33]), adopts a temperature-dependent analytical AC loss generation equation. The heat transfer equations are standard. The paper investigates a 66 kV Triax cable. Important conclusion is that the thickness of insulation (PPLP) is approximately linearly proportional to the recovery time of the cable. In Triax, this poses a potential problem at higher voltages due to the sandwiched phase in the middle that is without direct access to coolant flow. Furthermore, the study confirms that the middle phase inevitably does reach higher temperatures and achieves longer recovery time.

This study is preceded by an earlier work by Hu *et al* [34], which investigates the effect of the thickness of the stabilizer that exists next to each superconducting phase layer. Intuitively, their discovery is that thicker stabilizers provide the conditions for lesser temperature increase. In addition, a later study from the same authors [31] builds on the previous studies to include a model of flowing coolant liquid and combine heat transfer in both radial and longitudinal directions; see Figure 3.1. The model is built via finite differences. In this paper, the magnitude and duration of the applied fault current is based on recommendations from a Japanese electric power company, in contrast to the vast majority of other studies that do not specify how their fault current was derived. Highly descriptive temperature profiles within the cable are presented, with liquid nitrogen outlet temperatures being compared based on length of the cable and velocity of coolant flow. A counter-intuitive discovery is that higher velocity of coolant flow can produce higher maximum temperature. However, the paper has not investigated how the velocity affects the recovery time, since maximum temperature and recovery time may not necessarily be proportional. Despite the lack of results of such investigation, the authors conclude, intuitively, that faster coolant flow would indeed result in faster recovery time.

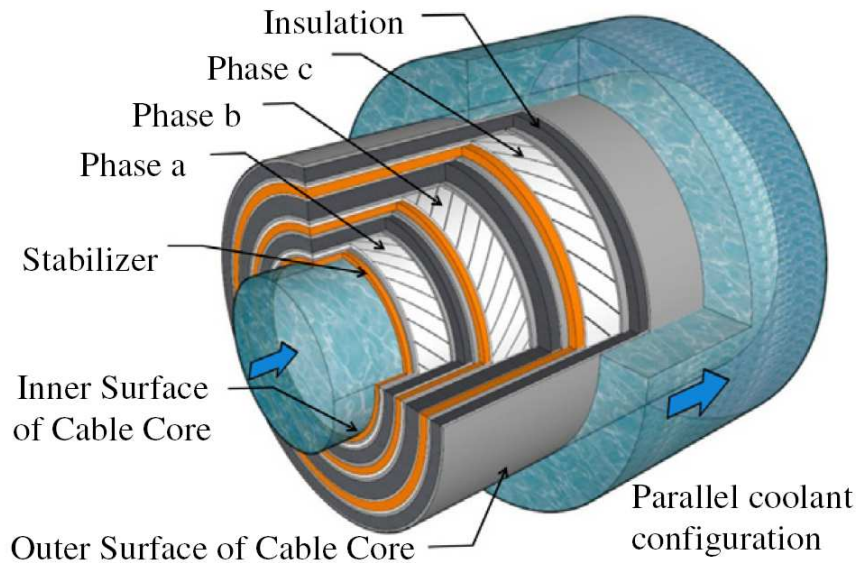


Figure 3.1: The general structure of an HTS cable in the Triax configuration, as seen in Hu *et al* [31] © 2013 Elsevier. This Triax cable operates a parallel coolant configuration where the inner and outer coolants are flowing in the same direction, with an external return flow.

Shu *et al* [36] implement an equivalent circuit model to simulate overcurrent and overvoltage in all three phases of a 1-kilometre-long 110 kV cable. As an extension of this study, equivalent  $\pi$  circuit model of a 110 kV, 3-phase cable has been developed by Li *et al* [37]. Presented are results for both a short circuit fault and electrical breakdown fault; it does not become clear how the fault current is determined.

Another full model of a 3-phase, 22.9 kV Triax cable under a three phase fault has been developed in Sun-Kyoung *et al* [32] (see Figure 3.2). The methods utilized include an electrical model in PSCAD/EMTDC, coupled with heat transfer equations. However, there is lack of information about how exactly the temperature increase affects the overcurrent development in the model, but the publication considers in detail the design of superconducting cables. It draws attention to the design challenge of ensuring the current flow in each layer of a phase is balanced. A particular conclusion is that the middle phase in a Triax design would experience the highest temperature increase due to the decreased access to cooling, which makes it a particular point of interest in that design type.

A unique model to consider the gaps that are between the individual layers of tapes within a phase has been built in Fang *et al* [38]. The model used is once again equivalent circuit equation, combined with heat balance and transfer. Presented is a dependency of the maximum temperature in the cable on the heat transfer coefficient.

A series of papers have been published by researchers from the China Electric Power Research Institute (CEPRI) and associated institutions, which investigate the coupling

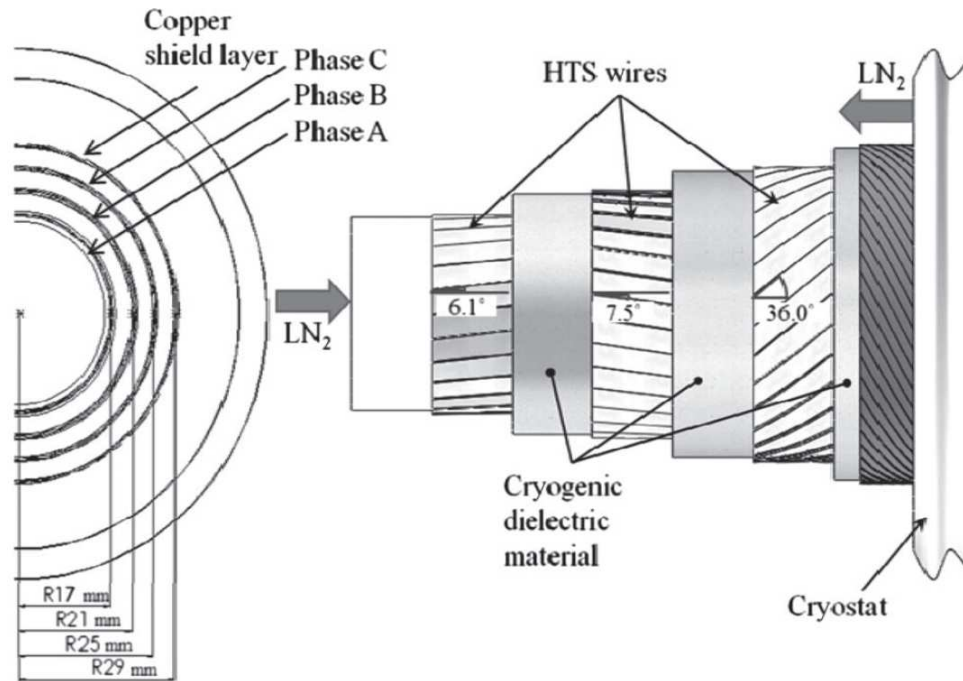


Figure 3.2: The design of an HTS cable in the Triax configuration, as seen in Sun-Kyoung *et al* [32] © 2013 IEEE. This Triax cable operates a counter-flow coolant configuration where the inner and outer coolants are flowing in the opposite direction, thus the return of mass happens within the cable structure.

of the thermal and electromagnetic studies on a 110 kV, 3 kA rated superconducting cable under a fault current. In essence, the complete model is a mathematical equivalent circuit together with heat transfer equations.

The most recent paper that provides results on both temperature and current distribution is the work of Li *et al* [39]. They simulate a 10 metre, 110 kV cable in MATLAB and ANSYS and apply a through fault current. Provided are cable dimensions, but there is no discussion of any methodology. This seems to be based on earlier work done in CEPRI [40]. Here, a complete mathematical breakdown of the equivalent circuit method, as well as the thermal model, is provided. Key findings includes that the fault current distribution between all layers, this including the stabilizer and former, and the time needed for this distribution to be reached, depends greatly on the resistances that the materials possess when subjected to said fault current. It also demonstrates the reason why the part of HTS cables, called former, is required — 96% of the fault current in the study is reported to have been eventually redirected to the former.

A similar study by the same research group [35] describes a 2D finite element model of the same problem and cable, implemented in ANSYS together with an equivalent circuit model. The model presents a table with the thermal properties on a number of materials at cryogenic temperatures, which are otherwise difficult to obtain.

Figure 3.3 presents a flow chart of the program used in [35]. This serves as a confirmation of the proposed final product flow chart as seen in Figure 1.1.

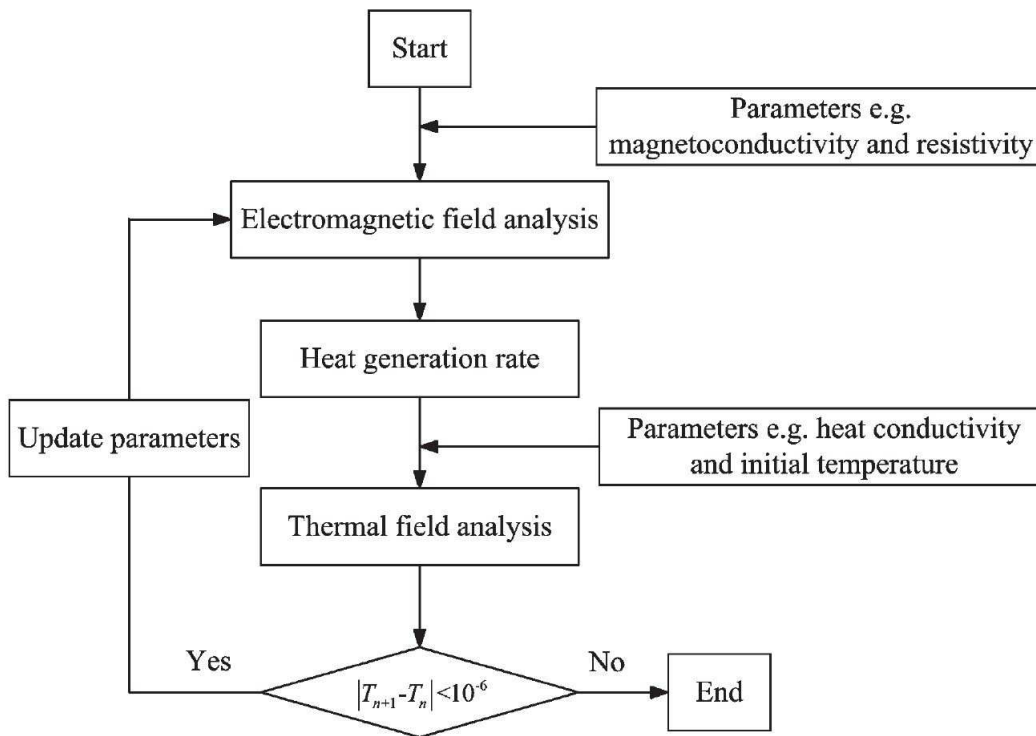


Figure 3.3: An electro-thermal coupled simulation program flowchart [35] © 2013 IEEE.

Yin *et al* [42] look at the overcurrent distribution in a single core HTS cable. The investigation is purely electromagnetic, and uses an equivalent circuit model. While there are mentions of magneto-thermal coupling, no methods or results regarding temperature are presented. For the simulations, two currents — one value below the critical current, and one value above — have been used. It demonstrates a successful implementation of the equivalent circuit model for an HTS cable, and points out that the design of the cable’s copper stabilizer (former) plays an important part in the current distribution in case of a fault.

A research group from Waseda University, Japan, together with other institutions, have published a recent series on the temperature and pressure changes in cables, cooled by liquid nitrogen. Their research follows a structure of developing a finite differences computer model for heat transfer and fluid flow [43], and its subsequent improvements and verifications with real or analytical 1.5-metre [44], 20-metre 275 kV [45, 46], 40-metre 66 kV [47] and 3-kilometre 66 kV [48] cables. Their research does not incorporate any electromagnetic phenomena calculations and relies on 1D discretization. Moreover, the transient fault current — whenever a part of a study — is not calculated within the simulation but usually a value of the heat generated in the conductor is provided.

The 20-metre long 275 kV cable [45] is with central coolant flow, single phase and of concentric design. Besides an insight into possible solutions of the problem that is the heat transfer between solids and the coolant, the results display how an overcurrent can increase the temperature of the conducting material noticeably. The research on that

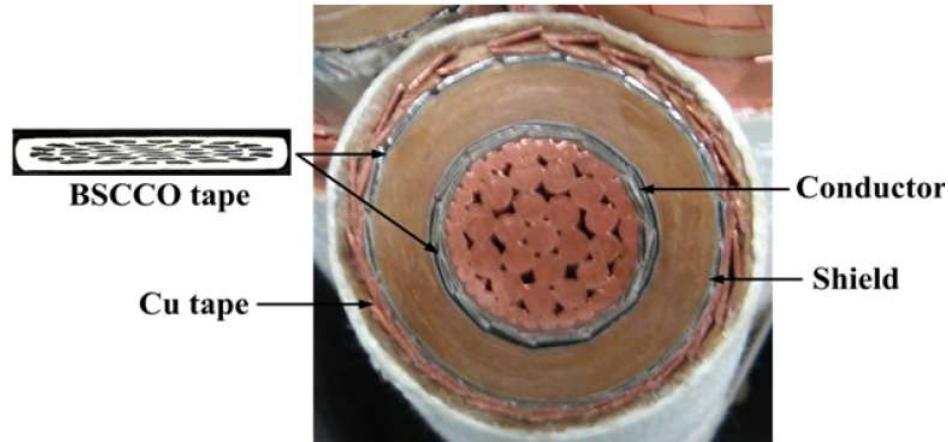


Figure 3.4: This photograph from [41] © 2015 IEEE shows a single phase of a 50 MVA HTS cable. First generation tapes can be seen (23 in the conductor, 19 in the shield, silver-coloured, 4.3 mm by 0.22 mm) for both the conductor and the shield, and an electrical insulation in between. Copper stabilizers are also present in the form of tapes (for the shield) and wound wire (for the conductor). This particular design does not have an internal channel, so the coolant flows outside of the shield. The inner diameter of the conductor is 16 mm and the inner diameter of the shield is 25.88 mm [41].

cable is continued with [46], where a fault's effect on the temperature of the conducting layers and coolant is analysed. The conclusions drawn are from the perspective of post-fault recovery.

The 40-metre long 66 kV cable [47] is again single phase, but without a central coolant flow. It is noted that the temperature of the inlet of coolant flow (before any contact with the superconducting cable) may rise due to joule heating of the normally conducting parts in the joint, and that it is possible in long cables that the coolant would evaporate when approaching the outlet.

The 3-km long 66 kV cable [48] is a three-core cable. The finite difference method has solved for the properties of the  $LN_2$  before, during and after a short-circuit fault. It is concluded that for long cables, all AC, dielectric and joint losses have to be taken into account.

The research team from Waseda University has examined HTS cables previously. Wang *et al* [49] measure a 2-metre-long 66 kV second generation HTS cable under fault conditions, then proceed to numerically estimate the losses via 3D finite element analysis. An equivalent circuit is introduced to consider the magnetic coupling between the shield and conducting layers. The power law used appears to be simplified and does not take into account temperature, which does not seem to introduce a significant error. Despite the authors' conclusion that the models match well, some variables see a considerable unexplained difference between simulation and experiment.

This study is preceded by [50], where the same problem is tackled for a 20-metre cable with similar specifications. This paper is valuable as it presented detailed dimensions



for the model cable, as well as thermal properties of liquid nitrogen around boiling temperature. However, the numerical model presented is not verified with experiment, as far as the publication is concerned.

Within the same research group [51], a 275 kV cable, also of 2-metre length, has been investigated both experimentally and numerically. The methods are the same as the studies above, and particular attention is paid to the thickness of the copper stabilizers.

A more detailed temperature and pressure model has been published by Shabagin *et al* [52], such that a cross-sectional temperature profile is coupled with the longitudinal coolant temperature profile, producing a 3D distribution. They consider the AmpaCity [53] project cable for their calculations, which is of a Triax design, and suggest that boiling of the liquid nitrogen can be prevented (to an extent) by controlling the pressure of coolant at the inlet. The authors present their temperature and pressure calculation methods with excellent detail, but the current (steady-state) is once again calculated by an analytical method.

Miyagi *et al* [54] have recently shown a Triax cable can achieve a longer length per cooling station than its corresponding three-core counterpart, within a set diameter limit. The necessary calculations have been achieved via analytical formulas while a number of useful parameters and material properties are provided.

A 22 kV, 3 kA, 2G Triax HTS cable intended to be used as a busbar, has been developed in [55]. Then, it has been subjected to a short circuit fault both experimentally and numerically, while a bypass copper cable exists in parallel. For the numerical model, an equivalent circuit has been used, while the common heat equation is used for thermal modelling. The conclusions of this study are that by having a bypass cable, the post-fault recovery time can be decreased significantly.

In [56] by de Sousa *et al*, a cooling method with an external return flow tube is proposed and the results indicate it is feasible. Analysis of the thermal response under both normal and fault conditions is performed via a finite differences method. This is based on a heat source being the transport current, but no details about the electromagnetic modelling are presented.

Again by de Sousa *et al* [57], a finite difference model is introduced for the simulation of the transient fault response and recovery of the first generation AmpaCity cable. The paper offers an excellent opportunity for verification of any FEM models built within this study due to its detailed description of parameters and results.

## 3.2 Overview and research questions

As discussed in the previous section, the state of the recent literature (2009 onwards) shows there are few studies that explicitly examine the recovery time of cables. The links to realistic power grids are limited. The most commonly utilized electromagnetic model is an equivalent circuit model. Meanwhile, there is solid research into the temperature

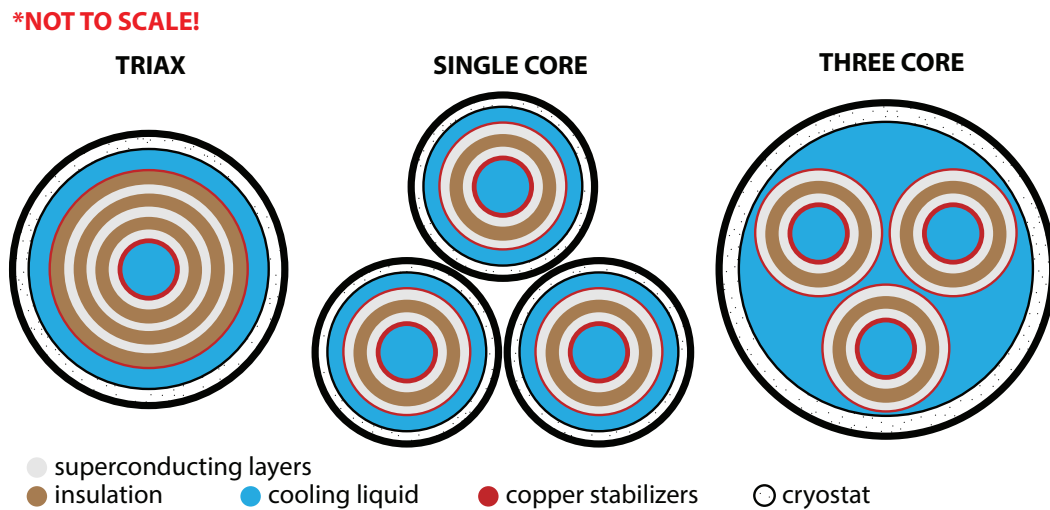


Figure 3.5: The three options for spatial design of 3-phase HTS cables. Not to scale; for illustrative purposes only.

distribution and coolant flow, all of which favours classical heat transfer and fluid flow equations. It is easily seen there is very little work done in the past 10 years regarding the multiphysics FEM modelling of superconducting cables both at the steady-state level (normal operation at currents below critical) as well as at the transient level. The term "multiphysics model" in the scope of this study is defined as a model built by two or more different physics (i.e. heat transfer, electromagnetics and fluid dynamics) coupled together such that simulating the model provides a better and more accurate understanding of the system behaviour than if only one of the physics was used.

There exist three possible spatial designs for 3-phase superconducting cables. For illustrative purposes, those are presented in Figure 3.5. From the review of the literature, it becomes clear there is no model that uses a finite element method or equivalent to introduce a multiphysics model of any of the three possible designs, particularly for first generation tapes.

Work on the finite element models is focused on cables made up from the second generation tapes [58–61]. While it may be argued that the second generation has gained significant popularity in the past decade and displays excellent potential, first generation technology is still widely adopted and continuously improved [62] and the HTS cable projects with longest cable lengths deployed have been made with Bi-2223 tapes (AmpaCity [63] and LIPA [64]). Hence it would not be unreasonable to focus on the tape which is less researched.

If the time needed for a superconducting cable to be ready for operation after a significant through fault is to be examined, there is one primary question that has to be answered — "How fast can the materials that an HTSC is built of be cooled down to operational temperature?". While the answer would depend greatly on design specifications and

the power grid, this can be further dismantled into further questions, such as — ”What electromagnetic response does a cable exhibit when subjected to a current, substantially larger than its rated current?”, ”How does the temperature affect the electromagnetic response and vice versa?” and ”How fast could a multiphysics model of the transient response and recovery of a 1G HTS cable be simulated?”.

The unique question this thesis will probe is ”Can a single model be made which can accurately simulate the whole operational range of a 1G HTS power cable in a reasonable amount of time?”. A single model that may simulate the AC losses during both steady-state and transient operation is not demonstrated in literature; a combined model would ease the effort required to theorize a new power cable for installation in a real grid.

To be able to answer the set questions, consideration must be made of the steps that might be necessary to construct the model. Section 3.3 describes the previous research in homogenizing the large amount of filaments in a 1G tape, and Section 3.4. describes the previous research in attempting to model in 2D the losses incurred in an inherently 3D twisted tape. Both steps are taken in order to simplify the geometry and speed up the simulation.

### 3.3 Existing techniques for homogenization of multifilamentary tapes

A number of papers note the similarities between the measured losses in some multifilamentary tapes and tapes with an elliptical monofilament [65], as well as Norris’s elliptical model [66,67]. This arises from the fact that in densely packed multifilamentary tapes, a strong magnetic coupling exists between the filaments such that the filaments experience the magnetic field as one entity. Therefore, it may be reasonable to assume the superconducting domain can be modelled as a single uniform domain, instead of its actual multifilamentary geometry.

Researchers in [68], [69] and [70] use a homogeneous model to represent the superconductor in their numerical models. However, a description of their homogenization methodology is not provided. Hence, replication of these numerical models is not possible. [71] uses a technique where the filamentary region is assumed to be a uniform superconductor. The matrix material is ignored in the AC loss modelling and, naturally, there is no investigation of overcurrent with that model. Furthermore, the description of the technique is minimal. The same technique is briefly explained in [72], but not in the context of AC loss modelling.

The only full AC power loss homogenization technique that has been identified is described in [73]. In it, the material within the multifilamentary region is represented as a mixture between the matrix (silver) and the superconductor (Figure 5.1). Its conductivity is then defined as:

$$\sigma = \lambda_{fr}\sigma_{sc} + (1 - \lambda_{fr})\sigma_{Ag} \quad (3.1)$$

where  $\lambda_{fr}$  is the fraction of superconductor in the filamentary region (e.g. the ratio of the total area of the superconducting filaments and the area of the multifilamentary region),  $\sigma_{Ag}$  and  $\sigma_{sc}$  are the conductivities of the silver (or any other material) matrix and superconducting material, respectively.

The drawback of this model is that it requires drawing a shape that may be a mix between an ellipse and a rectangle. This is not straightforward, because  $\lambda_{fr}$  is directly linked to the area of that shape and any errors may noticeably change the model output. The verification of the prediction of AC losses using that homogenization technique is not directly presented — however, another paper by the same authors references the same tape. The results from the simulation are presented and compared with this work's homogenization technique in Figure 5.5. Lastly, the technique does not seem to be implemented in modelling systems of tapes.

### 3.4 Existing techniques for estimating the losses in twisted tapes and cables

There is limited literature available regarding the finite element modelling of twisted cables and twisted tapes. The majority of developed techniques concern themselves with the modelling of twisted-filament tapes and wires, which are widely used to decouple the filaments but are not the focus in this work.

A reduced 3D model proposed in [74] utilizes a conductivity matrix with anisotropy to model a multi-layer first generation HTS power cable. The conductivity matrix uses trigonometry to influence the direction of current flow based on the twist angle of each layer. However, the underlying construction of the model appears to rely on a monoblock, which may be insufficient to model overcurrent situations.

A similar model is utilized in [75]. Amemiya *et al* [73,76] have developed a technique for the 2D finite element modelling of twisted tapes under an applied magnetic field, which entails representing Ohm's law in 3D via a tensor equivalent conductivity.

Helicoidal symmetry is explored in [77] where a methodology is introduced for simulating the twisted filaments of a superconductor in 2D. This appears to be directed at investigating the properties of the filaments within twisted superconductors rather than the modelling of systems of tapes. Another helicoidal technique for twisted filaments is shown in [78], however in this case the model remains in the 3D domain.

The methods described above chiefly explore multifilamentary conductors in external field or conductors for magnetic applications. Furthermore, they are not straightforward to apply and may not be possible to be adapted for the simulation of power cables.

3D modelling of multi-layer cables results in high computation power requirements even with a relatively coarse mesh [15] which can be thought to render 3D models impractical. A full 3D model of the shielding layer in a real 1G power cable was made in [79],

including the multifilamentary structure of each tape. The purpose of the model was to estimate the magnetic shielding capability of the shielding layers. No comment is made whether a 2D model exists that would be able to accomplish the same task for Bi-2223 superconductors. However, mathematically-derived 1D and 2D approximations for coated conductors (second generation) do exist [15].

In [15] it is simply stated that simulation of the AC loss in Bi-2223 cables requires a 3D model. Using a cross-section is argued can only be used for conductors of infinite length and geometries with cylindrical symmetry. It can be speculated this is true in the general case where no supplementary mathematical or analytical calculations and simplifications are made to introduce this infinitely-long cylindrical symmetry.

However, in [80] it is stated HTS power cables can be modelled in 2D with an acceptable error when the twist angle is "relatively small" due to the negligible axial (longitudinal) magnetic field. It is not clarified how small the angle must be. This is supported by [81], where several second generation cables are modelled in the 2D domain, as a reference point for further 3D studies. A simple cross-section is taken without further considerations. The results show that the shorter the twist pitch is (thus the larger the twist angle), the less accurate the 2D model is in simulating AC loss. This work capitalizes on the principal findings of these studies.

## Chapter 4

# Numerical modelling of superconducting tapes using the finite element method

### 4.1 Physics

#### 4.1.1 The Power Law

From a macroscopic electrical engineering perspective, superconducting materials are special primarily based on their E-J characteristic, the slope of which is known as resistivity. For 'normal' materials the resistivity usually obeys the linear Ohm's Law, but for superconductors it is highly non-linear.

As discussed in the previous chapter, the CSM is not accurate enough for HTS. It has been shown by Rhyner [82] that the superconductor's resistivity conforms to the so-called E-J Power Law, in vector notation:

$$\vec{E} = E_c \times \left( \frac{|J|}{J_c} \right)^{n-1} \times \frac{\vec{J}}{J_c}$$

In the general form:

$$E = E_c \times \left( \frac{J}{J_c} \right)^n \tag{4.1}$$

where  $E$  is the electric field variable,  $E_c$  is a constant of the electric field at which the DC critical current is defined ( $E_c = 1 \times 10^{-4}$  V/m being the most widely used critical current criterion [15, 73, 83]),  $J$  is the current density variable,  $J_c$  is the critical current density, and  $n$  is the power index.

Thus, the conductivity can be expressed as:

$$\sigma_{fc} = \frac{J}{E} = \frac{J_c}{E_c^{1/n}} \times E^{\frac{1-n}{n}} \quad (4.2)$$

This equation is descriptive for the so-called flux creep state. It is valid for a broad range of  $E$ , but once the current density reaches the flux flow regime [15], the resistivity has been expressed as [84]:

$$\rho_{ff} = \frac{\Delta E}{\Delta J} \approx \rho_n \frac{B}{B_{c2}} \quad (4.3)$$

where  $\rho_n$  is the resistivity in normal state and  $B_{c2}$  is the upper critical magnetic field.

It is still difficult to determine universally when exactly the flux creep ends and flux flow starts. Equation 4.1 cannot be used when  $J \gg J_c(B, T)$  because this would result in an unlimited value for the superconductor's resistivity. The addition of the superconducting material's normal state resistivity  $\rho_{ns}(T)$  (e.g. the resistivity above critical temperature/critical field, which would itself be temperature dependent) in parallel with the resistivity from Equation 4.1 can represent more accurately the real behaviour of the material [85]:

$$\rho_{tot} = \frac{\rho_{HTS}(B, T)\rho_{ns}(T)}{\rho_{HTS}(B, T) + \rho_{ns}(T)} \quad (4.4)$$

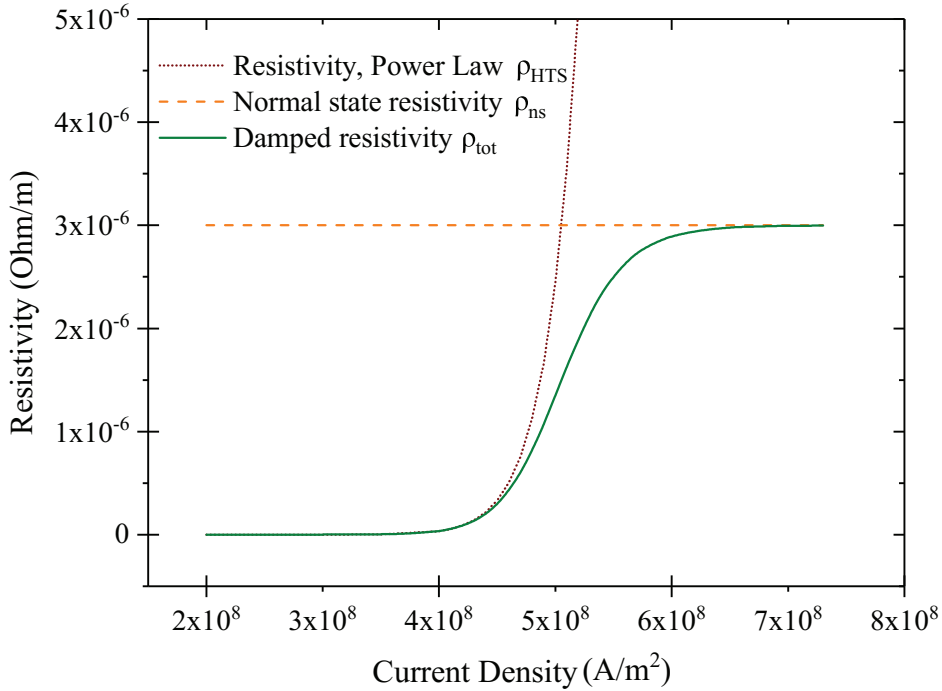


Figure 4.1: This graph shows how Equation 4.4 dampens the unlimited increase of resistivity observed under the power law. The dotted red line represents the resistivity of the superconducting material of one of the tapes used in Chapter 5 (Choi *et al*, Table 5.3). The dashed orange line represents the normal state resistivity (an example value of  $3 \times 10^{-6} \Omega\text{m}$ ) at constant temperature.

where  $\rho_{HTS}(B, T)$  is the resistivity of the superconducting material from the power law. An illustration of this concept, for constant temperature, is shown in Figure 4.1.

### Magnetic Field Dependence of the Critical Current Density

As discussed in the previous chapter, the critical current density depends on the material, as well as on the magnetic field it is subjected to and its temperature. Hence, Equation 4.1 would be incomplete.

There are different methods to model the magnetic field dependence of the critical current.

The most accurate is to use an interpolated function of the magnetic field dependent critical current density, taken from measured data points. In such case a piecewise cubic interpolation of the data in literature can be performed (easily in COMSOL), with the following equation for the critical current density:

$$J_c(B) = J_{c0} \times f(B_{\perp})g(B_{\parallel}) \quad (4.5)$$

where  $J_{c0}$  is the local critical current density at self-field;  $0 < f(B) \leq 1$  and  $0 < g(B) \leq 1$  are the interpolated functions calculating the local critical current density as a function of the perpendicular and parallel magnetic field in Tesla, respectively, normalized by  $J_{c0}$ ;  $B_{\parallel}$  is the parallel component and  $B_{\perp}$  is the perpendicular component of the magnetic field density with respect to the wide face of the tape, respectively (see Figure 4.2).

The same equation may be applied to the  $n$ -index [83].

No proposed analytical function has been universally accepted as an accurate model of the magnetic field dependence. One of the first models has been proposed by Kim [86]

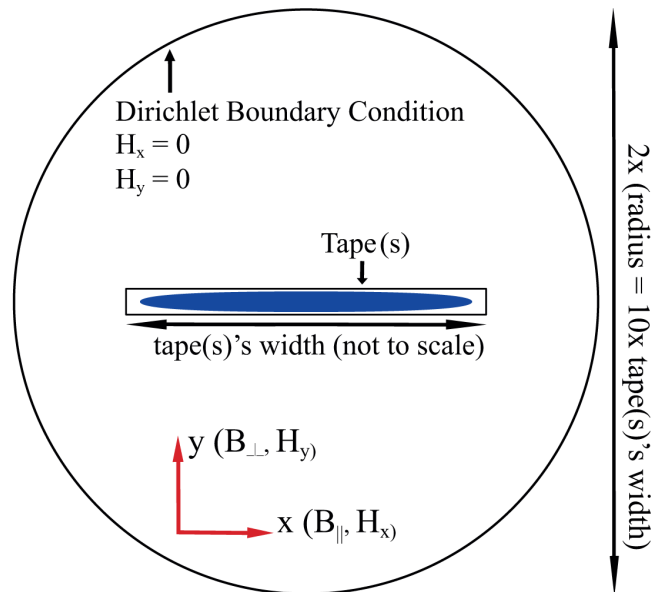


Figure 4.2: Spatial definitions for the 2D FEM model.



and refined by Anderson [87], and is widely referred to as the Kim-Anderson relation [11]:

$$J_c(B, T) = \frac{J_{c0}(T)}{1 + |B|B_0} \quad (4.6)$$

$$n_c(B, T) = \frac{n_0(T)}{1 + |B|B_0} \quad (4.7)$$

where  $B_0$  is a constant,  $|B|$  is the magnitude of the field and  $J_{c0}(T)$  and  $n_{c0}(T)$  are the temperature-dependent self-field critical current density and power index, respectively. This model has been shown to fit measured data poorly in some instances [11] and especially at higher magnetic fields above 4 mT [83]. An option in numerical analysis is a model based on Gaussian distribution of the misalignment of the grains [88]:

$$\frac{I_c(B)}{I_c(0)} = \frac{1 + (B/B_1)^{p_1} + (B/B_3)^{p_3} \times F(\alpha, z_1)}{1 + (B/B_2)^{p_2} + [(B/B_4)^{p_4} + (B/B_5)^{p_5}] \times F(\alpha, z_1)} \quad (4.8)$$

where  $B$  is again the magnitude of the magnetic field,  $F$  is a smoothing function and  $\alpha$  is the direction angle of magnetic field. This method is reported to be very accurate, but complex due to the presence of numerous constants and an additional function that need to be determined.

A more straightforward polynomial fit has been derived in [12] which inherently takes into account the direction of the magnetic field by splitting it into components:

$$J_c(B) = \frac{J_{c0}}{a_1 + b_1 e^{-B_{\parallel}} + c_1 e^{-B_{\perp}}} \quad (4.9)$$

$$n_c(B) = \frac{n_0}{a_2 + b_2 e^{-B_{\parallel}} + c_2 e^{-B_{\perp}}} \quad (4.10)$$

where  $J_{c0}$  and  $n_{c0}$  are the self-field critical current density and power index respectively, with  $B_{\parallel}$  and  $B_{\perp}$  representing the parallel component and perpendicular component of the magnetic field, respectively.

The reference here is to the  $ab$ -planes, which in tapes for power transmission applications in a Cartesian coordinate system are usually correspondent to the  $zx$ -planes, where  $z$ -direction is in the length of the tape, or otherwise the direction of current flow, the  $x$ -direction is the width and  $y$ -direction is the thickness of the tape. Thus,  $B_{\parallel}$  corresponds to  $B_x$  and  $B_{\perp}$  corresponds to  $B_y$  (see Figure 4.2).

Gömöry *et al* [84] have proposed an expanded formula, based on the Kim-Anderson approximation, to consider the magnetic field dependence in a Bi-2223 superconductor, as follows:

$$J_c(B) = \frac{J_{c0}}{\left[1 + \left(\sqrt{\gamma^2 B_{\parallel}^2 + B_{\perp}^2}\right) / B_0\right]^{\beta}} \quad (4.11)$$

where  $J_{c0}$  is the proportionality factor for the growth of the pinning force in very low fields [84] and can be assumed to be critical current density at self-field as per the

Kim-Anderson equation;  $B_0$  is the cut-off value at low fields, otherwise described as the value at which  $J_c = 0.5 \times J_{c0}$  [83];  $\beta$  is a parameter that can describe varying field dependencies [84] and manifests itself via the rapidity of reduction of  $J_c$  [15];  $\gamma$  is the anisotropy factor, which allows to take into consideration that the pinning of flux lines is anisotropic, thus a magnetic field does not affect the superconductivity properties of the material equally in every direction;  $B_{\parallel}$  is the parallel component and  $B_{\perp}$  is the perpendicular component of the magnetic field, respectively.

This may be rewritten as:

$$J_c(B) = J_{c0} \times \left( \frac{B_0}{B_0 + \sqrt{\gamma^2 B_{\parallel}^2 + B_{\perp}^2}} \right)^{\beta} \quad (4.12)$$

It has been shown that Equation 4.12 is capable of simulating the effect on the critical current density of various magnetic fields applied under a range of angles. While only Equation 4.11, which deals with the critical current density, is proposed in [84], the original Kim-Anderson relation of Equation 4.7 suggests that the same extension could be applied to the power index:

$$n(B) = n_0 \times \left( \frac{B_0}{B_0 + \sqrt{\gamma^2 B_{\parallel}^2 + B_{\perp}^2}} \right)^{\beta} \quad (4.13)$$

where  $n_0$  is the self-field power index.

### Temperature Dependence of the Critical Current Density

To achieve even better accuracy, the model can also be extended to include temperature dependence. This is essential for modelling overcurrent response due to the large quantity of resistive dissipation associated with transient faults.

The equations representing the dependence of the critical current on temperature for Bi-2223 [89] and for YBCO [90] superconductors are reported to be of the following form:

$$J_{c0}(T) = J_{c0}(0 \text{ K}) \times \left( 1 - \frac{T}{T_c} \right) \quad (4.14)$$

where  $T_c$  is the critical temperature of the superconducting material (Bi-2223 or YBCO) and  $T$  is the temperature of the material. However, in [90], the considered temperature range is up to 80 K, which is below the critical temperature of YBCO. Thus, a substantial part of the tape behaviour is unconfirmed. A full working range of YBCO is presented in [91], who confirm the following formula:

$$J_{c0}(T) = J_{c0}(0 \text{ K}) \times \left( 1 - \frac{T}{T_c} \right)^{3/2} \quad (4.15)$$

Equation 4.14 is linear while Equation 4.15 has a non-linear zone when  $T$  is approaching  $T_c$ . An assumption will be made that Bi-2223 as well as YBCO superconductors can be described via Equation 4.15, which is supported by  $J_c(T)$  measurements in [52]; furthermore, such an assumption would be in line with the fact that both the Power Law and the magnetic field dependencies described above can be used for both Bi-2223 and YBCO materials. This can be modified to refer to the critical current at liquid nitrogen temperature [92]:

$$J_{c0}(T) = \frac{J_{c0}(T_{LN_2})}{(1 - T_{LN_2}/T_c)^{3/2}} \times \left(1 - \frac{T}{T_c}\right)^{3/2} \quad (4.16)$$

where  $T_{LN_2} = 77$  K is the most common reference temperature for high temperature superconducting properties. In addition:

$$n_0(T) = n_0(T_{LN_2}) \frac{T_{LN_2}}{T} \quad (4.17)$$

In contrast with the magnetic field dependence, the temperature dependence equation is widely accepted in literature.

Formulation	Constitutive Equations	Definitions
Vector and scalar potential $\mathbf{A} - \Phi$	$\mu\sigma\partial\mathbf{A}/\partial t - \nabla \times \nabla \times \mathbf{A} = -\nabla\Phi$	$\mathbf{B} = \nabla \times \mathbf{A}$ $\mathbf{E} = -\partial\mathbf{A}/\partial t - \nabla\Phi$ $\sigma = \sigma(E)$
Current potential $\mathbf{T} - \omega$	$\nabla^2\omega = 0$ $\nabla \times \rho\nabla \times \mathbf{T} = -\mu\partial(\mathbf{T} - \nabla\omega)/\partial t$	$\mathbf{J} = \nabla \times \mathbf{T}$ $\mathbf{H} = \mathbf{T} - \nabla\omega$ $\rho = \rho(J)$
$\mathbf{E}$ -field	$\nabla \times \nabla \times \mathbf{E} = -\mu\partial(\sigma\mathbf{E})/\partial t$	$\partial\mathbf{B}/\partial t = -\nabla \times \mathbf{E}$ $\sigma = \sigma(E)$
$\mathbf{H}$ -field	$\nabla \times \rho\nabla \times \mathbf{H} = -\mu\partial\mathbf{H}/\partial t$	$\mathbf{J} = \nabla \times \mathbf{H}$ $\rho = \rho(J)$

Table 4.1: Different formulations utilized to solve Maxwell's equations [93].

### 4.1.2 Electromagnetics

Different formulations exist for the solution of Maxwell's Equations, see Table 4.1 [93]. Any one of these can fully describe the electromagnetic state of a point in space.

The  $H$ -formulation was selected primarily due to its successful implementation in COMSOL [94–96] for both 2D and 3D. Furthermore, there is a number of other advantages to be considered.

In 3D problems, the  $A - \Phi$  and  $T - \omega$  formulations have four variables while the  $H$ -formulation only has three spatial variables, depending on the coordinate system [93, 94, 97]. Using  $H$ -formulation for 2D allows taking advantage of the fewer variables in 3D by simply expanding the formulation instead of replacing with a completely new formulation. On the other hand, it may be necessary to consider both transport current and applied magnetic field. In this case, an  $H$ -formulation provides direct means to set the boundary values of the magnetic field. Furthermore no differentiation of vector potentials is required as this condition is automatically obtained via first-order edge elements, which improves the accuracy [93, 94] and implicitly satisfies the condition of zero divergence of the magnetic field [93]. In addition,  $A - \Phi$  formulation is shown to be prone to instability since a small change of  $E$  will produce a significant change of  $J$ . The  $H$ -formulation is reported to effectively avoid non-convergence [94].

Writing down Ampere's Law:

$$\nabla \times H = \frac{\partial D}{\partial t} + J \quad (4.18)$$

where  $H$  is the magnetic field,  $J$  is the current density and  $D$  is the time-changing electric displacement field.  $D$  is neglected once it is assumed there are no displacement currents in the given problem, which produces:

$$\nabla \times H = J \quad (4.19)$$

Writing down Faraday's Law:

$$\nabla \times E = -\frac{\partial B}{\partial t} \quad (4.20)$$

where  $B$  is the magnetic field.

Faraday's Law can also be written in terms of the magnetic field:

$$\nabla \times E = -\mu_0\mu_r \frac{\partial H}{\partial t} \quad (4.21)$$

where  $\mu_0$  is the magnetic permeability of free space and  $\mu_r$  is the relative permeability of the material.

The following relation is also known:

$$J = \frac{E}{\rho} \quad (4.22)$$

where  $\rho$  is the resistivity of the material.

Substituting 4.22 into 4.19:

$$\nabla \times \rho H = E \quad (4.23)$$

Substituting 4.23 into 4.21 gives:

$$\nabla \times (\rho \nabla \times H) + \mu_0\mu_r \frac{\partial H}{\partial t} = 0 \quad (4.24)$$

4.24 is the general form PDE that has to be solved for. Since the magnetic field  $H$  is the variable, it is what is called an  $H$ -formulation, and it is valid for both 2D and 3D models.

## 4.2 Implementation of 2D physics within COMSOL with focus on tapes

### 4.2.1 H-formulation

An  $H$ -formulation for COMSOL has been successfully introduced by [96].

Equation 4.24 is not directly created in COMSOL. Faraday's Law (Equation 4.21) is implemented via the 'General Form PDE' module. The field is discretized using first order curl elements [98]. In the same time, Ampere's Law (Equation 4.19),  $J_c(B, T)$ ,  $n(B, T)$  and Ohm's Law (Equation 4.22) are implemented via a variable definition encompassing all domains. The operator  $\text{nojac}(n(B, T))$  is used to exclude the variable from the Jacobian and thus avoid undefined equations in the stiffness matrix that arise from the quick changes of  $n(B, T)$  and its usage as a power index.

#### Initial Conditions

The Initial Values definition includes all the magnetic field variables and their first derivatives. This is set to 0, which is also what COMSOL adds by default.

$$H = \begin{bmatrix} H_x \\ H_y \end{bmatrix} = \begin{bmatrix} 0 \\ 0 \end{bmatrix} \quad (4.25)$$

$$\frac{\partial H}{\partial t} = 0 \quad (4.26)$$

This is the simplest option considering the non-uniform magnetic field that develops within the domains [99].

#### Boundary Conditions

Electromagnetic simulations must obtain results for infinity, however this is impossible and instead it is assumed that some boundary conditions exist at a sufficiently large distance from the area of interest (the tape, or superconducting cable).

A boundary condition must be implemented on all external boundaries. COMSOL adds a Neumann boundary condition by default (Zero Flux), which enforces  $\partial H / \partial t = [0, 0]^T$ , where  $H = [H_x, H_y]^T$ , via  $E = 0$ . This can be used only in the absence of external magnetic field [96], and it is used in that capacity within this study.

Introducing external magnetic fields is possible by explicitly defining a Dirichlet Boundary Condition, which overrides the Zero Flux condition. To introduce a magnetic field,

such that in standard Cartesian notation in 2D Euclidean space  $\vec{B}_{ext} = B_x\vec{i} + B_y\vec{j}$ :

$$\vec{H} = \begin{bmatrix} B_x/(\mu_0\mu_r) \\ B_y/(\mu_0\mu_r) \end{bmatrix} \quad (4.27)$$

where  $\mu_r$  is the relative permeability of the material at the boundary, which is treated as air, hence  $\mu_r = 1$ . If  $B_x = B_y = 0$ , then the Dirichlet condition can be used for applied transport current. The practical difference between the Dirichlet and Neumann conditions is that the former specifies a value at the model boundary, while the latter specifies a derivative — a rate of change. By setting the rate of change of the magnetic field at the model boundary to zero, the boundary can be assumed to be infinitely far away from the area of interest where no change to the variable is observed. Regardless, insignificant effect on AC losses has been observed when changing between the two condition types. Further to that, decreasing the resistance of air to as low as  $\rho_{air} = 1 \times 10^{-4} \Omega\text{m}$  in favour of computation speed produces a negligible difference; this is due to the very large conductivity of the superconductor even at critical currents — even the resistivity of silver is 5 orders of magnitude smaller.

To introduce a current source, the current density on the contact surface can be integrated to determine the total current on that surface:

$$\int_S J_n dS = I_{transport} \quad (4.28)$$

where  $S$  is the surface on which the current is applied to the model,  $J_n$  is the normal component of the current density on this surface and  $I_{transport}$  is the total transport current. Eddy currents do not affect this because the result of integrating them over the entire surface is equal to zero.

Equation 4.28 is implemented within COMSOL via a pointwise constraint such that the integration is performed over the tape's total cross-section. This method can be applied to any surface [94].

## Mesh

The meshing used for 2D simulations of superconductors needs to consider the area of the largest interest. This would be the superconducting material itself, and a relatively fine mesh (element size of 0.02—0.08 mm depending on the element location) is required in that region, so that all fast variations in the dependent and independent variables may be captured. It has been recommended [11] that a mapped mesh should be used. For example, [11] uses a 20x3 mapped mesh within the filaments of a 37-filament tape. However, these have a rectangular shape and a mapped mesh may not be suitable for non-rectangular domains. It was observed that sufficiently accurate results are obtained from a mesh with well-sized triangular elements, while a mapped meshing inside the multifilamentary tapes increases the size of the problem significantly. This is supported

by findings in [12], however the author does give merit to finer meshes for obtaining the current density profile in a tape.

For the air around the model tape, very coarse meshing (element size between 0.4 mm and 1 cm) can be used, because the magnetic field distributions far from the tape are not of interest. The silver matrix is not an area of quick spatial change of variables thus its mesh does not require special attention, however it's minimum density is constrained by the density of the superconductor mesh, especially in multifilamentary tapes.

In any case, the necessary mesh density has to be evaluated on a case-by-case basis. Furthermore, care must be taken to ensure that areas with extremely rapid spatial changes of the variables have an adequate mesh density. This usually is around the edges of a domain, especially when low current is applied.

### Solver, Timestepping and Tolerance

For this Chapter, The COMSOL 5.2a default direct MUMPS solver has been used — later Chapters use COMSOL 5.4's MUMPS (for studies with electromagnetics) and PARDISO (for heat transfer only). The solver has been allowed to do free timestepping, with 100-200 recorded time steps per cycle and a relative tolerance of  $1.0 \times 10^{-4}$ . It has been reported the recommended value is  $1.0 \times 10^{-5}$  [94]. However, decreasing it to this value already increases the size of the problem, the significance of the increase being problem-dependent. Furthermore, sufficiently accurate results are obtained from  $1.0 \times 10^{-4}$ , and a trade-off must occur between computation time and accuracy.

### Power Law

Considering that  $E = \rho J$ , the Power Law (Equation 4.1) can be written in its resistivity form:

$$\rho_{HTS} = \frac{E_c \times |J/J_c(B, T)|^n}{J} + \rho_0 \quad (4.29)$$

That can be modified with the following result:

$$\rho_{HTS} = \frac{E_c}{J_c(B, T)} \times \left| \frac{J}{J_c(B, T)} \right|^{n-1} + \rho_0 \quad (4.30)$$

where  $\rho_0$  is a term, added for numerical stability when passing through zero, such that  $\rho_0 \leq 10^{-2} \times E_c/J_c$  [100]. This can be interpreted as a thermally-activated resistance and typical values for Bi-2223 are  $10^{-14} - 10^{-15}$  [73, 83, 97].  $\rho_0$  was originally introduced for improving convergence in the  $A - V$  formulation [97] and may not always be required in the  $H$ -formulation. An investigation of 2D models showed there is at most 1% influence on the value of the simulation results with no observed instability.

The bounding of the resistivity for high current densities is achieved via Equation 4.4 with an effect as seen in Figure 4.1. Meanwhile, from Equation 4.16:

$$J_c(B, T) = \frac{J_{c0}(0T, T_{LN_2})}{(1 - T_{LN_2}/T_c)^{3/2}} \times \left(1 - \frac{T}{T_c}\right)^{3/2} \times P(B) \quad (4.31)$$

and from Equation 4.17:

$$n(B, T) = n_0(0T, T_{LN_2}) \times \frac{T_{LN_2}}{T} \times P(B) \quad (4.32)$$

where  $P(B)$  could be as per Equation 4.12 (Kim-Anderson) or Equation 4.5 (data interpolation), depending on the choice of the critical current dependence model. Equation 4.30 is implemented via a domain-restricted variable — no COMSOL 'Materials' are used anywhere within the model. The remaining domains are occupied by their respective material's linear resistivity constant.

## 4.2.2 AC losses

The instantaneous AC loss is computed in the unit of  $\text{W}/\text{m}^3$ , via the already discussed equation [15]:

$$Q = J \cdot E \quad (4.33)$$

This equation is utilized to calculate the instantaneous power losses in both the superconducting material and the silver matrix.  $Q$  will subsequently be inserted as a heat source in the heat transfer equations.

To calculate the total losses, a global equation is employed in the following notation [101]:

$$\frac{dQ_{tot}}{dt} = 2Q \quad (4.34)$$

The total power losses  $Q_{tot}$  ( $\text{J}/\text{m}/\text{cycle}$ ) [15] are integrated over the 3rd half-cycle to avoid transient terms that arise from the initial conditions [11, 99] and over the entire surface of the tape  $S_t$ , then doubled to minimize simulation time:

$$Q_{tot} = 2 \int_{1/f}^{1.5/f} \int_{S_t} Q dt \quad (4.35)$$

Regardless of the above consideration, in [65, 66, 94] the time integration starts from  $t = 0$ .

A reasonable assumption is that all losses in the tape are converted to heat — any vibrational or acoustic losses would be insignificant. So Equation 4.35 describes the heat generated by the current inside the tape.



### 4.3 Verification of physics models

The physics implementation in this chapter requires to be verified against published data. This was accomplished by simulating several models and comparing them to existing data. The data was obtained manually via the free online graph data extractor WebPlotDigitizer. This introduces a small error in the extracted data both for  $x$ -axis and  $y$ -axis data due to human imprecision.

Furthermore, these are isothermal experiments, performed in a constant 77 K and thus all temperature dependencies have been neglected.

The models are built in 2D space, with  $x$ -axis and  $y$ -axis being the horizontal and vertical spatial direction respectively. The  $z$ -axis is the out-of-plane direction, in other words into the screen. Any transport currents are applied in the  $z$ -direction, while any external magnetic fields are applied in the  $x$ -direction (parallel  $B_{\parallel}$  fields) or the  $y$ -direction (perpendicular  $B_{\perp}$  fields). The tape in each simulation is placed such that the wide face is lying on the  $x$ -axis and the short face is lying on the  $y$ -axis (Figure 4.3).

#### 4.3.1 Single filament, Bi-2223, Ag-sheathed tape

The first verification of the  $H$ -formulation is against an  $A - \Phi$  method together with practical measurements, as described by Nibbio [83]. The  $B$ -dependent  $J_c$  and  $n$  are utilized using the simplified Equation 4.36 and Equation 4.37.  $J_{c0} = I_c/S$  where  $S$  is the cross-sectional area of the superconductor (Table 4.2). The geometry is a rectangle of superconducting material surrounded by a coating of silver.

The resistivity of silver for the single filament is  $\rho_{silver} = 2.7 \times 10^{-9} \Omega\text{m}$  [102].

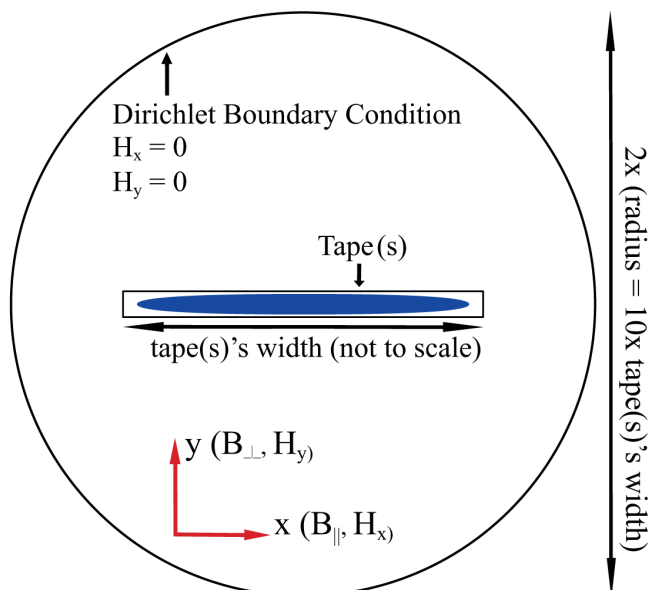


Figure 4.3: Spatial definitions for the 2D FEM model.

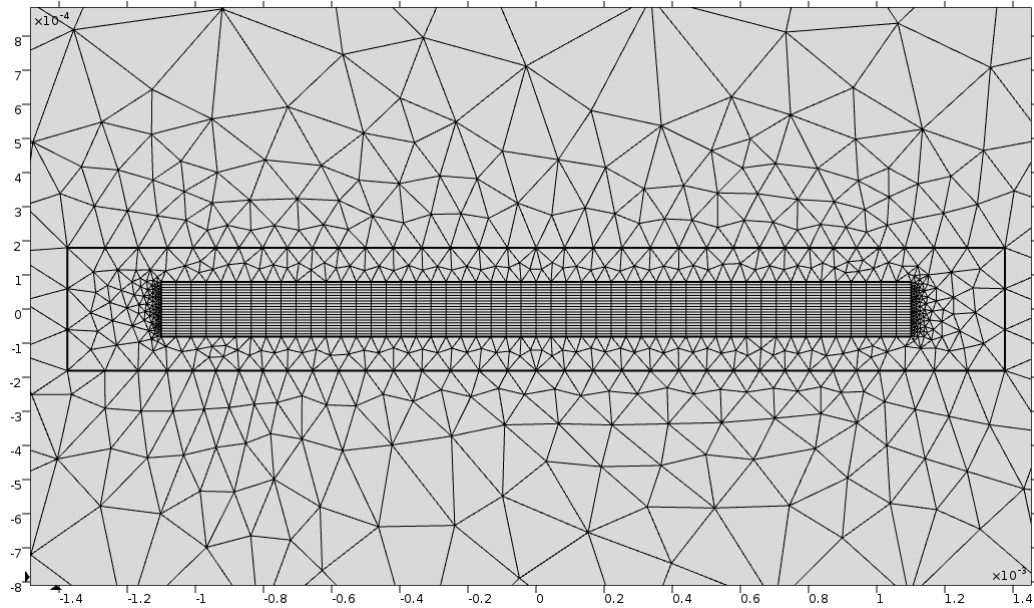


Figure 4.4: The 50x20 nodes mesh used for all simulations of the single filament.

For fields, applied only perpendicularly to the tape, it is possible to simplify Equation 4.12 with the function [12,83] which is essentially the Kim-Anderson relation (Equation 4.6 and Equation 4.7):

$$J_c(B) = J_{c0} \times \frac{B_0}{B_0 + B_y} \quad (4.36)$$

and  $n$  with the function  $n(B)$ :

$$n(B) = n_0 \times \frac{B_0}{B_0 + B_y} \quad (4.37)$$

where  $J_{c0}$ ,  $n_0$  and  $B_0$  are material constants., and  $B_y$  is the magnetic field in the  $y$ -direction.  $J_{c0}$  and  $n_0$  can be interpreted to be the self-field critical current density and self-field power index, respectively. This can be argued acceptable since the transport current used to measure  $J_c$  would always produce self-field, which cannot be eliminated experimentally.

### Applied AC transport current

Using a pointwise constraint integral, Equation 4.28 is applied. This forces a current in the form  $I_t \sin(2\pi ft)$ , where  $f = 59 \text{ Hz}$  and  $I_t$  is the amplitude of the current source.

Tape Dimensions	Bi-2223 Dimensions	Bi-2223 # Nodes	$I_c$ ( $B = 0$ )	$n$ ( $B = 0$ )	$B_0$	$f$
$2.75 \times 0.36 \text{ mm}$	$2.2 \times 0.16 \text{ mm}$	$50 \times 20$	19 A	19	21 mT	59 Hz

Table 4.2: Parameters for single filament verification.

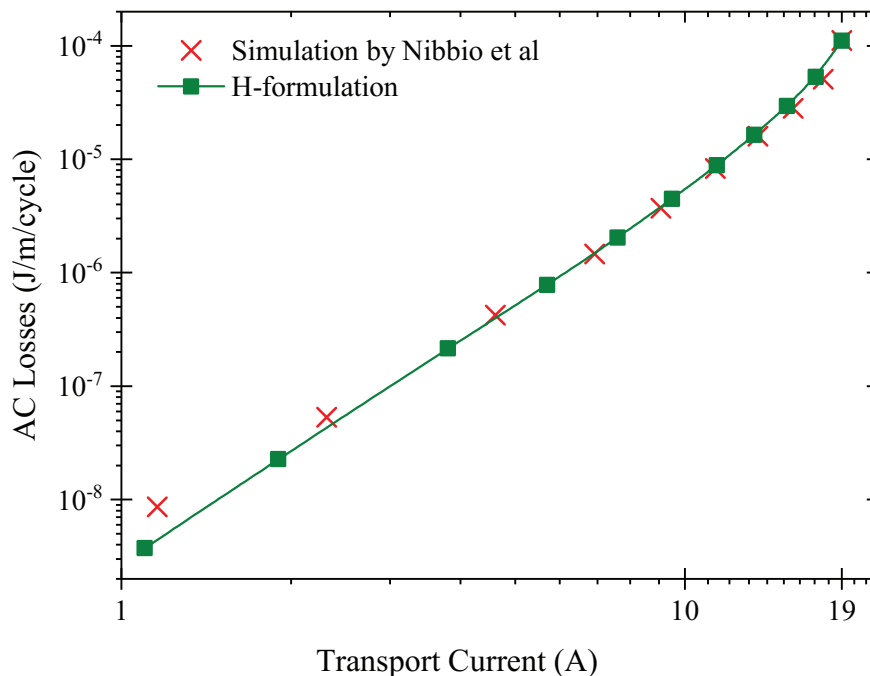


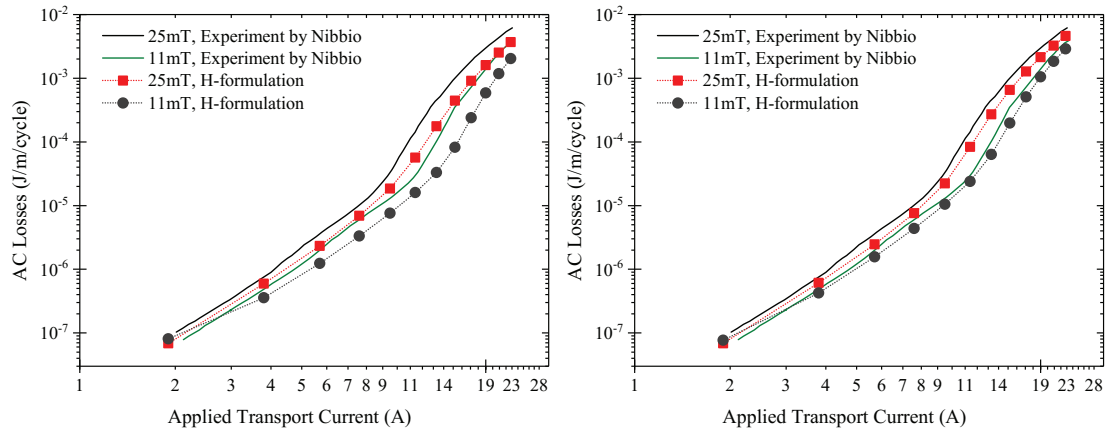
Figure 4.5: Comparison between the simulated AC transport losses and the numerical results of Nibbio *et al.*

The results are shown in Figure 4.5, compared with the Kim-Anderson numerical results of Nibbio *et al* [83]. Around critical current, the simulated values are between 1% and 5% higher than the ones from Nibbio *et al*, with the losses becoming underestimated at low currents, e.g. under  $0.25 \times I_c$ , to an error of about two times less than actual losses. In [83], it is shown that the numerical results in fact are somewhat overestimating the actual measurements for currents larger than  $0.15 \times I_c$ .

### Applied AC transport current in a DC magnetic field

Using a Dirichlet boundary condition, as described in Equation 4.27, a magnetic field perpendicular to the wide face of the tape (along the  $y$ -axis) may be applied, such that  $B_{ext}^{\vec{}} = B_y \vec{j}$ .

The results are displayed in Figure 4.6. When the model for  $J_c(B)$  and  $n(B)$  is used, the predicted losses are severely underestimated (Figure 4.6a). It appears that with the increase in current, the underestimation also increases. The reason for this is the inaccuracy of the fit of the simplified critical current dependency and  $n$ -index model. When an interpolation of the field-dependent properties as provided by [83] is used in the simulation, the gap between the published measurements and the simulated losses is visibly decreased (Figure 4.6b). This shows that, despite all of the remaining three cases of the paper reviewed agree very well with the original experiment, some cases require a precise knowledge of the field-dependent parameters in order to predict the losses accurately. Using an interpolation function may be better than the Kim-Anderson law especially for DC applied fields.



(a) When the Kim-Anderson model is used for  $J_c(B)$  and  $n(B)$ . (b) When an interpolation function is used for  $J_c(B)$  and  $n(B)$ .

Figure 4.6: Comparison between the simulated AC transport losses in a DC magnetic field and the numerical results of Nibbio *et al.*

### Applied AC perpendicular magnetic field

Using a Dirichlet boundary condition, as described in Equation 4.27, a magnetic field perpendicular to the wide face of the tape (along the  $y$ -axis) may be applied, such that  $\vec{B}_{ext} \sin(2\pi ft) = B_y \sin(2\pi ft)\vec{j}$ .

Figure 4.7 displays the results of the simulation, which provides a very tight fit with less than 2% difference between the  $H$ -formulation and the simulated values in [83].

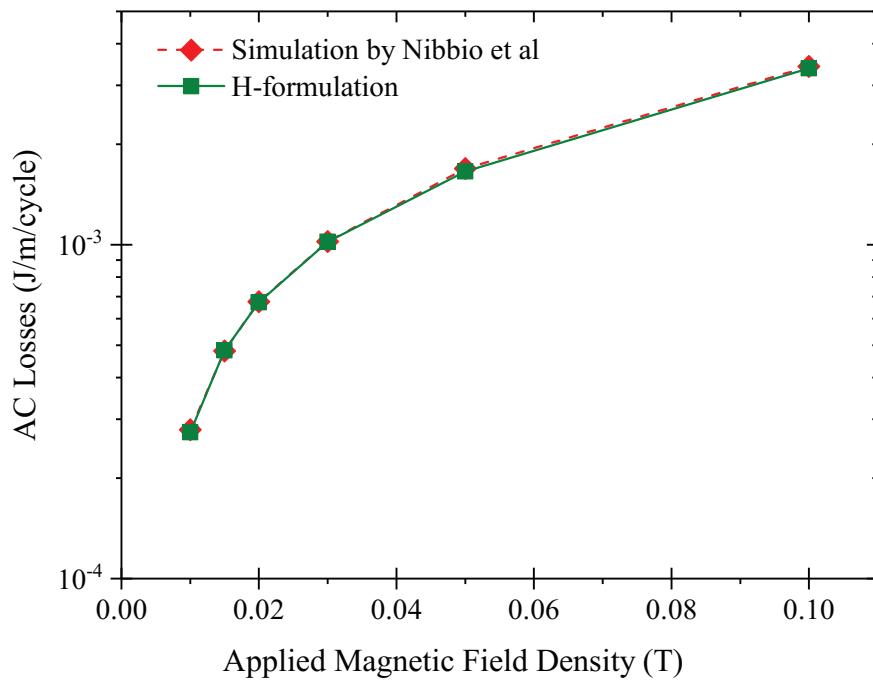


Figure 4.7: Comparison between the simulated and experimental values of the magnetization AC losses in perpendicular magnetic field without any transport current.

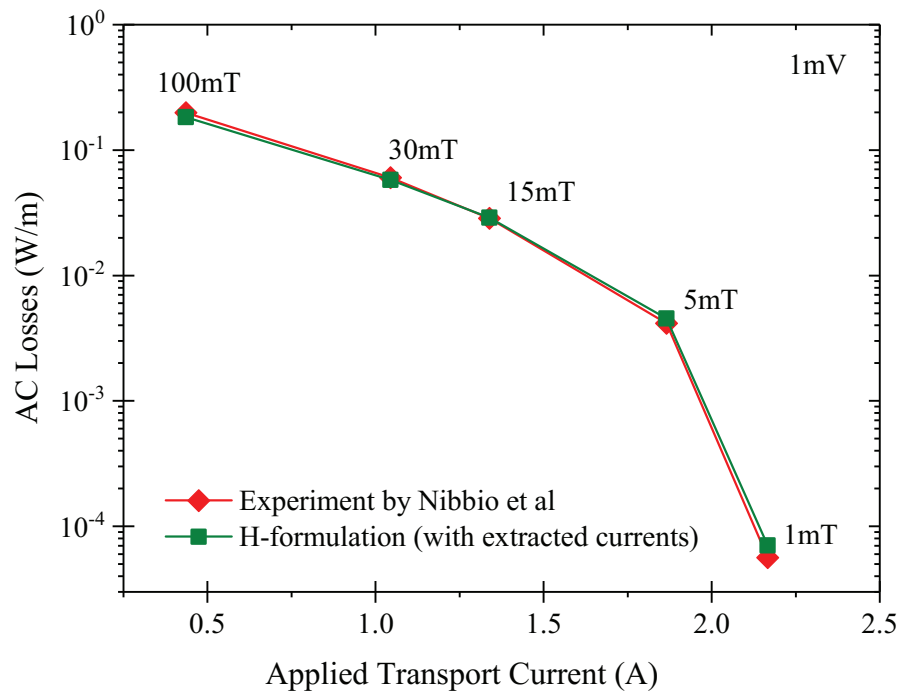


Figure 4.8: Comparison between the experimental AC losses in [83] and the ones simulated in COMSOL, for an applied AC magnetic field together with a transport current. The current is extracted from the relevant figure in the literature.

### Applied AC transport current in external AC magnetic field

The principles described via Equation 4.27 and Equation 4.28 are combined to create a situation where an AC transport current and AC magnetic field are applied together, in phase. The results of these simulations are shown in Figure 4.8 and explained below.

In [83], the transport current is applied via a voltage source, which can be applied out-of-plane in a 2D model only by specifying the electric field. Since there was no published data on the length of the sample, using a voltage source was not possible. Additionally, there was no known method, at the time of modelling, to impose a voltage source on a 2D H-formulation model in COMSOL. Instead, the currents at a given (1 mV) applied voltage were extracted from the literature and simulated directly in order to verify the present modelling technique.

Using precisely the values of the extracted currents (Figure 4.8), the difference between the experimental data and the simulation is between 0% and 8%, with the estimated losses at 1 mT being 20% larger. Hence, the physical model demonstrates acceptable accuracy. The results confirm what is observed in [83] that in higher magnetic fields, the dominating loss is magnetization loss, while the transport loss is almost negligible.

### 4.3.2 Multifilamentary, Bi-2223, Ag-sheathed tape

The second verification of the  $H$ -formulation is against experimental measurements and  $T - \Omega$  numerical simulations, as described by Amemiya *et al* [103]. The Kim-Anderson extended relations for  $B$ -dependent  $J_c$  and  $n$  by G6m6ry *et al* [84] are used for the simulations. Parameters for this tape are shown in Table 4.3.

Due to lack of specific information on the aspect ratio of the 61 filaments or their spatial distribution, the geometry was assumed to consist of equally sized rectangles of superconducting material, the distribution of which is symmetrical around the  $x$ -axis and  $y$ -axis. These are embedded in a silver matrix of overall rectangular shape (summary in Table 4.4 and Figure 4.9). It has been reported that the shape of the filaments does not practically matter, so long that the HTS to silver ratio of the tape and the number of filaments is the same [69]. Furthermore, the shape shown in Figure 4.9 is such due to the difficulty associated with constructing each filament manually; it is not representative of any general model of a tape's multifilamentary region.

The ratio of transport current to critical current is  $i = I_t/I_c$ , the current and the magnetic field are in phase; and  $f = 50$  Hz for the case of transport current only and  $f = 60$  Hz where external field is applied.

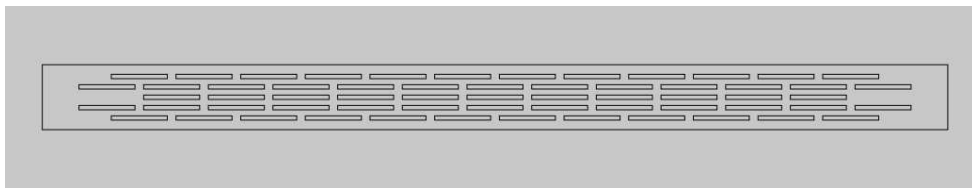


Figure 4.9: The geometry of the multifilamentary tape used in verifications of the  $H$ -formulation.

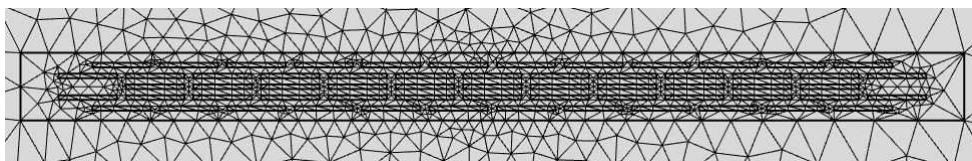


Figure 4.10: The mesh used in the case of multifilamentary tape, used in verifications of the  $H$ -formulation.

Tape	Bi-2223	Filam.	$J_c$	$n$	$\sigma_{silver}$
Dimensions	Total Area	#	( $B = 0$ )	( $B = 0$ )	
$3.5 \times 0.25$ mm	$2.2 \times 10^{-7}$ m <sup>2</sup>	61	$2 \times 10^8$ A/m <sup>2</sup>	19	$3.33 \times 10^8$ S/m

Table 4.3: Parameters for multifilamentary verification.

Aspect Ratio	Width ( $x$ -direction)	Thickness ( $y$ -direction)	$B_0$	Anisotropy $\gamma$	$\beta$
13	216.53 $\mu\text{m}$	16.66 $\mu\text{m}$	0.05 T	0.15	1

Table 4.4: Properties of a filament for the multifilamentary verification.

### Fitting of the critical current's magnetic field dependence

The magnetic field dependence of the critical current density and the power index is presented in [103] in the form of a graph. The model used to approximate these data was the extended Kim-Anderson-Gömöry relation from Equation 4.12.

Data extraction software was once again used for obtaining the numerical values and using them for plotting a comparison to simulated values. The accuracy of the extracted data presented in Figure 4.11a and Figure 4.11b is subject to the resolution of the image it was sourced from and to a minimal human error in selecting the data points.

The anisotropy coefficient  $\gamma$  was manually adjusted for the best fit for both the critical current density and the power index, and the value of  $\gamma \approx 0.15$  was reached. It was observed that increasing or decreasing the value of the anisotropy factor improved the accuracy of one variable and worsened the accuracy of the other variable. Possible solution to this may be using separate anisotropy factors to fit both the critical current density and the power index, however this has not been explored. Any exploration of such an option would suggest research into whether the anisotropy factor must be different for  $J_c$  and  $n$  in the general case of Bi-2223 behaviour or if it is an isolated occurrence.

For the parameter  $B_0$ , it was sought to be observed at what value of the perpendicular magnetic field does  $J_c$  equal half of  $J_{c0}$ . It is clear from Figure 4.11a that  $B_0 \approx 0.05$  T.

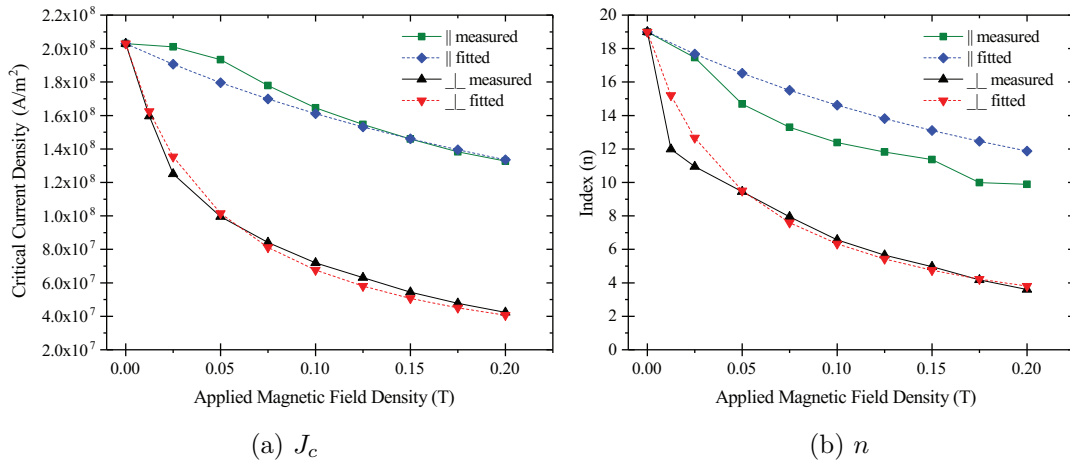


Figure 4.11: Comparison between the measured values in [103] and those plotted with Equation 4.12, with  $\beta = 1$  and  $\gamma = 0.15$ .

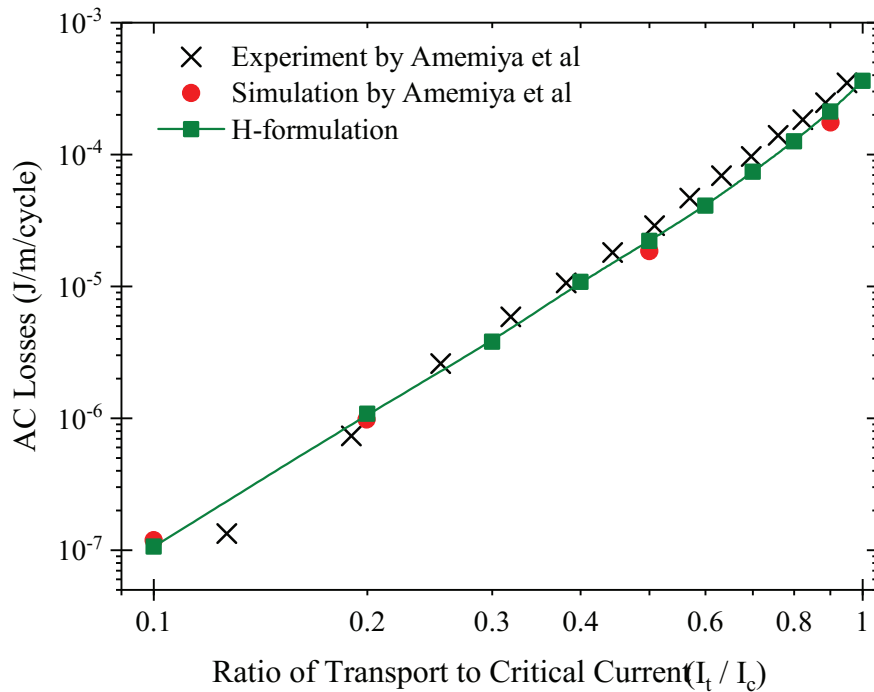


Figure 4.12: Comparison between the simulated and measured values of the AC losses under applied transport current for a range of  $i$ .

The power constant  $\beta$  is simply  $\beta = 1$ . Summary of the parameters for using the Kim-Anderson-Gömöry relation is in Table 4.4.

### Applied transport current

Using a pointwise constraint integral, Equation 4.28 is applied. This forces a current in the form  $I_t \sin(2\pi ft)$ , where  $f = 60$  Hz and  $I_t$  is the amplitude of the current source.

Figure 4.12 shows the summary of simulations where a transport current is applied via a current source. The results show a close match with both measured and numerically calculated losses. Achieved were results that are larger than the numerical simulations by 20% for  $i = 0.9$  and 10% for  $i = 0.2$ , which can be explained by the imperfect critical current dependence approximation. Meanwhile, when compared to the measurements presented, the results demonstrated an underestimation, typically around 14-23%. Under  $i = 2.5$ , the measured losses become smaller. There are no suggestions for this behaviour in [103].

### Applied AC transport current in external AC magnetic field

Using a Dirichlet boundary condition, as described in Equation 4.27, a magnetic field of  $\vec{B}_{ext} \sin(2\pi ft) = B_x \sin(2\pi ft) \vec{i}$ , parallel to the wide face of the tape (along the  $x$ -axis) may be applied, or perpendicular to the wide face of the tape (along the  $y$ -axis), so that  $\vec{B}_{ext} \sin(2\pi ft) = B_y \sin(2\pi ft) \vec{j}$ .



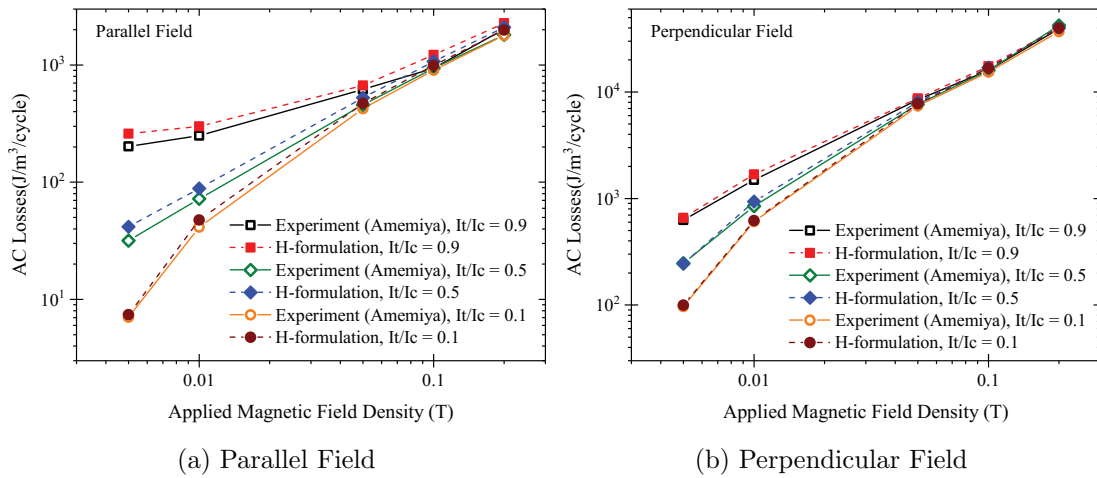


Figure 4.13: Comparison between the simulated and measured values of the AC losses in AC magnetic field for  $i = 0.1, 0.5, 0.9$ .

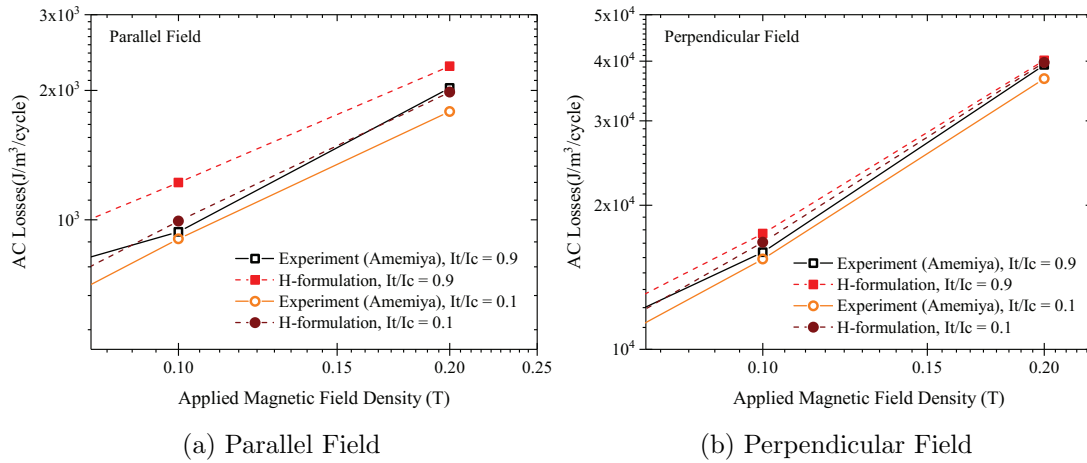


Figure 4.14: Zoomed-in comparison between the simulated and measured values of the AC losses in parallel magnetic field for  $i = 0.9$  and  $i = 0.1$ .

The simulated values for AC loss in a parallel field are in close match with the measured values, as shown in Figure 4.13a. The largest difference between simulated and experimentally measured data from the literature is when  $i = 0.9$ , where the differences are of about 8% to up to 30% in one case. With decreasing the current, the difference also decreases. The difference for all other cases varies between 0% and 16% overestimation, while in only one case when  $B_{ext} = 0.2$  T the losses were underestimated out of line with the remaining cases. The positioning of the filaments and their aspect ratio could affect the losses as well. For the perpendicular field, from Figure 4.13b it can be seen that the simulated values produce a close match with measured values. The error for all cases varies between 1% and 12% overestimation, while in some cases the losses were underestimated.

In Figure 4.14a, a close-up view of the results for large ( $i = 0.9$ ) and very small current ( $i = 0.1$ ) are shown when the applied magnetic field is parallel to the tape. Figure 4.14b shows the same when the magnetic field is perpendicular to the tape.

## Chapter 5

# The homogeneous multifilamentary domain

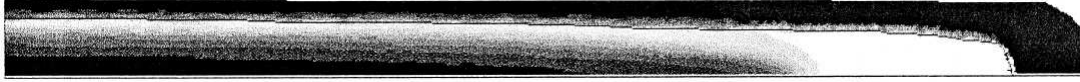
The majority of this chapter, in the shape of a full-length research article, has been published in the journal *Physica C: Superconductivity and its Applications* [104]. An abstract about the same content was presented as an oral presentation at the *6th International Workshop on Numerical Modelling of High Temperature Superconductors*, 25<sup>th</sup>-29<sup>th</sup> June 2018.

Modelling of first generation tapes can be noticeably time-consuming due to the filaments' large number and small size. This is largely caused by the requirement to simulate their exact shape and positioning. Since first generation superconducting cables can have from dozens up to hundreds of tapes, the work required to build the whole cable structure with the help of computer-aided design may be very significant. There are several reasons for that. Firstly, each filament can have an irregular shape, which may not be the same for each tape. Secondly, the construction of hundreds of small domains is cumbersome and prone to errors. Furthermore, and perhaps more importantly, the small size of the filaments enforces very small mesh elements to be used within the superconducting domains in order to capture the correct field penetration. This introduces large amounts of nodes across the entirety of the tape. So the simulation, especially when performed over a useful time in the context of fault response, becomes extremely time-consuming and computationally expensive. On top of that, higher magnetic fields have been observed to increase computation time [94].

At this point, an engineer should ask the question whether it is better to use analytical equations or any other type of numerical modelling technique instead of FEM. From a modelling perspective, the two main issues for the long computational time of first generation tape models are the non-linearity of the superconducting material's E-J relation, and the degrees of freedom (DoF) of the model. The DoF are directly related to the number of dependent variables, mesh nodes and the order of mesh elements. In



(a) Quarter-tape cross-section micrograph of the tape by Amemiya [73]



(b) Quarter-tape cross-section homogenized domain of the tape by Amemiya [73], including shading for current density distribution at  $I_t/I_c = 0.5$ . The darkest areas represent  $0 \text{ A/m}^2$ , and the brightest areas represent  $8 \times 10^7 \text{ A/m}^2$ .

Figure 5.1: The micrograph and homogenized model of Amemiya [73] © 1998 Elsevier. The width of the displayed quarter of the tape is 1.75 mm and the thickness is 0.125 mm, details in Table 5.1.

turn, the mesh nodes are proportional to the level of detail of the applied mesh, and to properly discretize each filament a very detailed mesh is required. A way to loosen that requirement is to simplify the geometry, or in other words, to *homogenize* the superconducting filaments into one large domain. Such a *homogenized domain* may noticeably decrease the computation time not only for first generation tapes and cables, but also any other first generation multi-tape devices.

The objective of this chapter is to characterize a homogenization technique for AC power loss estimation of multifilamentary first generation tapes with straight filaments, such that it decreases the problem size compared to a full multifilamentary model. In addition, the level of accuracy it provides in the calculation of the AC transport current loss over a range of applied currents is investigated.

## 5.1 Proposed homogenization technique

The homogeneous technique for modelling Bi-2223 tapes, described in this section, can be found originally in [71], where the matrix material is ignored in AC loss modelling. It is also briefly explained in [72], but not in the context of AC loss modelling.

Appropriate homogeneity can be obtained when the simulated superconducting domain has the approximate shape of the real tape's multifilamentary region. For simplicity and where applicable, the multifilamentary region can be approximated to be a classical ellipse, and its dimensions can be obtained from the tape's micrograph (Figure 5.3 — the shaded areas in both (a) and (b) represent the homogeneous superconducting domain). These dimensions must be such that all filaments are located within the rectangle, described by them. Since here the cross-sectional area of the homogenized domain is larger than the real area of superconductor, it must be ensured that the current is correctly distributed in the cross-section. This can be achieved by scaling the

local critical current density in self-field  $J_{c0}$  in all cases such that:

$$J_{c0} = I_c/S_{eq} \quad (5.1)$$

where  $S_{eq}$  is the area of the filamentary-equivalent domain used in the model and  $I_c$  is the critical current for the given tape. The scaling ensures that the current in any part of the homogenized domain is very similar to the average current in equivalent part of the real tape. Therefore, the homogenization model should correctly describe local magnetic field.

It is expected that the shape of the homogeneous region is linked to the shape of the multifilamentary region, particularly when exposed to external magnetic fields (i.e. a rectangular homogeneous region will represent a rectangular multifilamentary region; however, this has not been proven or disproven).

To verify the homogenization method, the prediction can be compared with published experimental data. Of particular interest are studies with AC loss measurements in external field and studies with more than one tape.

This homogenization technique is not applicable to tapes with decoupled filaments, such as those with twisted filaments.

To verify the homogenization method, the loss prediction can be compared with published experimental data. The requirements for tapes from the literature to be modelled are the presence of sufficient data about the geometry, the magnetic field dependence of the critical current, and the transport current losses within the tape. Micrographs, numerical models and measurements in applied external field would also be beneficial, but not essential. The majority of papers that investigate AC power losses do not provide either one or more parameters, which means scientifically sound verification of the homogenization technique would not be possible.

## 5.2 2D verification of the homogenization technique

The most important parameters of the modelled tapes are listed in Table 5.1, 5.3 and 5.4. They have been taken directly from the literature and some of them have been derived from other known parameters. In all tapes, the superconductor is straight Bi-2223 and the sheath is silver, unless specified otherwise.

The critical current dependence of the magnetic field was implemented via an interpolation function of the data in literature (Figure 5.4), as described in Section 4.2.1. In all of the AC transport current in self-field simulations in this study, the largest local magnetic field does not exceed 30 mT.

Different meshing densities were used, as seen in Figure 5.2. The purpose was to quantify the difference in degrees of freedom and simulation time between meshes with different number of nodes. It could have been possible that an accurate simulation may require

a significant number of degrees of freedom regardless of the homogenization, and it must be ensured that the proposed techniques offer a noticeable computational benefit compared to the fully multifilamentary models.

The simulations in this chapter were performed on a desktop PC with Intel i7-6700 CPU, 3.40GHz, with 16 GB of RAM.

### 5.2.1 61-filament, Bi-2223, Ag-sheathed tape — Amemiya *et al*

#### Description

The first tape is one by the research group of Amemiya *et al* [73,103], and is hereafter referred to as "Amemiya". It is the same tape as in Subsection 4.3.2, used for initial verification of the numerical technique.

The provided resistivity of silver in [103] is  $3 \times 10^{-9} \Omega\text{m}$ . Amemiya *et al* also provide the area of the superconductor, as well as the area of the multifilamentary region, but

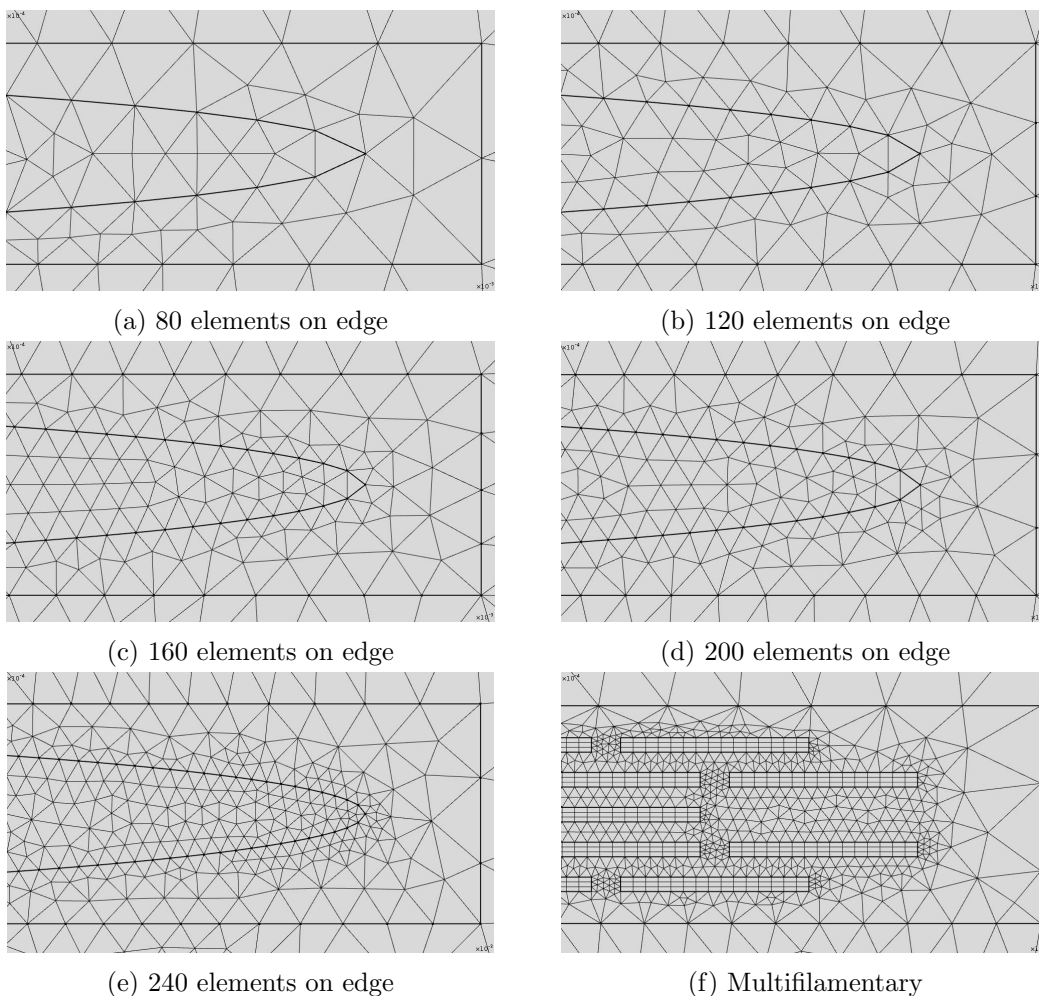


Figure 5.2: Comparison between mesh densities in Amemiya *et al*, as in Table 5.2. The presented images display only the right end of the tape.



(a) Quarter-tape cross-section, Amemiya *et al* [73] ©1998 Elsevier. The width of the displayed quarter of the tape is 1.75 mm and the thickness is 0.125 mm, details in Table 5.1.



(b) Full tape cross-section, Choi *et al* [68] © 2004 IEEE. The width of the displayed full tape is 3.1 mm and the thickness is 0.17 mm, details in Table 5.3.

Figure 5.3: Micrographs of the tapes, by Amemiya *et al* and Choi *et al*. No micrograph available by Ryu *et al*. The shaded red areas (original work) represent the homogenized superconducting domain.

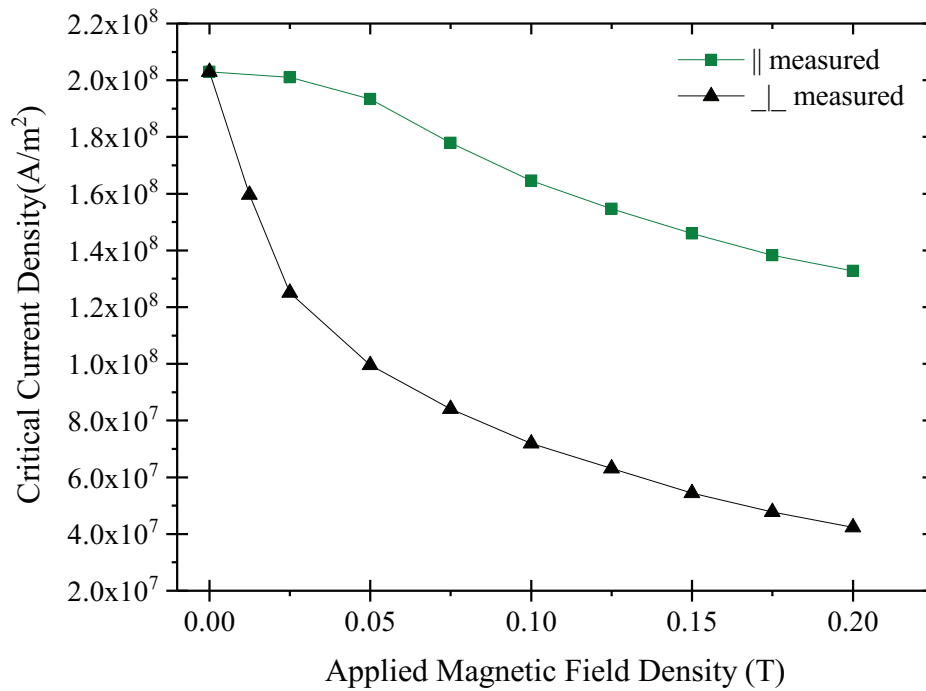


Figure 5.4: Measured by Amemiya [103] magnetic field dependency of the critical current. The y-axis is normalised by the critical current density at zero field.

do not provide the dimensions for it. Thus, the dimensions were obtained from the micrograph in Figure 5.3a. Provided are also AC total losses of the tape when subjected to an external magnetic field (see Figure 5.4 for the  $J_c$  dependence on the field), and appropriate models have been built and simulated to explore the filamentary-equivalent domain's accuracy in this case.

## Results

In terms of AC transport current losses, at  $I_t/I_c = 0.94$  the model provides 0.327 mJ/m/cycle while the original measured loss is 0.349 mJ/m/cycle. This accuracy is maintained for peak transport currents above  $I_t/I_c = 0.3$ . As it can be seen in Figure

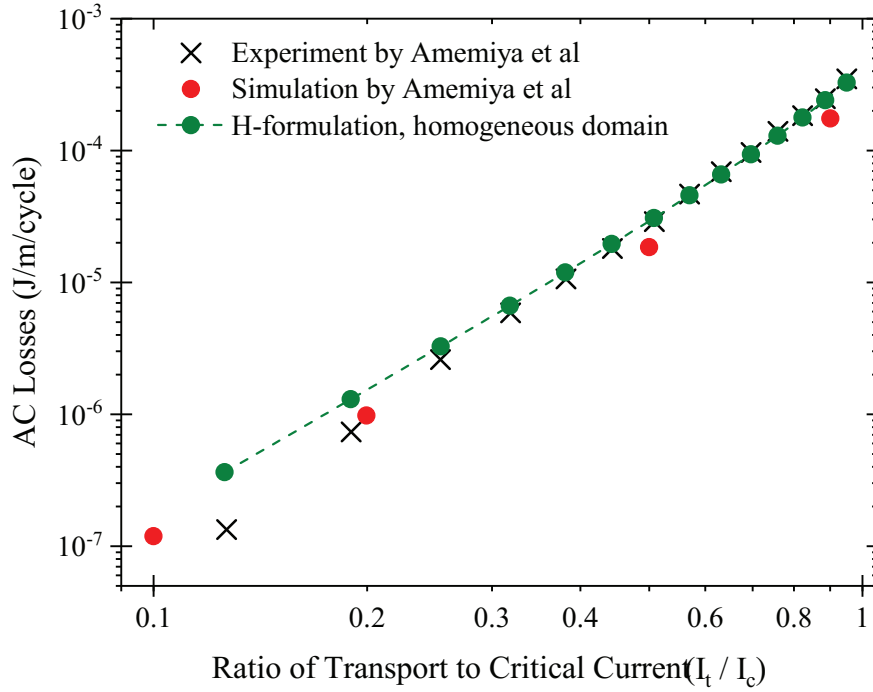


Figure 5.5: Comparison between the AC transport current losses in [103] and the simulations. The mesh has 240 boundary mesh elements as in Figure 5.2e.

5.5, the losses at peak transport currents under  $I_t/I_c = 0.3$  of the transport current are somewhat overestimated. This has been noted in [103] but no explanation is provided. A similar result is obtained from the fully multifilamentary model and the slope of the numerical model by Amemiya *et al* closely resembles the slope of the homogenized model, but is displaced uniformly towards lower values of the loss. This means this discrepancy is not connected to the homogenization model but rather numerical simulation as a whole, perhaps model input data or the physical equations. Since loss measurements at low currents are very sensitive, it is also a possibility that the authors' experiment has underestimated the losses.

	Tape dimensions, $w_t \times h_t$	3.5 mm $\times$ 0.25 mm
	Superconducting area, $S_{SC}$	$2.2 \times 10^{-7}$ m <sup>2</sup>
	Critical current, $I_c$	44.66 A
Amemiya	$n$ -index	19
[103]	Number of filaments	61
	Frequency ( $I_t$ only)	60 Hz
	Frequency (with $B_{ext}$ )	50 Hz
	Resistivity of silver	$3 \times 10^{-9}$ $\Omega$ m
	Multifilamentary region size	3.23 mm $\times$ 0.2 mm
	Multifilamentary region type	Ellipse

Table 5.1: Parameters for the tape by Amemiya [103].

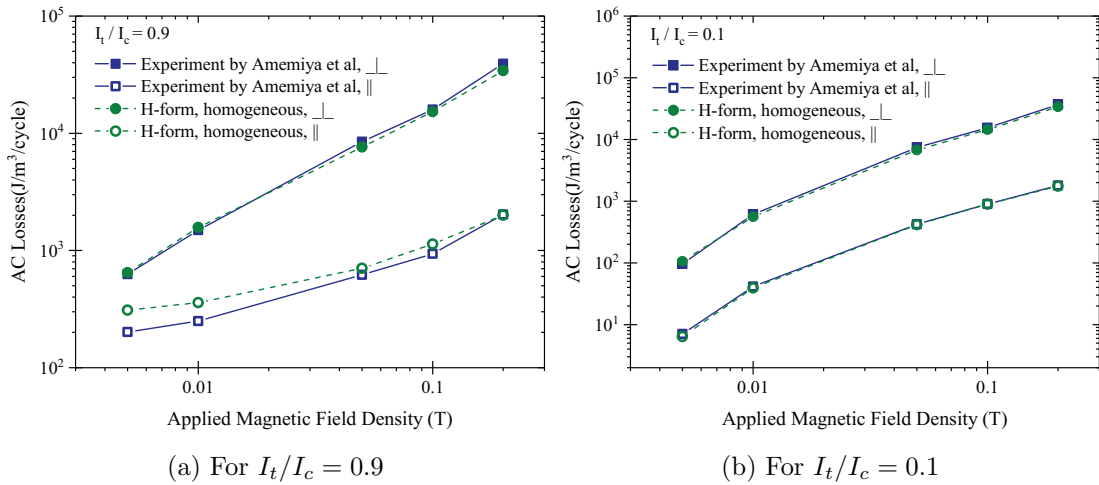


Figure 5.6: Predicted AC total losses in the Amemiya tape in applied external magnetic field. The mesh has 240 boundary mesh elements as in Figure 5.2e.

Mesh Density	Time (seconds)	Degrees of Freedom
<b>Amemiya</b>		
Homogenized	314	5512
Multifilamentary	2406*	16894
<b>Choi</b>		
Homogenized	668	12952
Multifilamentary	2406*	35307

Table 5.2: Time and degrees of freedom required in simulations of the homogenized and multifilamentary model in Amemiya and Choi with transport current equal to the critical current, in self-field.

\* - the numbers are the same, which is coincidental and not an error.

Figure 5.6 compares the results from the homogeneous model with measurements from literature, subjected to perpendicular and parallel magnetic field with  $I_t/I_c = 0.9, 0.1$ . Figure 5.7 illustrates the current distributions (based on the same superconducting area) in the homogeneous and the multifilamentary tape at  $B_{\perp} = 0.1$  T and  $I_t/I_c = 0.9$  — it demonstrates that the same current distribution can be achieved in both models.

At the beginning of the cycle (assume  $t = 0$  s and the simulation has already been running for at least one cycle), there is no current and the applied magnetic field  $B_{\perp}(0) = B_{\perp max} \sin(0) = 0$  where  $B_{\perp max} = 0.1$  T is the peak value of the applied field, though there is still a field gradient  $dB_{\perp}/dt \propto B_{\perp max} \cos(0)$ , which, together with the superconductivity, induces a perfectly symmetrical current within the superconducting domain. As the transport current in the tape starts to rise, it expands the zone of current flow that matches the direction of the transport current while decreasing the zone of current that flows in the opposite direction. This can be illustrated by the red



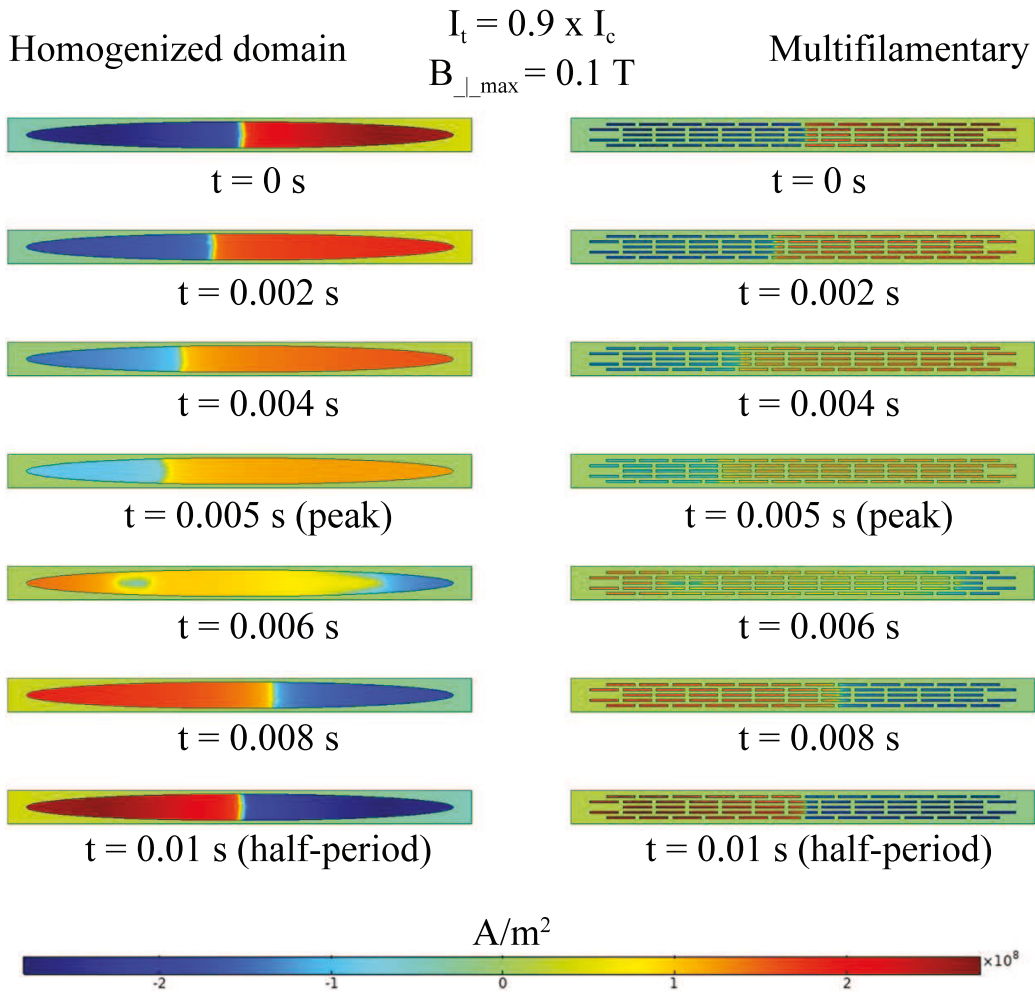


Figure 5.7: Comparison between the current densities in the homogenized and multifilamentary model of Amemiya’s tape when the peak applied magnetic field is equal to  $B_{\perp \max} = 0.1 \text{ T}$  and  $I_t/I_c = 0.9$  at various times. The frequency is 60 Hz and thus one period is 0.02 s. The current density in the homogenized part of the figure is multiplied by  $(S_{eq}/S_{hts})$  where  $S_{hts}$  is the total area of the superconducting material in the multifilamentary model — this allows for the values of  $J$  to be compared directly.

area expanding: it contains both the transport current and the part of the induced current that matches the direction of the transport current. Since the transport current is sufficiently below critical, it is not required to distribute uniformly.

Once the peak of the wave of the current/applied field is reached at  $t = 0.005 \text{ s}$ , the applied field begins to decrease, and under the principle of electromagnetic induction the direction of the induced current flips. This change of direction, together with the decrease of transport current, explains why the red zone (positive current flowing into the screen) moves to the other half of the tape and itself starts to decrease. Once the transport current is equal to zero at the half-period ( $t = 0.01 \text{ s}$ ), the induced currents are symmetrical within the tape.

The observed magnitudes of induced current at maximum applied field ( $t = 0.005$ ) and at zero applied field ( $t = 0$  s and  $t = 0.01$  s) are consistent with the principle of electromagnetic induction. As the derivative of  $\sin(t)$  is  $\cos(t)$ , the largest rate of change is offset by quarter of a period (0.005 s). Then, the highest EMF is induced when the rate of change of the magnetic field is the highest, and the lowest EMF is induced when the rate of change of the magnetic field is the lowest.

At  $B_{ext} = 0.05$  T and  $I_t/I_c = 0.9$ , the value of the simulated loss is  $7620$  J/m<sup>3</sup>/cycle and of the measured loss is  $8463$  J/m<sup>3</sup>/cycle for perpendicular field (10% underestimation); under the same conditions but for parallel field, the simulated loss is  $705$  J/m<sup>3</sup>/cycle and the measured loss from literature is  $618$  J/m<sup>3</sup>/cycle, giving 13% overestimation.

To demonstrate the efficiency of the proposed homogenization, the simulation time was considered at  $I_t = I_c$  for a number of mesh densities and for a full multifilamentary model. It is evident from Table 5.2 that the filamentary-equivalent domain model is significantly faster than the full multifilamentary model. All mesh densities achieve an accuracy of 5% or better when compared to the measurements from [103] when the simulations were repeated with  $I_t/I_c = 0.95$ . A bottom limit for achieving well-matching losses is at as little as 40 boundary elements. The selection of mesh density has implications beyond accuracy, as insufficiently fine meshing can even fail to converge when there are very large gradients in the geometry it is discretizing. Furthermore, it was observed that the time taken to simulate the model is directly proportional to the

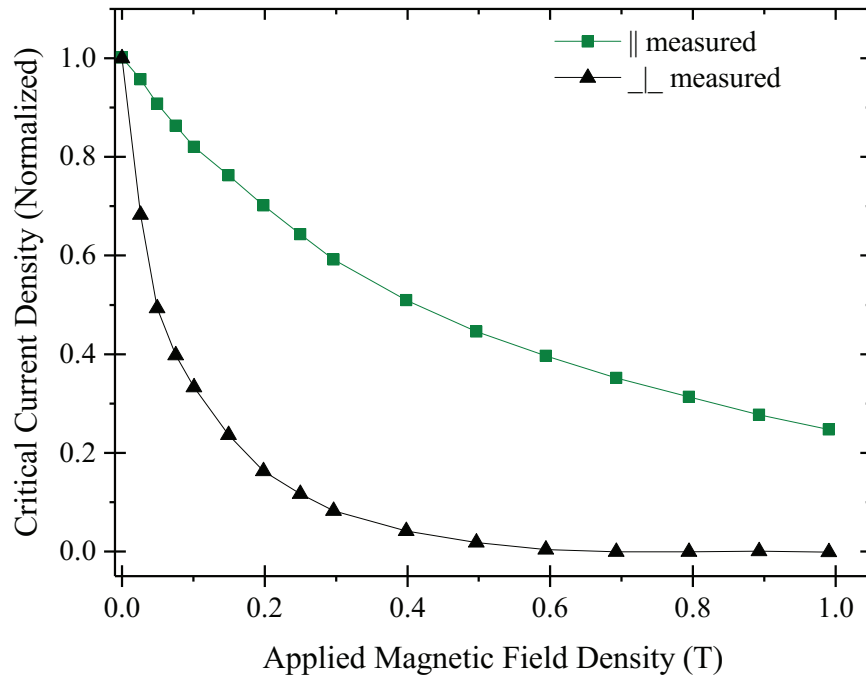


Figure 5.8: Measured by Choi [68] magnetic field dependency of the critical current. The y-axis is normalised by the critical current density at zero field.

	Tape dimensions, $w_t \times h_t$	3.1 mm $\times$ 0.17 mm
	Critical current, $I_c$	78 A
Choi	$n$ -index	20
[68]	Number of filaments	55
	Frequency	50 Hz
	Resistivity of silver [102]	$2.7 \times 10^{-9} \Omega\text{m}$
	Superconducting area, $S_{SC}$	$1.84 \times 10^{-7} \text{ m}^2$
	Multifilamentary region size	2.94 mm $\times$ 0.12 mm
	Multifilamentary region type	Ellipse

Table 5.3: Parameters for the tape by Choi [68].

applied current (observations made up to critical current).

### 5.2.2 55-filament, Bi-2223, Ag-sheathed tape — Choi *et al*

#### Description

The second tape is by the research group of Choi *et al* [68, 105] (referred to as "Choi"), where the authors examine the transport losses of three identical tapes, attached to each other with their short sides. The authors provide the dimensions of the superconducting region, but not the area of the superconductor itself. Instead of using this data, the fraction of the superconductor of the whole tape's cross-section and the multifilamentary region's dimensions was obtained via image analysis of the micrograph (Figure 5.3b). See Figure 5.8 for the  $J_c$  dependence on the field.

#### Results

Figure 5.9 displays the total transport current losses, compared to the measurements from the literature. There is practically no difference (less than 1%) between the homogeneous model and both the experimental measurements and the data from simulation in the literature. This demonstrates that the homogenization technique can be used to accurately model the total losses in more than one tape, however the literature does not provide useful data about the loss distribution between the tapes.

To demonstrate the efficiency of the proposed homogenization, the simulation times and degrees of freedom of the homogenized and full multifilamentary model of the Amemiya and Choi tapes are presented in Table 5.2. It is clear that the filamentary-equivalent domain model is significantly faster than the full multifilamentary model even at a relatively fine mesh such as the one from Figure 5.2e.

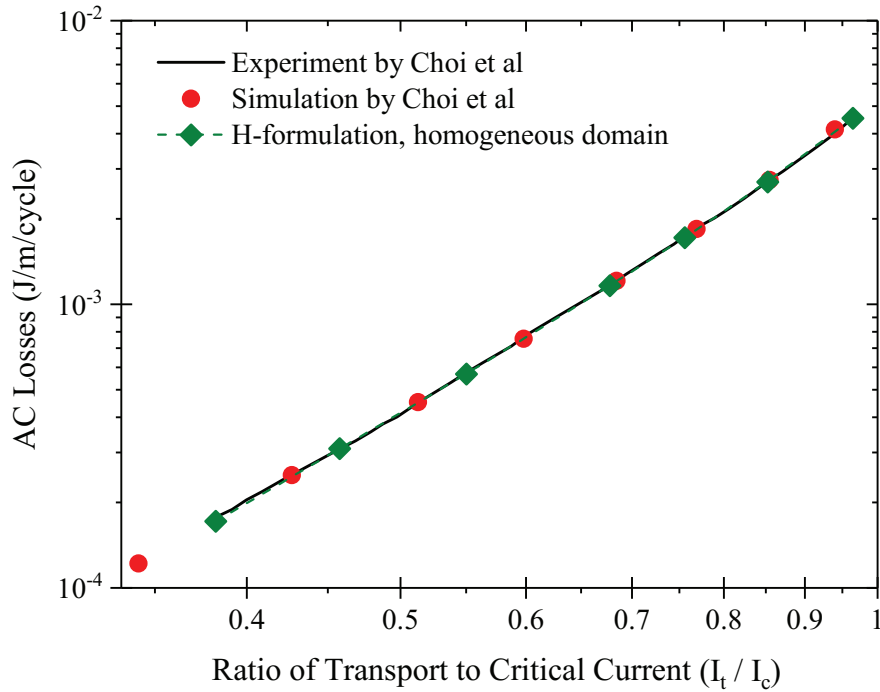


Figure 5.9: Comparison between the AC transport current losses in [68, 105] and the simulations. The mesh has 240 boundary mesh elements as in Figure 5.2e.

### 5.2.3 Circular multi-tape conductors — Ryu *et al*

#### Description

The third and fourth tape are described by Ryu *et al* [106] and Ma *et al* [70] and are named "Ryu-A" and "Ryu-B" for the lower and higher critical current carrying tape, respectively. The configuration of these tapes is a circular conductor of 10 non-twisted tapes, arranged such that the tapes form a regular decagon (Figure 5.11). Then, a number of modes are provided, of which two are the most interesting — Single Mode and Simultaneous Mode. Single Mode is where only one tape, called Tape 1, has been energized. Simultaneous Mode is similar to a cable conducting current, as it is where all tapes have been energized; only the losses in Tape 1 are considered.

The authors provide the area of the superconductor and the dimensions of the multifilamentary regions, but no micrographs. Hence, the homogenized region has only been simulated via the provided values. Furthermore, in these two tapes, the anisotropy of the magnetic field dependence is not provided, and thus, it is assumed to be approximately equal to 0.12 as it is the average value between Amemiya and Choi. See Figure 5.10 for the  $J_c$  dependence on the field. The sheaths in Ryu-A and Ryu-B are made from an Ag alloy, but due to lack of more information are assumed to be silver only. The resistivity of silver is assumed to be  $\rho_{silver} = 2 \times 10^{-9} \Omega\text{m}$  [102]. The former, i.e. the supporting core of the tapes, is reported to be made of plastic [107], albeit the study in question

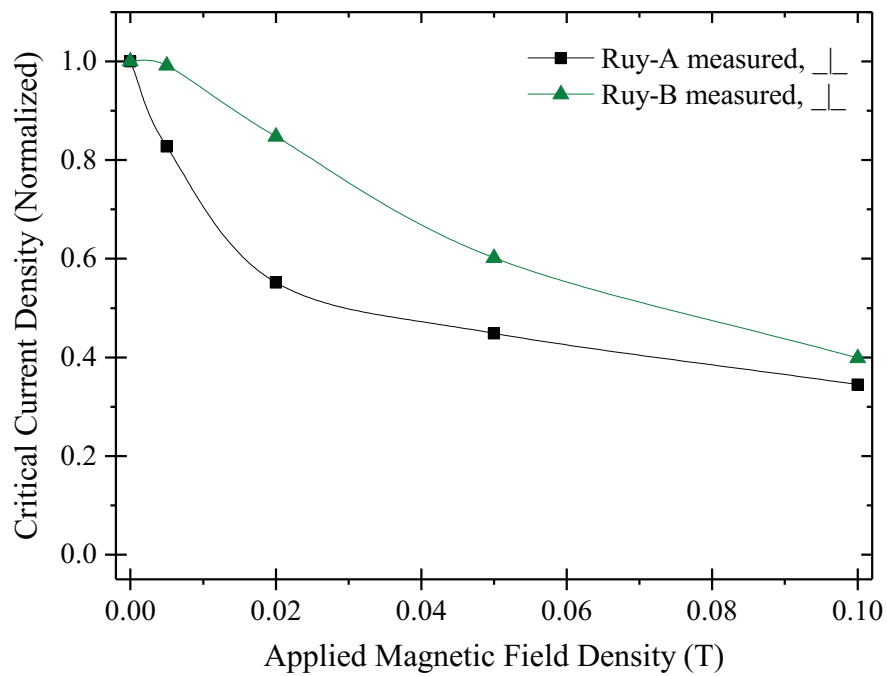


Figure 5.10: Measured by Ryu [106] magnetic field dependency of the critical current. The y-axis is normalised by the critical current density at zero field.

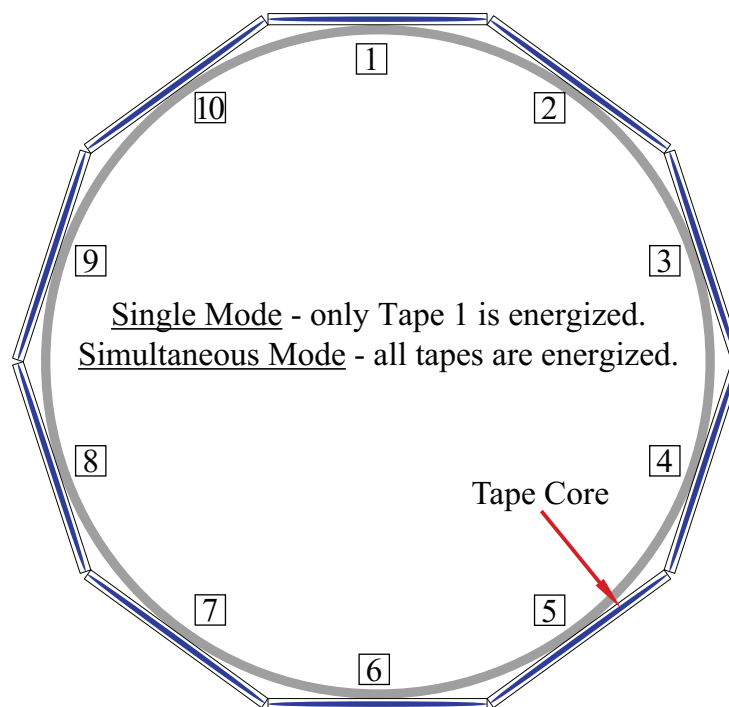


Figure 5.11: The cross-section of the configuration of the 10-tape conductor, as per Ma *et al* [70]. The shape is a regular decagon.

	Tape dimensions, $w_t \times h_t$	3.9 mm×0.3 mm
	Superconducting area, $S_{SC}$	$3.159 \times 10^{-7} \text{ m}^2$
	Multifilamentary region size	3.7 mm×0.26 mm
Ryu-A	Critical current, $I_c$	24.2 A
[70, 106]	$n$ -index	10.4
	Number of filaments	37
	Frequency	500 Hz
	Tape dimensions, $w_t \times h_t$	4.1 mm×0.21 mm
	Superconducting area, $S_{SC}$	$3.27 \times 10^{-7} \text{ m}^2$
	Multifilamentary region size	3.9 mm×0.154 mm
Ryu-B	Critical current, $I_c$	129.85 A
[70, 106]	$n$ -index	16.18
	Number of filaments	55
	Frequency	300 Hz

Table 5.4: Parameters for the tapes by Ma [70] and Ryu [106].

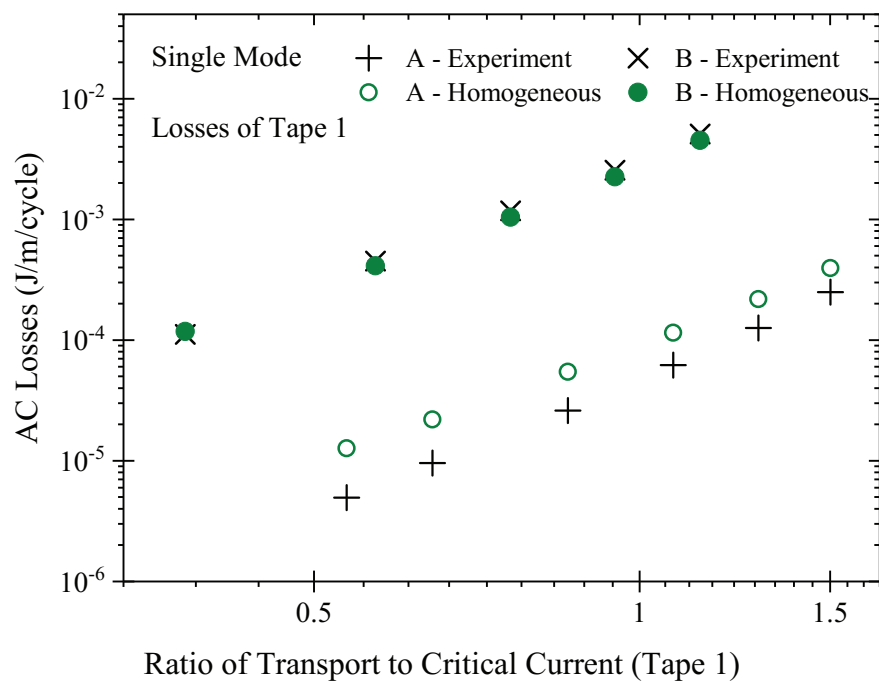
does not use exactly the same tapes. Due to material properties of the plastic not being available, the former has been assumed to be air.

## Results

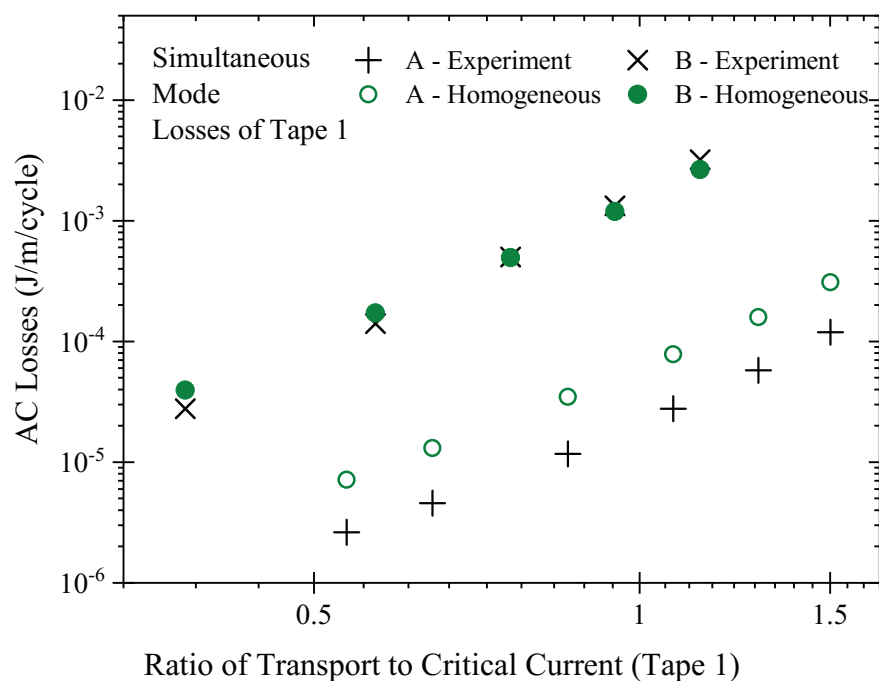
According to Ma *et al* [70], Single Mode is similar to a single tape in self-field. If in Single Mode simulations the pointwise constraint integrals in the remaining tapes are left undefined, net flowing currents will be induced in the neighbouring tapes. This would of course be impossible, as these tapes are not part of a closed circuit. In turn, this will increase the mutual inductance and decrease the critical current density in Tape 1, especially around the edges of the tape that are closest to its neighbours. To avoid loss distortion, the model should put the non-energized tapes floating via setting the pointwise constraint current integrals to zero, such that only induced eddy currents could flow.

The simulation results for the Ryu tapes are presented in Figure 5.12. The losses in both Single and Simultaneous mode of Ryu-A are noticeably overestimated approximately equally throughout the range of transport currents. In contrast, the estimated losses in Ryu-B for both modes display close agreement with measurements from literature.

A possible cause for the discrepancy between the predicted losses and the losses provided by the literature may be the assumption that the tapes' matrices are entirely made of silver, while in fact they are made out of unspecified (different) alloys that may possess different resistivity. Moreover, the former's material and dimensions would influence the current distributions within each tape, and thus — losses. Additionally, the setups



(a) Single Mode — losses for only one tape.



(b) Simultaneous Mode — losses for only one tape.

Figure 5.12: Measured by experiment in [70] and simulated (original) AC losses in Ryu-A (hollow symbols) and Ryu-B (filled symbols). 240 boundary mesh elements.

used are in the high frequency range, which may introduce further complications, such as noticeable skin effect or increased eddy current loss, which has not been taken into account. Finally, the measurements of the AC losses in [70] are performed via the

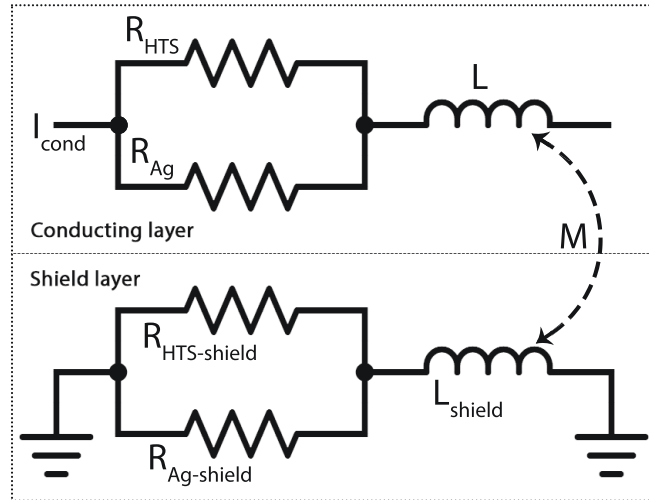


Figure 5.13: The equivalent circuit arrangement of the MATLAB model.

voltage tap method, which is suited for transport loss measurement [108]. Hence, in this particular case it might not have captured fully the effect that circulating currents, resulting from the electromagnetic interaction with neighbouring tapes, would have on the total losses. This may be contributing to the discrepancy between measured and predicted values of the loss, especially considering that Ryu tapes are the least well characterized tapes of those presented in this paper.

### 5.3 The homogenization technique at currents above critical current

The results from modelling transport power loss in multiple first generation tapes, including in applied field and in cable configurations, suggest the homogenization technique is appropriate for modelling large devices such as power cables. However, the result of Ryu-A is not satisfactory, and therefore further investigation may be necessary. In this section, the results of the constant critical current loss simulations in COMSOL of a sample power cable using the homogenization technique are compared to an analytic equivalent circuit calculation of the same cable, built in MATLAB.

#### 5.3.1 Equivalent circuit modelling of a superconducting cable

Approximating transport current losses of an HTS cable via equivalent circuit is narrowed down to determining constants (i.e. geometry and inductances) and dynamic variables (conductivity of superconductor), as well as defining the relationship between them; finding the current distribution in the conductor layers (applicable to conductors with more than 1 layer) and hence their resistance at every point in time; and calculating the real loss (mostly converted to heat) in the cable via  $I^2R$ .

Most single phase HTS cables consist of one to several layers of conductor and one to several layers of shield, essentially making it a coaxial cable. In order to find the values



of the self and mutual inductances of each layer of that cable, the following equations have been used [109]:

$$L_i = \frac{\mu_0 \pi r_i^2}{l_p^2} + \frac{\mu_0 \ln(D/r_i)}{2\pi} \quad (5.2)$$

$$M_{i,j} = M_{j,i} = \alpha_i \alpha_j \frac{\mu_0 \pi r_i^2}{l_{pi} l_{pj}} + \frac{\mu_0 \ln(D/r_i)}{2\pi} \quad (5.3)$$

where  $L_i$ ,  $r_i$  and  $l_i$  are the self-inductance, outer radius and twist pitch of the  $i$ -th layer respectively,  $M_{i,j}$  – mutual inductance between the  $i$ -th and  $j$ -th layer,  $D$  – the distance between the  $i$ -th layer and the centre of the return path (the shield layer which confines the magnetic field [11]),  $\alpha = -1, 1$  – an indicator of the direction of twist pitch of the corresponding layer. Derivations of these equations can be found in [109].

For the general case of a cable with  $n$  conducting and  $m$  shield layers, Kirchoff's Law is represented in matrix form in Equation 5.4 [35, 109]:

$$\begin{bmatrix} Z_{c-1} & \dots & j\omega M_{c-1,c-k} & j\omega M_{c-1,s-1} & \dots & j\omega M_{c-1,s-m} \\ \vdots & \ddots & \vdots & \vdots & \ddots & \vdots \\ j\omega M_{c-k,c-1} & \dots & Z_{c-k} & j\omega M_{c-k,s-1} & \dots & j\omega M_{c-k,s-m} \\ j\omega M_{s-1,c-1} & \dots & j\omega M_{s-1,c-k} & Z_{s-1} & \dots & j\omega M_{s-1,s-m} \\ \vdots & \ddots & \vdots & \vdots & \ddots & \vdots \\ j\omega M_{s-m,c-1} & \dots & j\omega M_{s-m,c-k} & j\omega M_{s-m,s-1} & \dots & L_{s-m} \\ 1 & \dots & 1 & 0 & \dots & 0 \\ 0 & \dots & 0 & 1 & \dots & 1 \end{bmatrix} \cdot \begin{bmatrix} I_{c-1} \\ \dots \\ I_{c-k} \\ I_{s-1} \\ \dots \\ I_{s-m} \end{bmatrix} = \begin{bmatrix} V_{dp} \\ \dots \\ V_{dp} \\ 0 \\ \dots \\ 0 \\ I_t \\ -I_t \end{bmatrix} \quad (5.4)$$

$$Z_{c-k} = R_{c-k} + j\omega L_{c-k} \quad (5.5a)$$

$$Z_{s-m} = R_{s-m} + j\omega L_{s-m} \quad (5.5b)$$

where  $R_{c-k}$ ,  $L_{c-k}$  are the per metre resistance and self-inductance of the  $n$ -th conductor;  $R_{s-m}$ ,  $L_{s-m}$  are the per metre resistance and self-inductance of the shield,  $M_{c-k,s-m}$  is the per metre mutual inductance between two layers (shield or conductor) and  $V_{dp}$  is the per metre voltage drop across the cable.

The first  $k$  rows represent Kirchoff's law for the conductor layers, where the voltage drop is  $V_{dp}$ . The next  $m$  rows show that there is no voltage drop across the shield. The last two rows force the sum of the currents in the conducting layer to be equal to the total transport current at a given time, and the sum of the currents in the shield layer to have an equal magnitude but opposite direction to the current in the conducting layers

at the same time:

$$I_{c-1} + I_{c-2} + \dots + I_{c-k} = I_t \quad (5.6a)$$

$$I_{s-1} + I_{s-2} + \dots + I_{s-m} = -I_t \quad (5.6b)$$

In these calculations,  $I_t$  can easily be substituted with any function describing periodic AC current, e.g. current magnitude multiplied by a sine function. This representation is according to Figure 5.13, where the conductor resistance is composed by the HTS and silver resistances connected in parallel:

$$R_{c-k} = \frac{1}{(1/R_{HTS} + 1/R_{Ag})} \quad (5.7)$$

and similarly for the shield resistance.  $R_{Ag}$  can be calculated from the real cross-sectional area of the silver material — not from the homogenized model. The skin effect penetration depth  $\delta = 1/\sqrt{\pi f \mu \sigma}$ , where  $\sigma = 3.7 \times 10^8$  S is the conductivity of silver at 77 K (from Table 5.3) and  $f = 50$  Hz is the power frequency, is equal to 3.69 mm. This is larger than the width of the tape (3.1 mm). Therefore, it may be assumed the current in the silver material is uniformly distributed.

The resistance of the superconducting material of each layer is expressed similarly to Equation 4.22 as:

$$R_{HTS} = \frac{E_0}{I_c} \left( \frac{I_{HTS}}{I_c} \right)^{(n-1)} \quad (5.8)$$

where  $R_{HTS}$  is the per metre resistance of the superconducting material,  $E_0$  is the critical current criterion in V/m,  $I_{HTS}$  is the magnitude of the transport current passing through the superconducting material of the given layer at a given time (A) and  $I_c$  is the critical current of the layer (A).

The calculation of current distribution between each conductor layer is achieved by solving Equation 5.4 and its supportive equations at every timestep. This is not necessary when dealing with a single-layer cable. However, it is always needed to be able to calculate the current sharing between the silver matrix material and the superconducting material within each conductor layer. This is unavoidable when considering currents above critical, where the matrix starts to bear significant amounts of current.

A current divider equation for a conducting layer in line with Figure 5.13:

$$I_{HTS} = \frac{I_{c-k} R_{Ag}}{R_{HTS} + R_{Ag}} \quad (5.9)$$

$$I_{HTS} + I_{Ag} = I_{c-k} \quad (5.10)$$

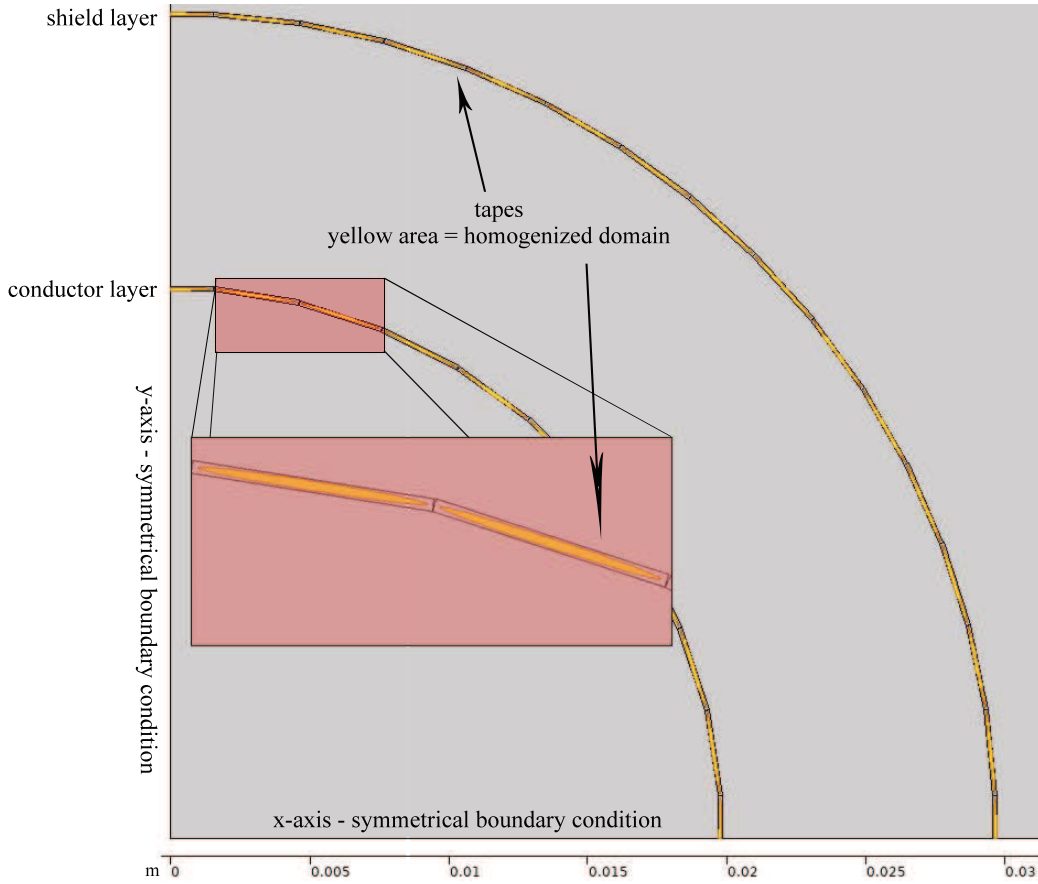


Figure 5.14: The symmetry arrangement of the COMSOL model.

Substituting for  $R_{HTS}$  from Equation 5.8 into Equation 5.9 and simplifying yields:

$$E_0 I_{HTS}^n + R_{Ag} I_c^n I_{HTS} - I_{c-k} R_{Ag} I_c^n = 0 \quad (5.11)$$

The above polynomial is of a very high order, and therefore can only be solved numerically. In this work, a Newton iteration method for MATLAB [110] is used to solve it for  $I_{HTS}$ .

The instantaneous loss can be calculated at every timestep over one cycle via  $I_{c-k}^2 R_c$  and then integrated as discrete data using a MATLAB function to give the loss per cycle. Alternatively, it can also be calculated via  $I_{HTS}^2 R_{HTS} + I_{Ag}^2 R_{Ag}$ .

### 5.3.2 Verification of the homogenization technique for a single layer HTS cable subjected to currents above the critical current

The Bi-2223 tape used here for the purposes of modelling of the sample cable is one fully characterized by Choi *et al* [68] (Figure 5.3). In the present study, these tapes are arranged in one conductor layer, the losses of which are the main point of interest, and one shielding layer. This means straight tapes can be used. The dimensions of the cable are shown in Table 5.5 and the configuration is similar to the one in Figure

# of conductor layers	1
# of shield layers	1
Conductor inner radius	19.695 mm
Conductor outer radius	19.865 mm
Shield inner radius	29.576 mm
Shield outer radius	29.746 mm
Conductor pitch length	$\infty$
Shield pitch length	$\infty$
# tapes in conductor	40
# tapes in shield	60
AC frequency	50 Hz

Table 5.5: Specification of the sample cable construction.

5.11, albeit with more tapes and a shield layer. The design of this cable only serves the investigation of its sample electromagnetic properties, and gives little consideration to insulation, stabilization, protection, design optimisation, or any specific device. The COMSOL simulations take advantage of rotational symmetry to model one quarter of the cable as in Figure 5.14. The MATLAB code follows the equations described in the previous subsection.

Two cases are considered. The first one models the single layer cable with the homogenization technique with a constant critical current; together with the equivalent circuit model. The second one takes into account the critical current dependence of the magnetic field and compares the homogenized tape with a tape with multiple separate filaments (Section 4.3.2). The purpose of this is to investigate whether, at currents well above critical, any effects arising from having a smaller cross-sectional area of the silver material in the homogenized model are neutralized by the lower critical current density within the homogeneous superconducting domain.

The results of the simulations in COMSOL and calculation in MATLAB are compared graphically in Figure 5.15. The demonstrated agreement between the homogenized model (orange) and the reference multifilamentary model (red) can be seen throughout the entire simulated range. The behaviour of the multifilamentary model and the homogenized model at currents below critical current was verified in Section 4.3.2 and Section 5.2, respectively. When comparing the COMSOL model with the equivalent circuit built in MATLAB (green), an agreement is observed at currents close to critical current and at currents much higher than the critical current.

The difference at  $I_t/I_c = 1$  in Figure 5.15 may be attributed to the difference in nature of the macroscopic (equivalent circuit, total current is important) MATLAB model and microscopic (electromagnetic fields, current density distribution is important) COMSOL

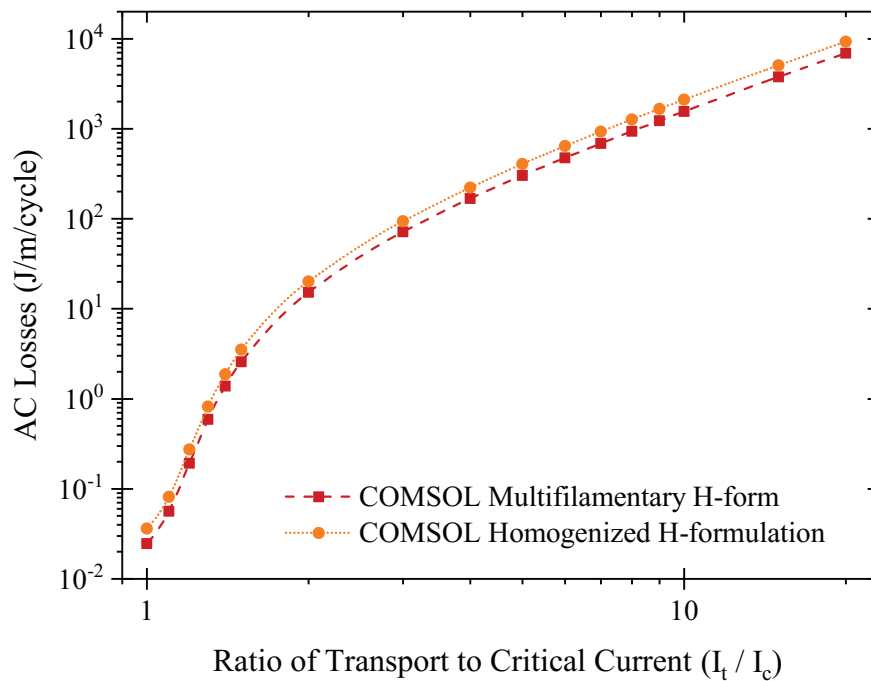


Figure 5.15: Simulation results of the homogenized model and the calculation of the analytical model with constant critical current.

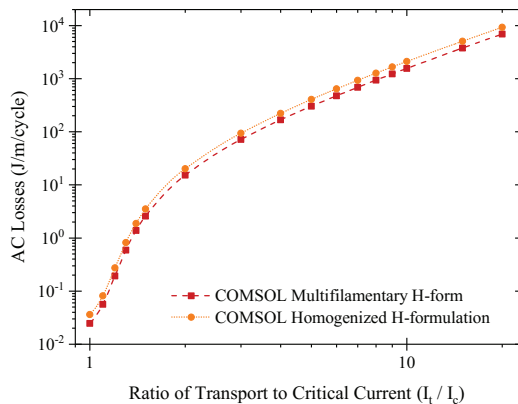


Figure 5.16: Simulation results of the numerical models with interpolated magnetic field dependent critical current.

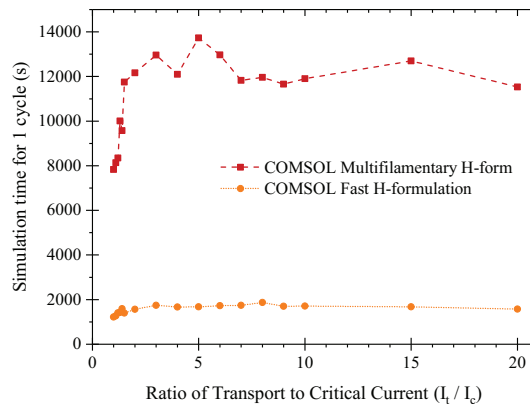


Figure 5.17: Simulation time of the homogenization and reference multifilamentary COMSOL model with field-dependent critical current.

model. Therefore, the MATLAB model does not take into account current distribution.

When comparing the multifilamentary and homogenized models that are with a magnetic field dependent critical current (Figure 5.16), a near perfect agreement can be seen.

In Figure 5.17 the simulation times of the two COMSOL models are compared, considering the times presented are for 1 cycle. Improvement in computational speed is 5 to 7 times.

## 5.4 Summary

A homogenization method was revisited in terms of its potential use for prediction of AC losses. It was verified via simulating a number of tapes in single or multiple tape configurations and with or without an external magnetic field, and comparing them with existing experiments. It was shown the method decreases the size of the problem considerably and displays a close fit with losses measured in literature.

To establish the quantitative accuracy and suitability of these models at a large scale and for transient analysis, more experimental data about cables and multi-tape conductors must appear in the literature. Such data must be accompanied with sufficiently detailed information about the tape properties and properties of any surrounding material.

### Contributions

- Reintroducing a domain homogenization method for the estimation of AC power loss of multifilamentary tapes with fully-coupled filaments, as well as cables built with multifilamentary tapes.
- The majority of this chapter was published in the form of a full length research article in *Physica C: Superconductivity and its Applications* under the title "Revisiting the homogenized domain model for fast simulation of AC transport power losses in first generation high temperature superconducting tapes and cables" [104].



## Chapter 6

# Estimation of power loss in twisted multi-layer Bi-2223 cables via 2D modelling

The work in this Chapter was presented in poster form on the *14th European Conference on Applied Superconductivity*, 1<sup>st</sup>-5<sup>th</sup> September 2019, Glasgow, and was published in the conference proceedings at IOP Publishing [111]. This chapter explores a technique for simulating first generation tapes and power cables with common twist angles that follows from the assumption the axial field can be neglected. Then the methodology is verified against several 3D models and measurements from literature taken from a real power cable.

### 6.1 Method for estimation of the power loss

#### 6.1.1 Method description

The proposed model in this chapter seeks, based on the multifilamentary region model from Chapter 5, to provide an easy-to-build and fast-to-simulate tool to estimate effects that are otherwise heavily dependent on 3D geometries and variables. The computational and time cost of finite element modelling can then be greatly reduced, enabling FEM to be easily used for AC loss calculations, and may be the base for further multi-physics studies.

A critical limitation of the method is that it may not predict the current sharing between the individual superconducting layers. When the current sharing is known and imposed on the 2D model, whether by experiment, by induction matching of the layers [109] or by coupling with an external MATLAB evaluation of the current sharing, this limitation is minimized. A remaining consideration is that in currents above critical the resistivity may, in theory, reach values comparable with the inductivity and thus influence the



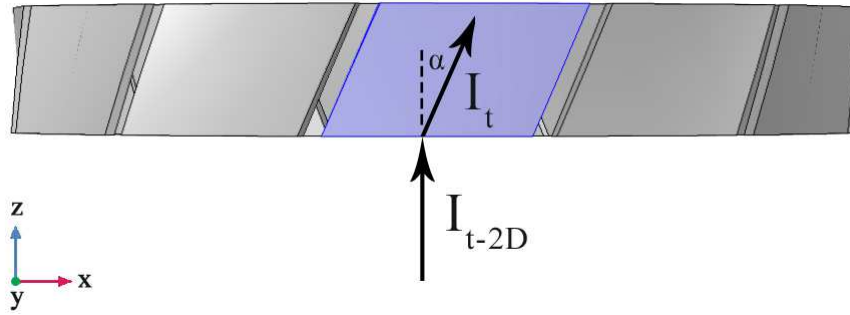


Figure 6.1: A top-down view of a small section of the 3D geometry of a power cable, the piece shaded in blue is a twisted tape. This is an illustration of the trigonometric relationship between  $I_t$  and  $I_{t-2D}$ .

current sharing. For this Chapter, it is assumed the current is equally shared between all layers.

This is not a substitute for a proper 3D study, but is rather an opportunity to achieve a time-efficient FEM simulation via an approximation.

### Mathematics

The essence of the proposed model is applying a current through a 2D cross-section, such that the magnitude of this applied current is equal to the total current flowing through the cross-section, and not the total current of the tape (Figure 6.1).

If the peak transport current flowing in a twisted tape is  $I_t$  and the twist angle is  $\alpha$ , then the peak applied current in the 2D cross-section is:

$$I_{t-2D} = \frac{I_t}{\cos \alpha} \quad (6.1)$$

Furthermore, the critical current density at zero field at any point of the 2D cross-section remains at the value prescribed by examining a straight tape via  $J_{c0} = I_c/S_{HTS}$  ( $I_c$  – critical current at self field,  $S_{HTS}$  – area of the tape taken from a perpendicular cross-section).

Additionally, each tape of a particular layer in the 2D model has its width  $w_t$  modified by the cosine of the twist angle  $\alpha$  of that layer. Displayed in Figure 6.2, similarly to Equation 6.1:

$$w_{t-2D} = \frac{w_t}{\cos \alpha} \quad (6.2)$$

### Constructing the 2D model

A single cross-section in a 2D model cannot represent the various positions a tape from one layer can have in relation with a tape from another layer. Therefore, it would not be able to truly estimate the electromagnetic relationship between every twisted layer. However, in a sufficiently long cable, it may be assumed that every possible cross-section

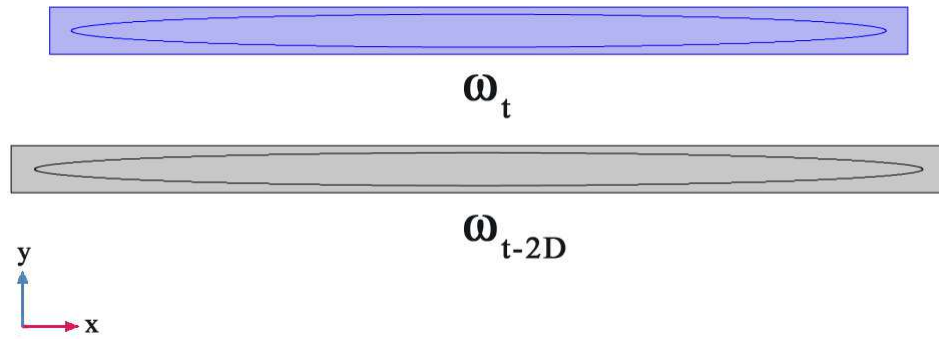


Figure 6.2: Visual description of the modification a tape's width must undergo for the method to work — from  $\omega_t$  (above – in blue) to  $\omega_{t-2D}$  (below).

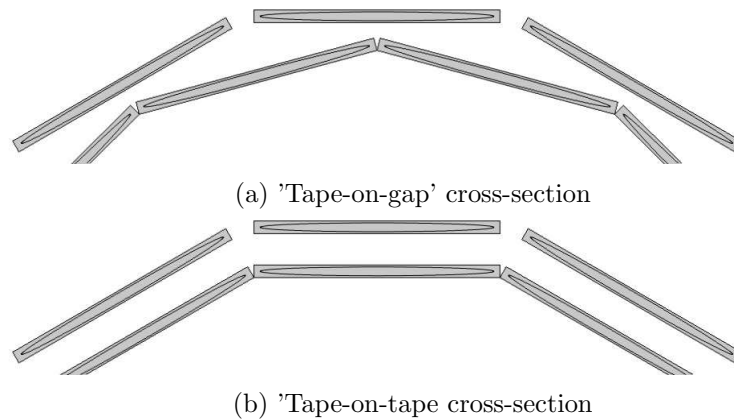


Figure 6.3: Illustration of the two types of cross-section used for approximating 3D losses.

is repeated an equal number of times. From that, it is proposed that the total AC loss in the cable is equal to the average value of the AC loss calculated by the 2D models using the "lower and upper extremes". It is already known that the AC loss in a practical cable must fall between the losses in the two extremes [112].

In an *alternating* cross-section, otherwise known as "tape-on-gap", each cable layer is rotated such that the center of a tape from any given layer will be above the gap between the tapes of the layers above and below (Figure 6.3a). This type of cross-section was observed to achieve the lowest losses and lowest internal magnetic fields in 2D of all other possible cross-sections, and as such is considered the "lower extreme".

Similarly, in the *aligned* cross-section, otherwise known as "tape-on-tape", the centres of the tapes in all layers are stacked on top of each other (Figure 6.3b). This type of cross-section was observed to achieve the highest losses and highest internal magnetic fields in 2D of all other possible cross-sections, and as such is considered the "upper extreme".

The need for these two cross-sections is most easily understood using two-layer cables, but the principle is applicable to cables with more than two layers.

### 6.1.2 Handling the critical current density's dependence of the magnetic field in twisted tapes in 2D and 3D

When a piece of tape is twisted, its axes — along the tape, perpendicular to the wide face and to the short face — no longer correspond to the axes of the global coordinate system. Then, the direction of the "magnetic field perpendicular to the tape" vector may no longer match any of the unit vectors of the coordinate system. This can introduce complications when the anisotropic dependence of the critical current density on the magnetic field is calculated in models where the twist of the tape with respect to the coordinate system is not taken into account.

In standard Cartesian 2D, the correction is fairly easy. There are two magnetic field components,  $H_x$  and  $H_y$ . If the magnetic field dependence on the field perpendicular to the tape's wide face is considered, the contribution from the  $H_y$  component is maximum and from  $H_x$  is zero when the wide face of the tape is lying on the x-axis. Then, the contribution from the  $H_y$  component is zero and from  $H_x$  is maximum when the wide face of the tape is lying on the y-axis — a  $\pm 90$ -degree turn. Similarly for the dependence on the field parallel to the tape's wide face, the maximum contribution from the  $H_x$  component is maximum and from  $H_y$  is zero when the wide face of the tape is lying on the x-axis, and the contribution from the  $H_y$  component is maximum and from  $H_x$  is zero when the wide face of the tape is lying on the y-axis.

This can be seen in Figure 6.4. It is achieved mathematically via the method widely known as rotation of base vectors — representing an arbitrary vector expressed in terms of the base vectors  $\vec{x}_0, \vec{y}_0$  of the global coordinate system into the terms of the base vectors  $\vec{x}_n, \vec{y}_n$  of the local system of each tape. The representation is made via the following trigonometric formulas:

$$H_{m-x} = H_x \cos \phi_r - H_y \sin \phi_r \quad (6.3)$$

$$H_{m-y} = H_x \sin \phi_r + H_y \cos \phi_r \quad (6.4)$$

$$\phi_r = \tan^{-1} \left( \frac{x}{y} \right) \quad (6.5)$$

where  $H_{m-x}$  is the component of the magnetic field perpendicular to the wide face of the tape and  $H_{m-y}$  — the component parallel to the wide face of the tape.  $\phi_r$  is the angle of rotation of the tape (clockwise) — conditional formulas must be added to find the quadrant of the point in order to determine the absolute rotation.  $x$  and  $y$  are the Cartesian coordinates of point at which the effective magnetic field is calculated, assuming that the cable is centered on  $x = 0, y = 0$ .

In 3D, a decision must be made what effect the longitudinal magnetic field, in this case  $H_z$ , would have on the critical current density. It has been shown that the longitudinal field  $H_z$  has a slightly smaller contribution to the critical current dependence than the

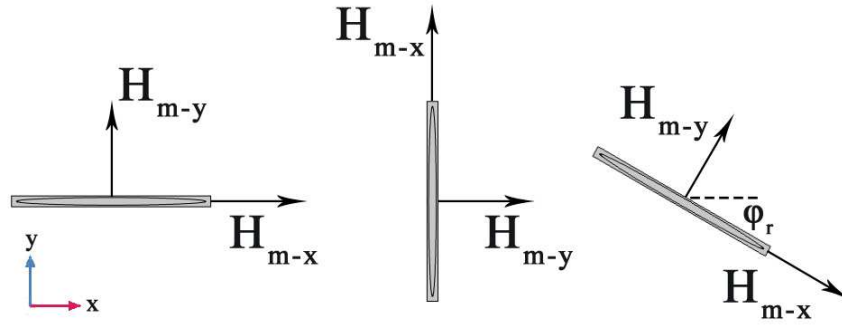


Figure 6.4: Illustration of the relationship between  $H_{m-x}$ ,  $H_{m-y}$  and the axes of the coordinate system in 2D.

field parallel to the wide face of the tape [113]. For simplicity, it has been assumed it bears the same contribution. In such case,  $H_z$  is added as-is to the calculation of the total magnitude of  $H_{m-x}$ .

This is represented mathematically via the following trigonometric formula:

$$H_{m-x} = \sqrt{(H_x \cos \phi_r - H_y \sin \phi_r)^2 + H_z^2} \quad (6.6)$$

$$H_{m-y} = H_x \sin \phi_r + H_y \cos \phi_r \quad (6.7)$$

Inspecting Equations 6.3 and 6.6, it is immediately seen that the addition of the longitudinal field in such a manner should lead to results that cannot be similar. It may be possible to estimate the value of  $H_z$  by knowing the twist angle. However, after review of the evidence collected in the next section, it can be seen that the average values of  $H_{m-x}$  and  $H_{m-y}$  in both 2D and 3D (volumetric) are similar. Since the value of the current used in the 2D model is based on the cross-section inflow, which is larger than the actual transport current, the magnitude of the longitudinal field can be said to "redistribute" into the remaining two field components. However, due to the complex interactions in 3D, this is not always true when the pitch length approaches 0.1 m. This is a source of error, but it is not significant.

### 6.1.3 Notes on layer twist

It has already been mentioned that the twisting of a layer is necessary to ensure the current flowing through it is evenly distributed with all other layers of the same phase. Equation 5.2 shows how to calculate the self-inductance of a given conductor layer, and Equation 5.3 shows how to calculate the mutual inductance between that layer and another layer. In both equations, the twist pitch of the layer is a variable. If Kirchoff's law for each conducting layer is written in a system of equations (such as Equation 5.4), and the currents flowing in each layer are declared equal, the only unknown is the twist pitch of each layer. As there are  $n$  layers with a total of  $n$  twist pitches in  $n$  number of equations, the system can be solved for the twist pitch at equal current distribution.

	# of conductor layers	2
	# of shield layers	0
	# tapes in layer 1	12
Common values	# tapes in layer 2	12
for all cables	Extrusion length	35 mm
	AC frequency	50 Hz
	Total $I_c$	1872 A
	Tape	Choi [68]
	Pitch length, layer 1	300 mm (+)
Cable 1	Pitch length, layer 2	300 mm (-)
	Layer 1 inner radius	5.8289 mm
	Layer 2 inner radius	6.3389 mm
	Pitch length, layer 1	300 mm (+)
Cable 2	Pitch length, layer 2	100 mm (-)
	Layer 1 inner radius	5.8289 mm
	Layer 2 inner radius	6.3389 mm
	Pitch length, layer 1	100 mm (+)
Cable 3	Pitch length, layer 2	100 mm (-)
	Layer 1 inner radius	6.2224 mm
	Layer 2 inner radius	6.8174 mm

Table 6.1: Specifications of the 3D cables used in verifying the 2D approximation method. The (+) and (-) signify twist direction.

The value of twist pitch in each layer of a cable would vary widely depending on the number of layers and their radii. In terms of practical twist pitches, the shortest can be as little as 115 mm [114] and the the longest can be as long as 795 mm [115], as well as anything in between.

## 6.2 Method verification

The proposed method is tested in three sample 2-layer cables, modelled in 2D and 3D, and one real 4-layer cable, modelled in 2D and compared with the losses from literature.

The homogenization model from Chapter 5 is applied for all models, both 3D and 2D.

### 6.2.1 Construction of sample 3D cables

Three cables with two layers each are proposed, their details are shown in Table 6.1. The tape used in these cables is the Choi tape [68], described in Table 5.3. Each of these three cables has been simulated in 3D by taking a length of 3.5 cm. A control sample of longer lengths did not produce different results.

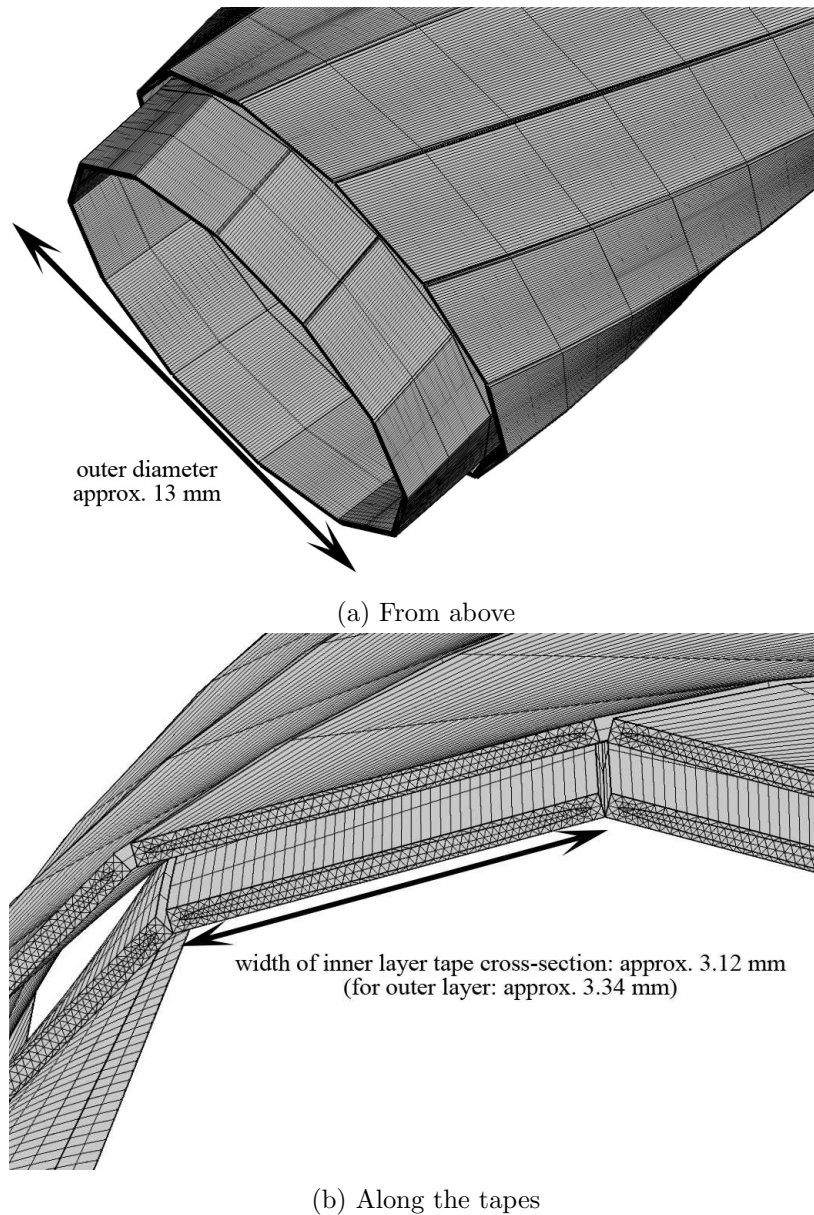


Figure 6.5: Illustration of the twist and meshing of the two layers in Cable 2.

Firstly, the 2D geometry is built by drawing each layer separately using its radius and twist angle, and putting it together with the other layers, according to Equation 6.2. The tape geometry is left rectangular, thus no curving is applied within the cross-section. This does not matter when the corresponding 2D model is also built the same way.

To build the geometry for the 3D models, each already-made 2D layer is sweep-extruded along a parametric curve, described mathematically by the pitch length and radius of each layer. The 3D model simulations are run on the High Powered Computing Cluster IRIDIS 4, located at the University of Southampton. They are simulated using an  $H$ -formulation as described in Chapter 4.2.1, adapted for 3D by adding a third dimension variable, which is also described in detail in [94]. The transport current is forced to be equally spread between the layers via pointwise constraint integration, applied on the

	# of conductor layers	4
	# of shield layers	2
	# tapes per conductor layer	13
Cable details	# tapes per shield layer	26/27
[114]	Conductor outer radius	10 mm
	Shield outer radius	18.5 mm
	Conductor pitch lengths, mm	130(+), 305(+), 400(-), 115(-)
	Shield pitch lengths, mm	350(-), 530(+)
	Total $I_c$	$\sim 2700$ A
	Tape dimensions	0.24 mm $\times$ 3.8 mm
	Tape $I_c$ and $n$	52 A, 10.5*

Table 6.2: Specification of the real 2D cable used in verifying the 2D approximation method.

\*- the value for  $n$  is extracted from the E-V characteristic in [114].

contact surface of each layer; no restrictions are enforced on the individual tapes.

The AC loss is taken twice, firstly from the volume of the entire model, and secondly from a small central section of the volume that should not experience any end effects:

$$Q_{tot} = 2 \int_{0.5/f}^{1/f} \iiint_{V_t} Q dt \quad (6.8)$$

where  $V_t$  is the volume of interest,  $Q = JE$  is the AC loss.

Swept meshing is used in all domains as a compromise between a sufficiently fine mesh within the superconducting domain and a reasonable amount of degrees of freedom (Figure 6.5). However, with the twisting of each layer being different, the two swept meshes would not be able to join. Then, adding buffer domain(s) where the mesh is free tetrahedral becomes necessary.

It was observed that adding more sections of swept mesh would calculate AC loss values that display a trend of plateauing after a certain density is reached. This is expected since the more sections the swept mesh has, the closer the mesh is to representing the real twisting of the tapes.

To be able to achieve convergence, the Jacobian was set to be updated once per timestep, up from the default "minimal" setting. This improves the Newton Method's ability to calculate in the presence of very large non-linearities, but it is more computationally expensive.

### 6.2.2 Construction of a 2D model based on a real cable

A cable, installed and tested in laboratory environment [114] has been selected to be modelled in 2D due to the existence of sufficient detail of its specifications and AC loss

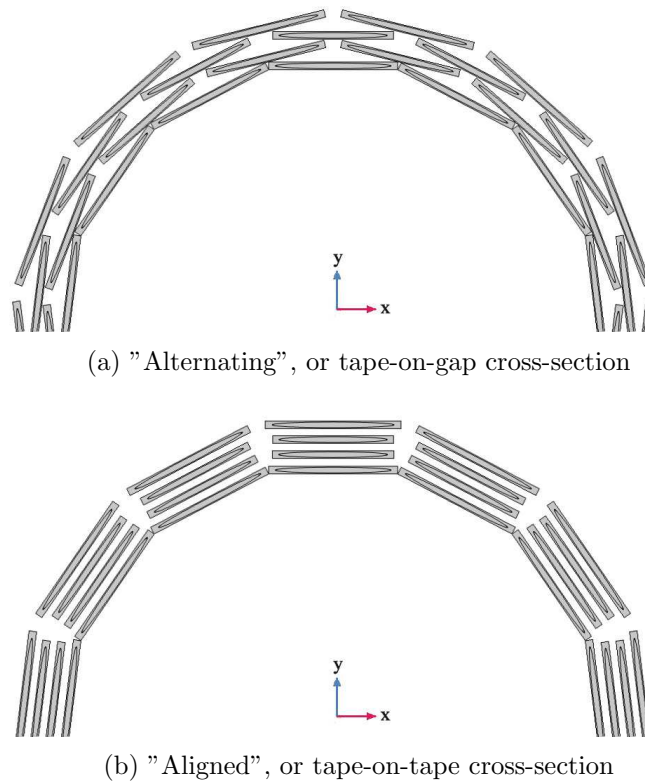


Figure 6.6: The two cross-section types as applied to the 2D cable from [114].

data. It is a 66 kV, 100-metre long cable in a 3-cores-in-1-cryostat configuration. The details relevant to the AC loss simulations are provided in Table 6.2. (+) and (-) signify the direction of the twist of each layer, which does not have any effect on the proposed method, provided that: 1) the design of the cable is such that equal current flows in each layer due to balanced inductance values, or 2) the values of the currents flowing in each layer of the model are the same as their corresponding values in the real cable. An  $H$ -formulation is used, which has been described in detail in previous chapters.

The 2D geometry is built by drawing each layer separately using its radius and twist angle, and putting it together with the other layers. Each tape of a particular layer has its width  $w_t$  modified by the cosine of the twist angle  $\alpha$  of that layer, as in Equation 6.2. As in the 3D case, the tape geometry is left rectangular, thus no curving is applied within the cross-section. This is not anticipated to be a problem due to the very small difference between the geometry of a curved and non-curved tape.

Due to the information about layer radial positioning being limited to the inner and outer radii of the conductor and shield, the layers were placed evenly within these radii.

The 2D model of the cable by [114] can benefit from symmetry along the  $y$ -axis or  $x$ -axis. Only half the tapes are simulated, using an appropriate symmetry boundary condition — in this case for symmetry along the  $y$ -axis —  $H_y = 0$ . Then, the value of any calculated losses is doubled to compensate.



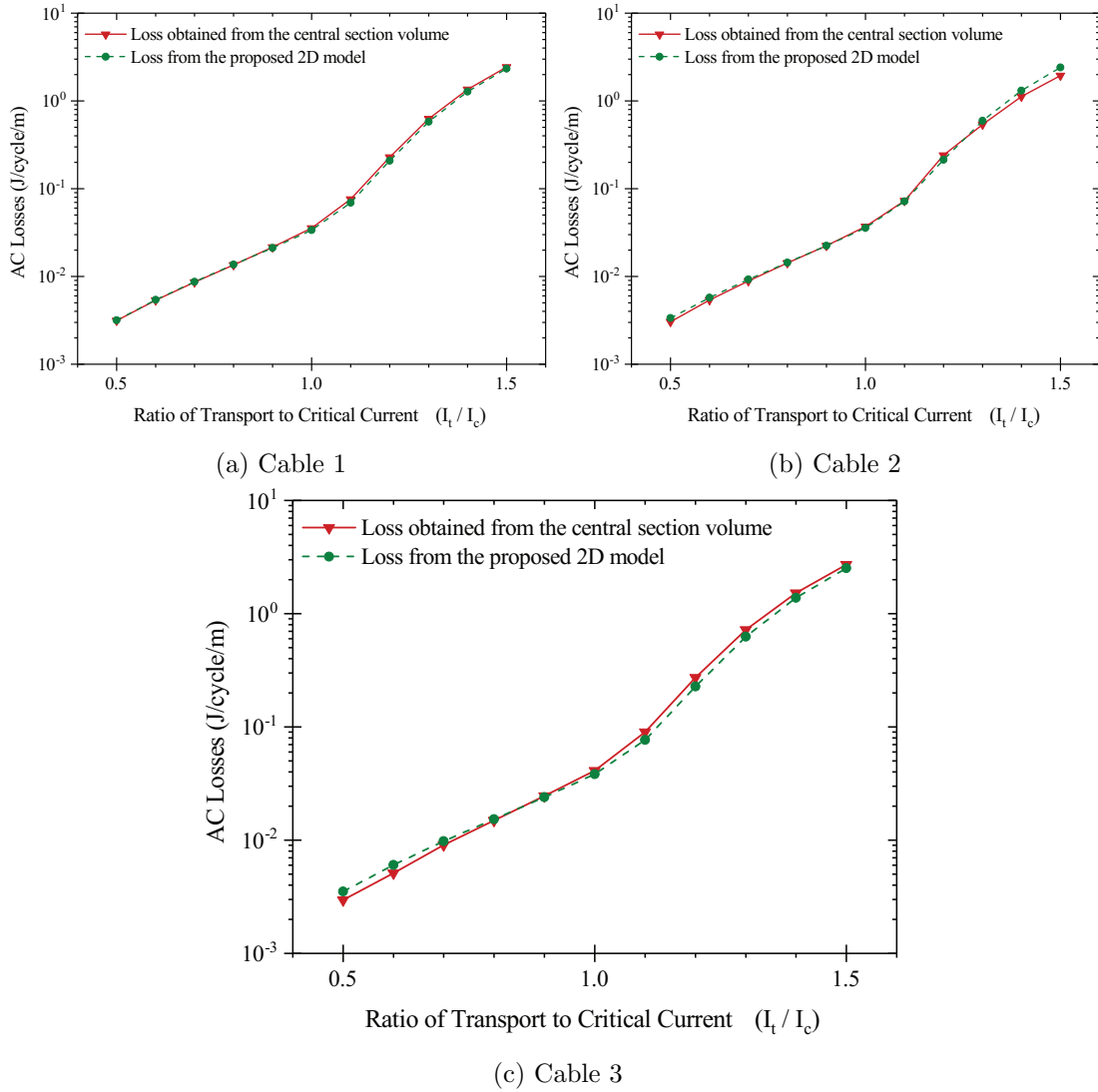


Figure 6.7: The simulated AC losses from the 3D models and the 2D models, compared by cable.

There is lack of information about the critical current dependence of the magnetic field and the proportion of silver to HTS material within a tape. Hence, it is assumed the tapes exhibit a field dependence and silver to HTS ratio common with other tapes from the beginning of the 21st century — the Amemiya [103] and Choi [68] tapes. Their dependencies are plotted in Figures 5.4, 5.8 and 5.10. The silver to HTS ratio has a limited effect at transport currents below critical, since the vast majority of the current flows inside the superconductor. At currents above critical the effect should be more prominent, but these are not simulated for this cable.

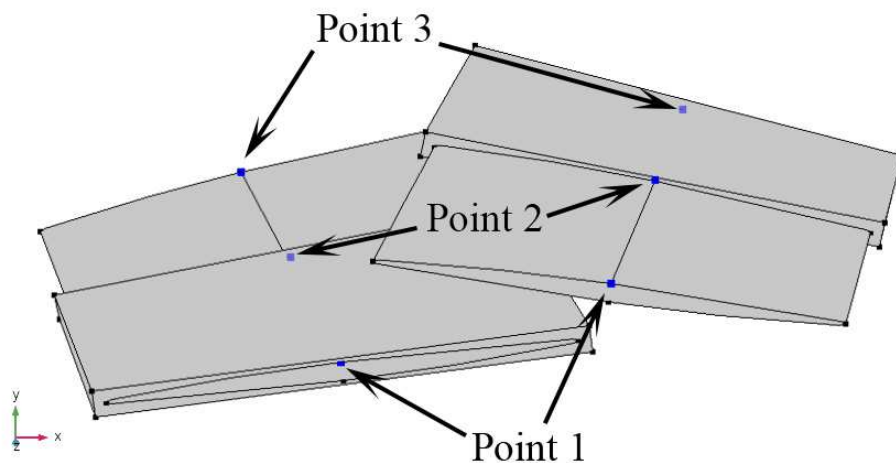


Figure 6.8: Displaying the location of the points in Figure 6.9.

### 6.2.3 Results analysis

#### Three two-layer cables, simulated in 3D and 2D

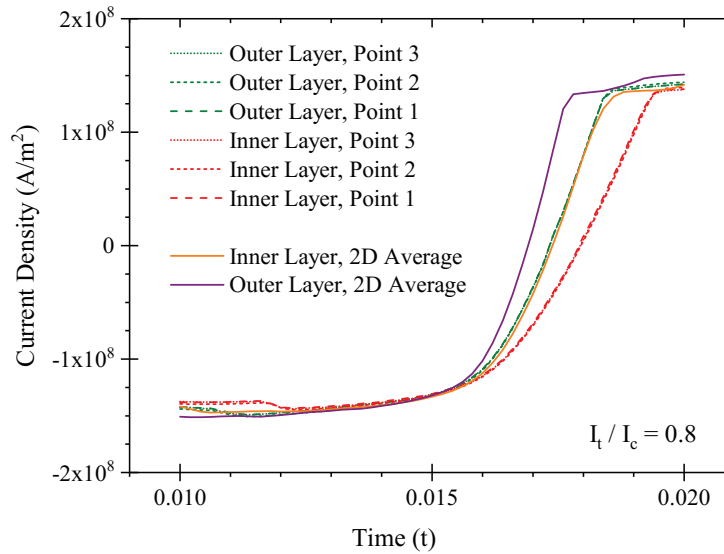
The three cables have been built and simulated as per the provisions of the previous sections. The results of the simulations are available in Figure 6.7.

The highest difference between the losses in the 2D and 3D (from the central volume) models in Cable 1 being 8%, in Cable 2 – 19%, and in Cable 3 – 20%. This can be seen in Figure 6.7.

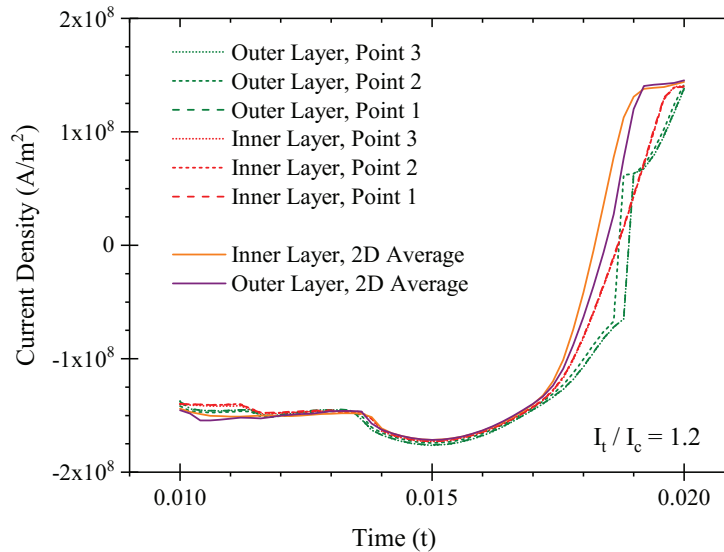
It was observed the shorter the pitch length of a layer, i.e. the sharper the twist, the denser the swept mesh has to be in order to capture the smoothness of the twist realistically. This is the most likely cause of the fact that Cable 3 (lowest pitch length) produces the worst match with the 2D model. Coincidentally, it was also observed that with increasing the density of the swept mesh, the 3D calculated loss values were approaching those calculated by the 2D model; finally plateauing at the values presented in Figure 6.7.

To confirm that the model does exhibit a symmetrical 3D cable, the following criteria are examined in post-processing: 1) consistency of current densities on points along a path, parallel to the length of the same tape; 2) symmetry of magnetic fields at the same points of every tape within a layer; 3) direction of the current density magnitudes inside each tape. Comparisons are presented here only for Cable 3, as it bears the lowest pitch length and therefore exhibits 3D effects more strongly.

Looking at the consistency of current density along the length of a tape (i.e. investigating continuity along a current flow line), it was noticed that unless the point was defined explicitly at the geometry building stage, it is difficult to ensure it lies on the same line. This is because in a swept mesh, the detail of the mesh, length-wise, is relatively coarse in order to achieve a trade-off with simulation time (Figure 6.5). This prevents



(a) Cable 3,  $I_t/I_c = 0.8$



(b) Cable 3,  $I_t/I_c = 1.2$ .

Figure 6.9: Current density at three points on the same position within the same tape with respect to the cross-section, but at different longitudinal positions. Both figures present the current at a point in the outer layer as well as in the inner layer. The discontinuity around  $t = 0.019$  s in (b) is discussed in the text.

examining the values of the current density along a given current flow line, as it simply isn't sufficiently well represented by the mesh. The mesh cannot be improved to a sufficiently high standard as it will be very expensive computationally. The values of current density on three points along the central section of two tapes are presented in Figure 6.9 for the negative half-cycle, where it is shown there is a strong consistency between them. Figure 6.9 also compares the current densities at the points from the 3D model with the value of the current density for the same point, in the corresponding 2D, averaged between the *tape-on-tape* and *tape-on-gap* methods. It can be seen that

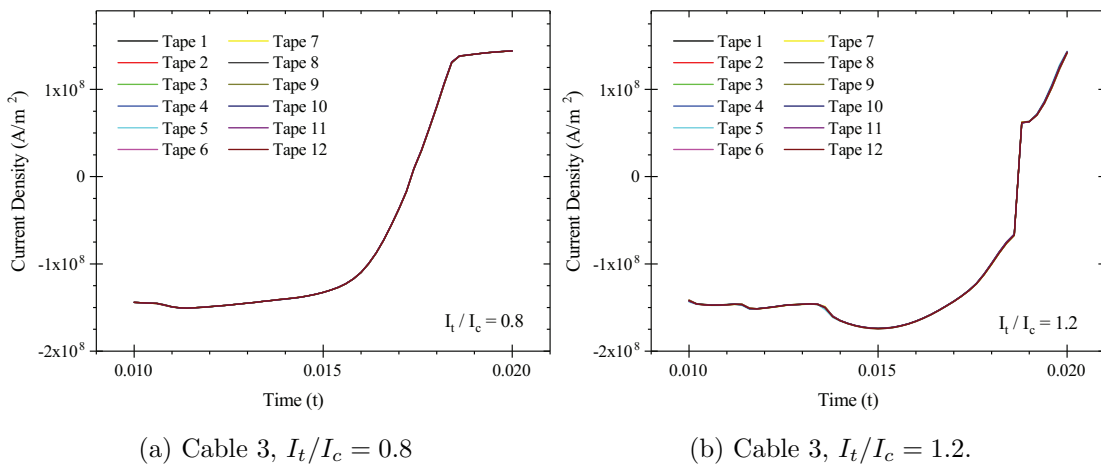


Figure 6.10: Current density at twelve points on the same position within the twelve tapes, with respect to the cross-section, and at the same longitudinal positions. Both figures present the current at a point in the outer layer only. The discontinuity around  $t = 0.019$  s in (b) is discussed in the text.

the current density in the 2D model reaches zero before the current density in the 3D model, which must be a local 3D effect, but the reason is unknown. However, there is an excellent match at the peak values of current density, and the "delay" between the 2D waveforms perfectly matches the "delay" between the 3D waveforms.

Similarly for the current densities on the same point of a tape, taken from each of the 12 tapes in a layer, a near perfect symmetry can be seen (Figure 6.10). For the cable at  $I_t/I_c = 1.2$  in both Figure 6.9b and Figure 6.10b, there is a sharp discontinuity, which is a result of taking the magnitude of the total current  $J_n = \sqrt{J_x^2 + J_y^2 + J_z^2}$  and plotting it as  $J_n x$  where  $x = \pm 1$  depending on whether  $J_z > 0$  or  $J_z < 0$ . There is no discontinuity in the individual current components  $J_x$ ,  $J_y$  or  $J_z$ ; there is also no discontinuity when  $J_n$  itself is plotted. Instead, this is attributable to a numerical effect arising from the mesh quality in combination with the higher transport current that makes  $J_x$  or  $J_y$  temporarily larger than the primary current carrier  $J_z$ .

The average magnetic field density of Cable 3 for three values of the transport current can be seen in Figure 6.11. As expected, the magnetic fields from each model are very similar for the same transport current, and the average magnetic field in the 'tape-on-tape' cross-section model is the highest.

Lastly, the direction of the current is observed in Figure 6.12. It can be seen to follow the tape as expected, and that behaviour is the same throughout all tapes.

### A real four-layer cable simulated in 2D

Following the provisions in the previous sections of this chapter, the cable from [114] was simulated for 8 values of the peak transport current. These values were extracted from the AC losses figure from the relevant publication using a graph data extractor. Each phase in [114] has a different critical current. Therefore, they are not identical and each phase must be simulated with separate critical current density. Then, the resulting

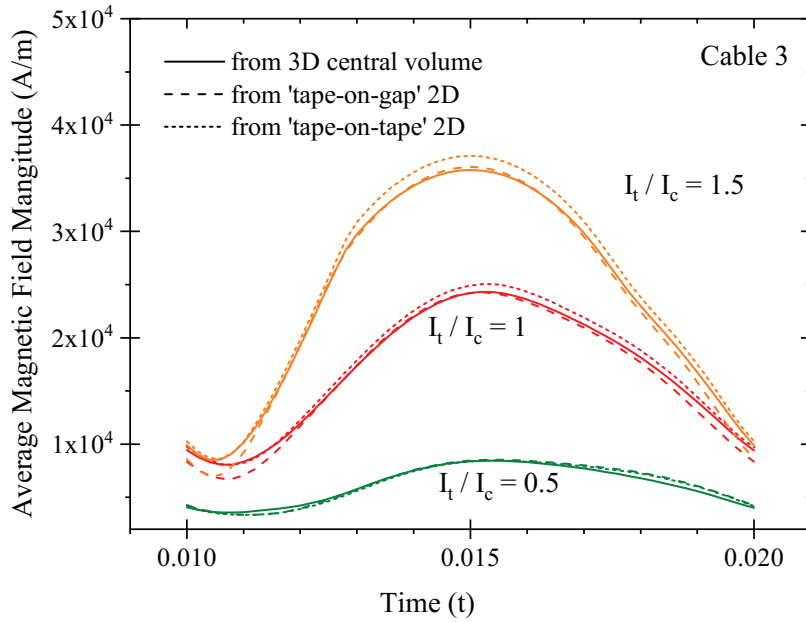


Figure 6.11: The average value of the magnetic field magnitude within the HTS material of all tapes of Cable 3, for three values of the transport current. The frequency is 50 Hz, thus the period is 0.02 s. The graph starts at the half-period  $t = 0.01$  s; the observed difference of the average field magnitude between the data sets at that time can be explained by the fact that a residual magnetic field remains even when the transport current is equal to zero, and that a higher transport current means a higher average residual field.

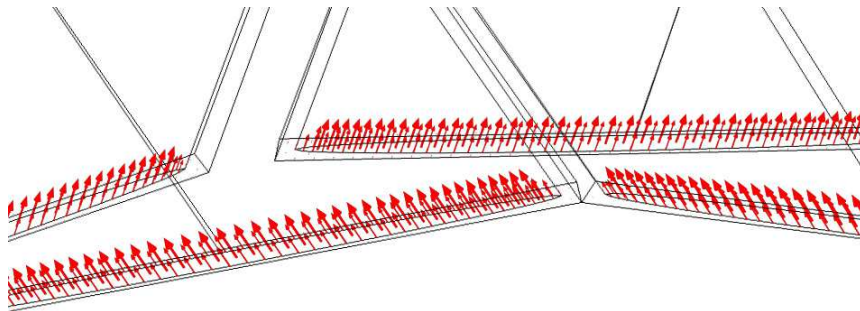


Figure 6.12: The direction of current flow in Cable 3 at peak transport current of 0.8 times the critical current. Each arrow represents the vector of current obtained by plotting the three current density components as each mesh node.

AC power losses from each phase can be summed together.

The results from this simulation are summarised in Figure 6.13. As expected, the 'tape-on-tape' cross-section simulation produces power loss with increasing current at a larger rate than the 'tape-on-gap' cross-section. This is because stacking current carriers (tapes – Figure 6.6b) above each other produces a stronger local magnetic field, due to superposition. Figure 6.6b would also remind of a coil configuration, where such stacking is used deliberately for increasing the magnetic field intensity.

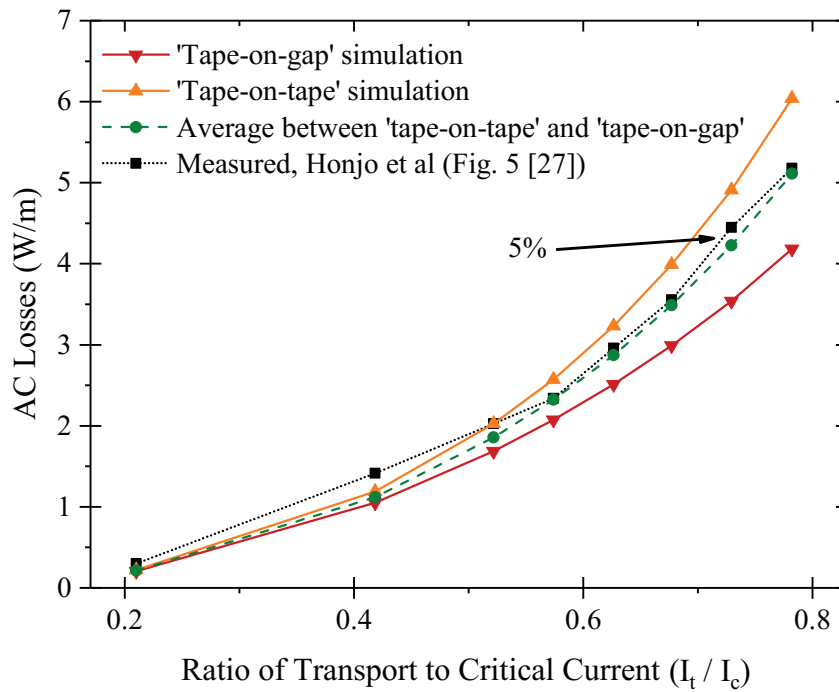


Figure 6.13: Simulated total AC losses in the 2D cable from [114], compared with measurements from literature.

Averaging the AC loss values of the 'tape-on-tape' and 'tape-on-gap' cross-section models produces a difference with the values measured in [114] of no more than 5% when approaching critical current. Below half the critical current, the overall simulation displays inaccuracy that can be attributed to the numerical model as a whole. The existing inaccuracy may be due to the fact the  $I_c$  dependency on the magnetic field was assumed, the lack of specific data about the exact spatial positioning of each layer, and the lack of information about the material make-up of the tape's cross-section.

There is very little to no effect on the above observations when the simulations use the critical current dependence on the magnetic field from either Amemiya or Choi.

### 6.3 Summary

A method for approximating the total AC power loss of first generation twisted-layer cables under transport current conditions in 2D has been presented.

It has been verified against 3D models of three sample 2-layer cables with different pitch lengths, with the results achieving a match with differences within the range of 5%–10%, and no more than 20%.

Models built with this method are easier and faster to construct and simulate than a corresponding 3D model, which can have significant implications when the level of detail of a FEM model is desirable but has previously been impractical to obtain.

Furthermore, the good match (within 5% at  $I_t/I_c > 0.5$ ) of the results for the real cable is promising. It may, however, be necessary to simulate the AC loss of several other real

cables before concluding the proposed method is valid. Such data, however, is scarce in literature.

These results show that the longitudinal magnetic field existing in a cable can be assumed to be negligible in many cases (as already stated in [15] and shown in [81]), since of importance to the tape's performance are the effective magnetic field values (Equations 6.3-6.7) rather than magnetic field components themselves. It would also be beneficial to observe how useful the averaged cross-sections model is when observing other effects within the cable, or attempting to simulate longitudinal and radial temperature rise.

### **Contributions**

- A method for approximating the losses of tapes wound over a circular former, taking into account the twist angle, is developed and verified.
- The introduction and verification of a technique for the estimation of AC power loss of multi-layer power cables with layers with varying twist pitches in a purely 2D cross-sectional model.
- Achieving in COMSOL a smooth and continuous split of the magnetic field into parallel and perpendicular components over the full rotation of a cross-section, in order to effectively take into account the anisotropy of the tape.
- Constructing and simulating the AC power loss in a single-phase two-layer power cable in 3D for a range of transport currents including above critical.
- The majority of this Chapter is published in the form of a conference paper at the IOP Conference Series under the title "2D finite element modelling of the AC transport power loss in multi-layer Bi-2223 cables" [111].

## Chapter 7

# Transient fault simulations using COMSOL

In this chapter, a finite element solution to the problem of HTS cable response to and recovery from a transient short circuit fault is discussed. The constructed model is split in three distinct stages:

1. Temperature profile – where the model of the cable is built and the steady state of the temperature within the cable during normal operation is found. This is achieved via a 1D coolant and a 2D-axisymmetric model;
2. Overcurrent response – using the steady state temperature profile as initial conditions, the electro-magneto-thermal solution due to the fault current is calculated. This is achieved primarily via a 2D cross section model;
3. Fault recovery – after the fault has been cleared, the cable system must return to normal temperature. This is again achieved via a 1D coolant and a 2D-axisymmetric model.

First, further modelling techniques that are required in this chapter are presented. Second, the background of the real cable to be modelled is laid out together with its most important properties. Third, as an original contribution, the cable model is built, simulated and results are reviewed.

The majority of this Chapter has been submitted for review in IEEE Transactions on Applied Superconductivity under the title "Efficient multiphysics finite element simulation of a transient fault in a first generation HTS power cable".



## 7.1 Further modelling theory

### 7.1.1 Modelling of the fault current waveform

In three phase systems, a short-circuit can occur between one or more phases and/or the ground. This leads to development of a short-circuit current, which may be extremely large compared to the normal operation current, depending on system properties. The largest short-circuit currents are developed during the three-phase fault [116] where, at the fault location, the three phases and the ground short all at once. When this fault is downstream from the superconducting cable, the cable will experience the fault current until it is cleared on its own or by a circuit breaker.

In power systems protection engineering where, due to the scale of the system, power equipment is treated as a black box, variables of interest such as 'initial peak current', 'RMS fault current' and 'fault level' are pinpointed [117]. In the numerical modelling of said power equipment, the full transient current waveform must be used. The way a three-phase fault develops may be described with a simplified RL circuit diagram, as seen in Figure 7.1 [118]. The voltage source  $V_s$  represents the power stations, with  $\phi$  indicating the phase delay ( $0, -\frac{2\pi}{3}, \frac{2\pi}{3}$ ).  $R_{grid}$  and  $L_{grid}$  are the lumped upstream resistance and inductance of the power grid,  $R_{HTS}$  and  $L_{HTS}$  are the resistance and inductance of the superconducting cable.  $R_{HTS}$  is practically equal to zero during normal operation and increases significantly with the onset of overcurrent — this is how superconducting fault current limiting is achieved. The load impedance during normal operation is represented via  $Z_{load}$ , which is immediately bypassed at the beginning of a short-circuit fault (switch  $S$  closing) [57].

If:

$$R = R_{grid} + R_{HTS} \quad (7.1)$$

$$L = L_{grid} + L_{HTS} \quad (7.2)$$

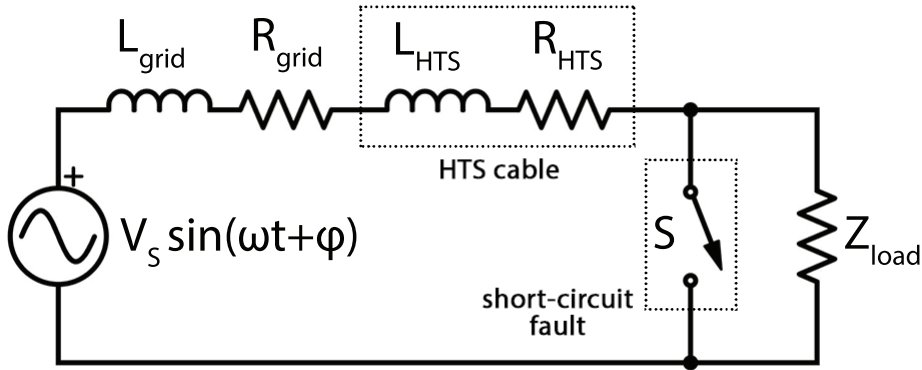


Figure 7.1: Circuit diagram of a power system under short circuit fault.

Then, the development of a short circuit fault follows Kirchoff's Law [118]:

$$V_s \sin(\omega t + \phi) = RI + L \frac{dI}{dt} \quad (7.3)$$

where  $I$  is the total current flowing in the circuit. Assuming that the current in each phase at fault start is negligibly small compared to the developed fault current, the initial conditions for Equation 7.3 are  $I(0) = 0$ ,  $dI/dt(0) = 0$ .

It can be inferred directly from the Equation above that the highest initial peak is achieved when the fault begins at the time when the voltage passes through zero.

Solving the ODE in Equation 7.3 at each time step provides the fault current waveform.  $R_{HTS}$  is dynamically updated at each time step to ensure the increasing superconductor resistance is captured and its effect observed. This equation can be solved numerically in COMSOL via the General Equation node under the General Form PDE module. Solving it numerically is unavoidable due to the high non-linearity of the superconducting resistivity (Private communication, Dr Wesley Tiago Batista de Sousa, Karlsruhe Institute of Technology, October 2019).

It can be seen, however, that Equation 7.3 has only the self-inductance of the line, but does not include any mutual inductances with the other phases. In this work, for the purposes of transient fault calculation, it is assumed the effect of the mutual inductances is negligible in light of the large grid inductance ( $0.58 \Omega$ ) and the significant increase of resistance of the power cable. This is done to avoid the need to create a system of ODEs.

### 7.1.2 Heat transfer in solids

Modelling of the temperature evolution in a superconductor is no different than any other material. Using the 2D equation for conductive heat transfer:

$$\rho_v C_p \frac{dT}{dt} = k \left( \frac{d^2 T}{dx^2} + \frac{d^2 T}{dy^2} \right) + Q - q \quad (7.4)$$

where  $\rho_v$  – mass density,  $C_p$  – specific heat capacity,  $T$  – temperature,  $k$  – thermal conductivity (isotropic),  $Q$  – heat energy from local heat source (equal to zero in insulation/non-conductive domains, and equal to  $JE$  in conducting domains),  $q$  – heat energy intake from neighbouring domains. The equation is implemented via COMSOL's Heat Transfer module.

### 7.1.3 Heat transfer in fluids

In fluids, heat transfer generally occurs via conduction and convection. Particularly in cooling systems, heat is moved by forced convection that depends on the velocity of the fluid and other factors. The COMSOL module Heat Transfer in Fluids provides the 1D

equation to be used in this chapter:

$$\rho_v C_p \frac{dT}{dt} + v \rho_v C_p \frac{dT}{dz} = k \frac{d^2 T}{dz^2} - q \quad (7.5)$$

where  $v$  – the velocity of the fluid in the pipe or channel, and the other variables are as described after Equation 7.4.

#### 7.1.4 1D fluid flow approximation

Superconducting power cables need to be cooled continuously to ensure their temperature does not increase beyond the permissible boundaries. In cables with high temperature superconducting wires, the cooling is achieved via forced convection of liquid nitrogen.

In practice, the flow of LN<sub>2</sub> can be either laminar or turbulent, as indicated by the Reynolds number, which develops a velocity front in the flow channel. Due to the inherent 2D/3D nature of a velocity front, a computational fluid dynamics (CFD) model requires at least a 2D-axisymmetric model to simulate the entire length of the cable. Furthermore, LN<sub>2</sub> has a discrete radial thermal conductivity, which means that the radial temperature rise within the coolant cannot be instantaneous.

In order to simplify the simulation and reduce computation time, it is possible to use a 1D model instead [52]. In this model, there is no velocity front and the thermal conductivity of LN<sub>2</sub> does not play a role. All heat transferred into the liquid is immediately spread through the entire width of the coolant channel (the physical system of the coolant, keeping in mind the model is 1D) and is carried away via forced convection. A possible shortcoming of this approach is a potentially unrealistic temperature profile of the LN<sub>2</sub> (but the temperature at the outlet is not affected). Despite this, the omission of CFD offers a valuable speed-up and, in this work, it is important to verify the used electromagnetic techniques against those in literature before introducing CFD. Using CFD instead of 1D heat transfer in the coolant should be done as part of future work, where the simulation could ideally be verified against measurements.

This 1D model is achievable with the Heat Transfer in Fluids module in COMSOL. The module allows for the LN<sub>2</sub> velocity to be specified. As the model has less dimensions than the real system, it is important to use the correct values for the channel's cross-section perimeter and area as they are key in calculating the amount of heat that crosses between the solid material and the liquid.

## 7.2 The AmpaCity cable

The AmpaCity project with its thousand metres length [53] is the longest superconducting power cable installed in a real power grid to date. It is a three phase, tri-axial cable, consisting of first generation tapes spread into three phases with one layer per phase.

The geometric and operational characteristics of the cable are described in Table 7.1 and Table 7.2, respectively. In Table 7.4, the material specifications in relation to heat transfer are displayed — these are assumed to be temperature-independent. Several published papers make it possible for a FEM model to be developed and verified against other models and real test results.

The cable is constructed in the following way [57]. A former lies in the centre of the structure. It is constructed from a hollow corrugated steel tube with parameters as in Table 7.3. The supply flow of the coolant flows within this tube, also called the tubular duct.

Above the former lies the first superconducting phase — as the other two, it consists of standard first generation tapes, formed of Bi-2223 filaments in a silver matrix. Between each phase lies a PPLP insulation layer, and between each phase and adjacent insulation there is a semiconductor layer. For the purposes of this chapter, it is assumed that semiconductor layer is absorbed into the PPLP.

After the third phase lies another insulation layer, followed by the neutral conductor, made of copper. Outside of the copper neutral is the annular duct, where the return flow of the coolant flows. The annular duct is bound by the inner wall of the cryostat. The actual cable can be seen in Figure 7.2 [63].

### 7.3 Temperature profile of the AmpaCity cable

To obtain the steady-state temperature along the width and length of the cable, two separate components must be constructed and coupled — a 1D liquid nitrogen model, and a 2D-axisymmetric conductor/insulation model. Subsequently, these will be used for the recovery simulations as well.

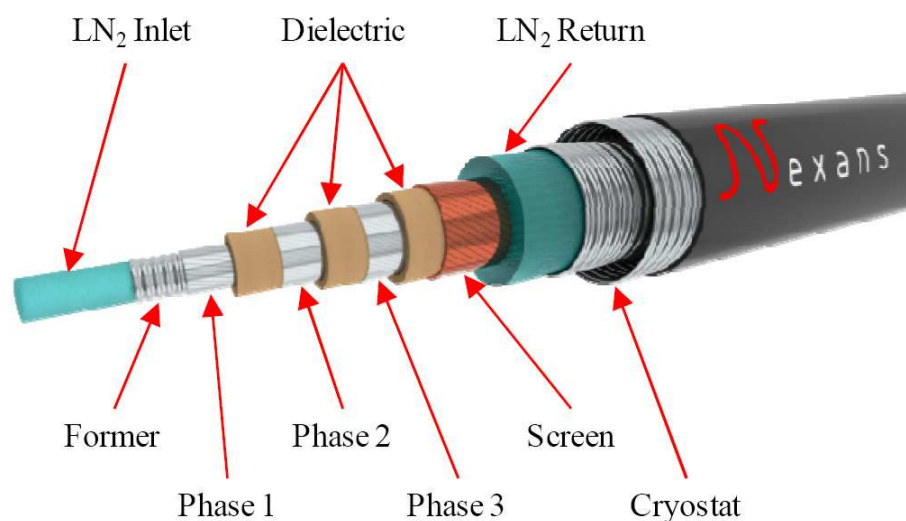


Figure 7.2: The geometry and layout of the AmpaCity Triax cable. From [63]  
© 2013 IEEE.

# of phases	3	[52,57]
# of layers per phase	1	[52,57]
# tapes per layer	Ph 1: 22	
	Ph 2: 26	[52,57]
	Ph 3: 30	
Twist angle	16° (all phases)	[119]
Outer radius of former ( $r_s$ )	17 mm	[57]
Inner radius of 1st phase	17 mm	[57]
Inner radius of 2nd phase	20.61 mm	[57]
Inner radius of 3rd phase	24.22 mm	[57]
Inner radius of copper neutral	27.83 mm	[57]
Inner radius of annular LN <sub>2</sub> channel ( $r_{r-i}$ )	30.83 mm	[57]
Inner radius of cryostat ( $r_{r-o}$ )	40 mm	[57]
Thickness of PPLP insulation layer	3.4 mm	[57]
Cable length	1000 m	[52,53,57]
Tape width	4 mm	[57]
Tape thickness	0.21 mm	[57]
Ratio of HTS to total area	0.3	private comm.
Ratio of Ag to total area	0.7	private comm.

Table 7.1: Geometric specification of the AmpaCity cable. Information is extracted from [52, 53, 57, 119].

### 7.3.1 Modelling of the coolant

The 1D Heat Transfer in Fluids handles the temperature of the liquid nitrogen inside both the supply and return flows; the standard equation is presented in subsection 7.1.3 and the basic principle of the 1D approximation is discussed in section 7.1.4.

A 1D component is defined within COMSOL. Then, a domain (a line) is built, with a length  $l$  equal to that of the cable ( $l = 1000$  metres for AmpaCity). A point is defined at each  $l_{dz} = l/5 = 200$  m along the length. This geometry is shared between two 'Heat Transfer in Fluids' physics — one solving for the temperature within the supply flow  $T_s$  and the other solving for the temperature within the return flow  $T_r$ .

#### Boundary conditions

The geometry and all boundary conditions can be seen in the infographic in Figure 7.3. Each variable requires two boundary conditions. At  $z = 0$  m,  $T_s$  is equal to the inlet temperature of 68 K via the Inflow boundary condition, while for  $T_r$  the Outflow boundary condition is used. At  $z = 1000$  m,  $T_s$  needs the Outflow boundary condition, while  $T_r(1000) = T_s(1000)$  — e.g. the outflow temperature of the supply flow is fed back into the return flow.

Tape $I_c(77K, 0T)$	200 A
Tape $n(77K, 0T)$	14
	Ph 1: 4400 A
Total $I_c$	Ph 2: 5200 A
	Ph 3: 6000 A
RMS phase voltage	10,000 V
LN <sub>2</sub> input temperature	68 K
Mass flow rate	0.425 kg/s
Cryostat heat leakage	1.7 W/m
$R_{\text{grid}}$	0.04 $\Omega$
$L_{\text{grid}}$	0.58 $\Omega$
Viscosity $\nu_{LN2}$	$166.678 \times 10^{-6}$ Pa s
Fault duration	0.1 s

Table 7.2: Operational specification of the AmpaCity cable. Information is extracted from [57] and obtained through private communication (Dr Wesley Tiago Batista de Sousa, Karlsruhe Institute of Technology, October 2019)

Wall thickness	0.3 mm	$s_s$
Surface factor	0.146 m <sup>2</sup> /m	$F_s$
Groove depth (tube width)	1 mm	$t_{gr}$

Table 7.3: Parameters of the corrugated tube in the AmpaCity cable. Information is extracted from [52]

	k (W/mK)	$C_p$ (J/kgK)	$\rho_v$ (kg/m <sup>3</sup> )
Bi-2223	150	200	5600
Silver	480	225.2	10470
St. Steel	1	200	7900
Copper	534.186	244.6	8960
PPLP	0.147051	430	1098
LN <sub>2</sub>	0.147051	2024.95	811.229

Table 7.4: Thermal parameters of the materials of the AmpaCity cable. All values are obtained through private communication with Dr Wesley Tiago Batista de Sousa from KIT in relation to [57].

Each of the two physics modules requires the hydraulic cross-sectional area  $A_c$  (the area of the cross-section where the fluid is flowing) and that area's perimeter  $P_c$  to be entered. For  $T_s$ ,  $P_c = 2\pi(r_s - t_{gr}/2) = P_s$  and  $A_c = \pi(r_s - t_{gr}/2)^2 = A_s$ . ( $r_s - t_{gr}/2$ ) is the averaged radius of the steel former, considering its corrugated structure. For  $T_r$ ,  $P_c = 2\pi r_{r-o} = P_{r-o}$  and  $A_c = \pi(r_{r-o}^2 - r_{r-i}^2) = A_r$ . The inflow of heat from outside the cryostat wall into the return flow is calculated using

the specified value of  $Q_{leak} = 1.7 \text{ W/m}$ . It is implemented on the inner wall of the cryostat via the 'Out-of-plane Heat Flux' node by specifying the general inward heat flux  $q_{leak}$  in  $\text{W/m}^2$ :

$$q_{leak} = \frac{Q_{leak}l}{P_{r-o}} = 6.8397 \quad (7.6)$$

where  $l$  is the length of the cable and  $P_{r-o}$  is the perimeter of the inner cryostat wall.

The heat transfer between the cable materials and the coolant is dependent on the respective heat transfer coefficient —  $h_s$  for the supply flow and  $h_r$  for the return flow. However, as described above, COMSOL's 1D Heat Transfer in Fluids module allows for only one value for the channel surface perimeter to be specified. This is because the software expects a "solid" structure with only an outer wall for the channel, as opposed to a "hollow" structure with an inner and outer wall, such as an HTS cable's annular duct. The heat flux crossing the cable's wall from outside the cable into the return flow is defined in the following way:

$$q_{r-i} = P_c h (T_{wall,r} - T_{ln,r}) \quad (7.7)$$

If  $P_c = P_{r-o}$  (the return flow channel's outer boundary perimeter) in order to fit the external heat leak condition, the perimeter of the return flow channel's inner boundary  $P_{r-i}$  must be inserted by another method:

$$h = h_r \frac{P_{r-i}}{P_{r-o}} \quad (7.8)$$

$$q_{r-i} = P_{r-i} h_r (T_{wall,r} - T_{ln,r}) \quad (7.9)$$

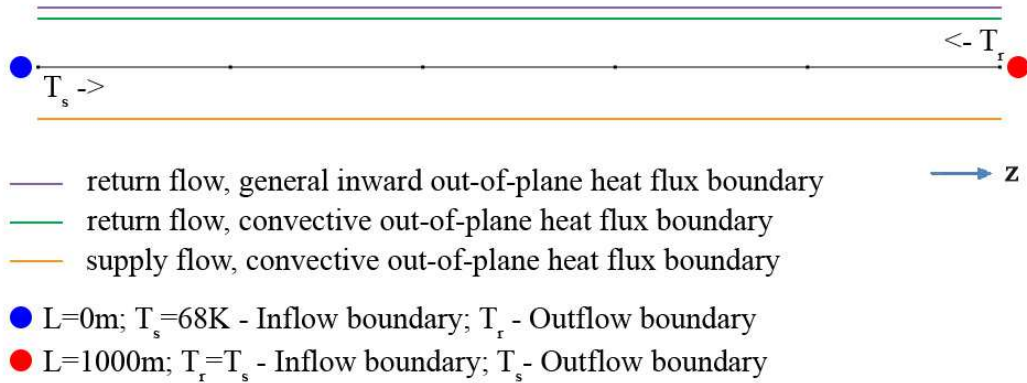


Figure 7.3: The geometry of the physics in the 1D coolant simulation. The blue and red circles indicate a point boundary condition; the thick coloured lines indicate a cable-long domain boundary condition; the thin black line with dots on it is the actual 1D domain — each dot is 200m apart.

For the supply flow, no modifications to the 'Out-of-plane Heat Flux' node are needed:

$$q_s = P_s h_s (T_{wall,s} - T_{ln,s}) \quad (7.10)$$

where  $T_{wall,s}$  is the temperature of the cable's solid part at the boundary with the supply flow, and  $T_{wall,r}$  is the temperature of the cable's solid part at the boundary with the return flow.

### Heat transfer coefficients

The heat transfer coefficients  $h_s$  and  $h_r$  must be calculated accurately depending on the system properties. A procedure for doing so is described in [120]. Firstly, it must be determined whether the flow is laminar or turbulent, through the Reynolds number:

$$Re = \frac{\rho_{v,ln} v d}{\nu_{ln}} \quad (7.11)$$

where  $\rho_{v,ln}$  is the density of the liquid nitrogen,  $v$  – average velocity of the fluid in the channel,  $d$  – hydraulic diameter of the channel,  $\nu_{ln}$  – liquid nitrogen viscosity.

Since the mass flow of the coolant is assumed constant, but there are two channels with a different geometry and hydraulic area, the average velocity (m/s) in each channel will be different:

$$v_s = \frac{m}{A_s \rho_{v,ln}} \quad (7.12)$$

$$v_r = \frac{m}{A_r \rho_{v,ln}} \quad (7.13)$$

Returning to the Reynolds number equation:

$$Re_s = \frac{\rho_{v,ln} v_s d_s}{\nu_{ln}} = 98380 \quad (7.14)$$

$$Re_r = \frac{\rho_{v,ln} v_r d_r}{\nu_{ln}} = 11459 \quad (7.15)$$

As for this model both Reynolds numbers are visibly larger than the turbulent flow value of 4000 (for pipes), the flow in both supply and return flow is turbulent.

Then, the formula for the heat transfer coefficient in turbulent flow is as follows [121]:

$$h = \frac{k_{ln} 0.023}{d} Pr^{0.4} Re^{0.8} \quad (7.16)$$

Where  $Pr$  is Prandtl's number:

$$Pr = \frac{\nu_{ln} C_{p,ln}}{k_{ln}} \quad (7.17)$$

and  $C_{p,ln}$  – specific heat capacity and  $k_{ln}$  – thermal conductivity of the liquid nitrogen.

As the steel former is in fact a corrugated tube, it is needed to modify the heat transfer coefficient to take this into account within the calculation. According to [52], the new



value for the supply flow heat transfer coefficient  $h^*$  is:

$$h_s^* = h_s \frac{F_s}{\pi(2r_s - s_s)} \quad (7.18)$$

where  $F_s$  is the surface factor of the corrugated tube and  $s_s$  is the wall thickness.

If  $d_s$  and  $d_r$  are the hydraulic diameters of the supply and return flow respectively, the final equations are:

$$h_r = \frac{k_{ln} 0.023}{d_r} \left( \frac{\nu_{ln} C p_{ln}}{k_{ln}} \right)^{0.4} \left( \frac{\rho_{v-ln} \nu_r d_r}{\nu_{ln}} \right)^{0.8} \quad (7.19)$$

$$h_s^* = \frac{k_{ln} 0.023}{d_s} \left( \frac{\nu_{ln} C p_{ln}}{k_{ln}} \right)^{0.4} \left( \frac{\rho_{v-ln} \nu_r d_s}{\nu_{ln}} \right)^{0.8} \frac{F_s}{\pi(2r_s - s_s)} \quad (7.20)$$

### Mesh and discretization

The domain is divided into 1-metre-long elements. For the AmpaCity cable, it means a total of 1000 elements. The discretization is linear. It is a very simple implementation with few required settings, however there are several component couplings which will be explored in detail further down in this section.

### 7.3.2 Modelling of the temperature along the total width and length of the cable

A problem exists of how exactly to simulate the temperature distribution within the cable, both in the radial and the longitudinal direction. Examining the literature, it can be seen that full-length 2D models built with finite differences ([121] and subsequently other studies) may serve as a stepping stone to developing and describing a FEM 2D-axisymmetric model to achieve the same purpose.

Firstly, a 2D-axisymmetric component is created within COMSOL. The only physics within this component is the 'Heat Transfer in Solids' module, with the temperature variable  $T_0$ . The standard equation is presented in subsection 7.1.2.

The geometry consists of the former, insulation and conduction layers, as well as the neutral conductor — their specifications are listed in Table 7.1. They are built for the entire length  $l = 1000$  m of the cable and a compressed, not-to-scale representation of the final geometry can be seen in Figure 7.4. As in the 1D model, the whole geometry is divided into five parts via lines every 200 metres.

Each phase is assumed to be a monoblock where the material is a mixture of HTS and silver. If  $s_{hts}$  is the fraction of superconductor in the tape's cross-section, the effective

specific heat capacity is:

$$C_{p,con} = C_{p,hts}s_{hts} + C_{p,Ag}(1 - s_{hts}) \quad (7.21)$$

And the effective mass density:

$$\rho_{v,con} = \rho_{v,hts}s_{hts} + \rho_{v,Ag}(1 - s_{hts}) \quad (7.22)$$

The thermal conductivity of the monoblock is assumed to be equal to the thermal conductivity of the HTS material, in line with literature.

### Boundary conditions

At the beginning (zero metres) and the end of the cable ( $l = 1000$  m), the simplest 'Thermal Insulation' (total heat transfer through the boundary equal to zero) is applied along the radial direction.

At the longitudinal boundaries, 'Heat Flux' boundary conditions using convective heat flux are applied. At the inner boundary, towards the supply flow, the heat transfer coefficient  $h_s^*$  is applied (Equation 7.20) and the 'external' temperature at the given length is equal to  $T_s$  – the temperature of the supply flow coolant. At the outer boundary, towards the return flow, the coefficient is  $h_r$  (Equation 7.19) and the external temperature

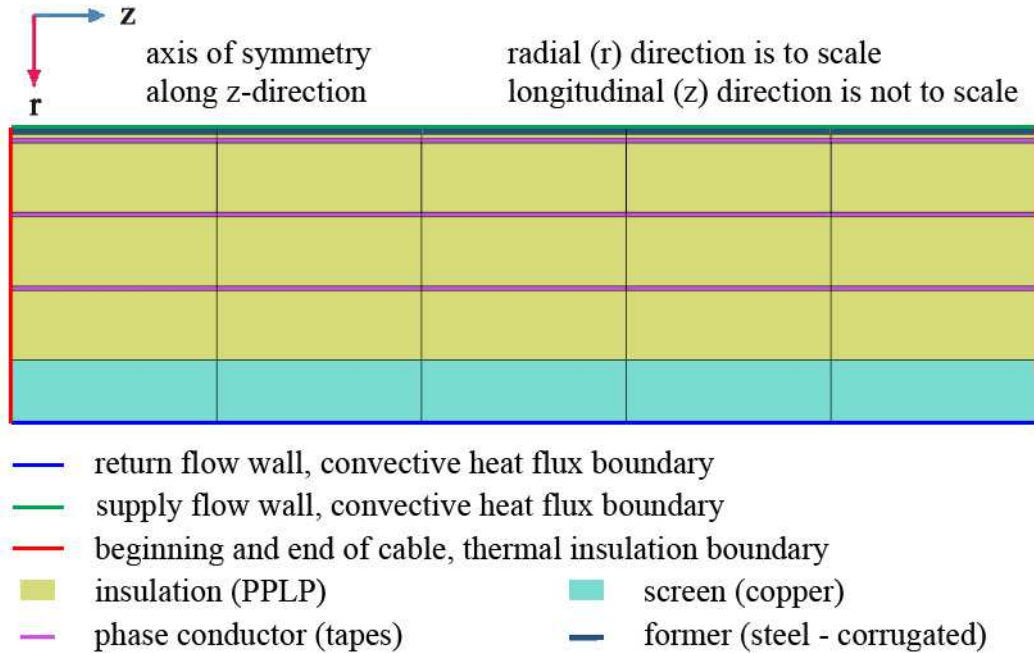


Figure 7.4: The geometry of the physics in the total width and length of the cable. The solid red lines indicate the thermal insulation boundaries at the beginning and end of the cable; the blue line is the convective heat flux boundary between the cable and the coolant's return flow; the green line is the convective heat flux boundary between the cable and the coolant's supply flow. The cable is split into five, 200-metre-long domains.

is  $T_r$ . This setup is identical with the heat transfer in the 1D coolant physics, which ensures the conservation of heat once the models are coupled together.

### Mesh and discretization

The mesh is divided, as in the 1D coolant physics, into 1-metre-long sections. A mapped mesh is used in order to minimize the size of the model. Within the larger domains of the insulation and the neutral conductor, 25 elements per edge (radially) are introduced. For the smaller domains of the former and HTS layers, 4 elements per edge are used.

Due to the extremely high heat gradient once each phase starts heating up, care must be taken around the borders between each phase and the surrounding material. If the mesh is too coarse, numerical errors may be introduced that can result in calculation inaccuracies, including the introduction of regions with abnormal and unrealistic temperature decrease. To combat this, a boundary layer can be introduced on the edges on each side of each phase. It may be necessary to use at least 4 or 5 boundary layers and improve the surrounding mesh in order to achieve good numerical accuracy.

In order to minimize the degrees of freedom, a linear discretization is used — even then there are 720,000 domain elements and over 50,000 boundary elements.

### 7.3.3 Coupling of the coolant and cable body heat transfer physics

So far three variables have been defined — the temperature of supply flow  $T_s$ , the temperature of return flow  $T_r$  and the temperature within the body of the cable  $T_0$ . Within COMSOL, these variables use one physics module each for a total of three modules, and these are spread between two components.

These variables do not share the same geometry, nor dimensions. In order to be able to simulate them together, it is necessary — regardless of the FEM software — to couple them. In COMSOL, this is achieved by coupling the separate components together via so-called "component couplings", which include operators, extrusions and projections. In the given model, the coupling is achieved via a linear extrusion that maps the walls of the 2D-axisymmetric cable geometry onto the 1D domain and vice-versa.

As described in the previous subsection, the supply flow strictly exchanges heat with the inner wall of the cable itself ( $T_s \rightleftharpoons T_0$ ), and the return flow strictly exchanges heat with the outer wall of the cable body ( $T_r \rightleftharpoons T_0$ ), both while ensuring the conservation of energy holds. Both achieve this via a convective heat transfer boundary condition.

The heat transfer into the supply flow (and into the cable is the negative value) is:

$$q_s = h_s^*(T_{0(wall,in)} - T_s)P_s \quad (7.23)$$

And the heat transfer into the return flow (once again the heat into the cable will be the negative value) is:

$$q_{r-i} = h_r(T_{0(wall,out)} - T_r)P_{r-i} \quad (7.24)$$

$T_{0(wall,in)}$  and  $T_{0(wall,out)}$  can be seen as the green and blue boundary conditions in Figure 7.5, respectively. The couplings are also illustrated in Figure 7.5.

### 7.3.4 Simulation of the steady state

A steady state temperature distribution of the coolant along the AmpaCity cable is simulated in [52] and subsequently reused in [57].

To achieve the simulation, it is necessary to run the coupled physics described above, in a time-dependent solver. A PARDISO or MUMPS direct solver with a Fully Coupled approach are enough; the solver itself can do free timestepping and the relative tolerance is 0.0001. The solver must simulate for a sufficiently long time to ensure the temperature has settled in a steady-state; it was observed that 1e6 seconds is long enough for that to happen. Only the starting (0 seconds) and ending (1e6 seconds) points in time need be saved, as nothing else but the end point is required once the onset of steady state is determined. A simulation on a desktop PC with Intel i7-6700 CPU, 3.40GHz, with 16 GB of RAM, managed to solve for all 735,000 degrees of freedom in 3 minutes and 18

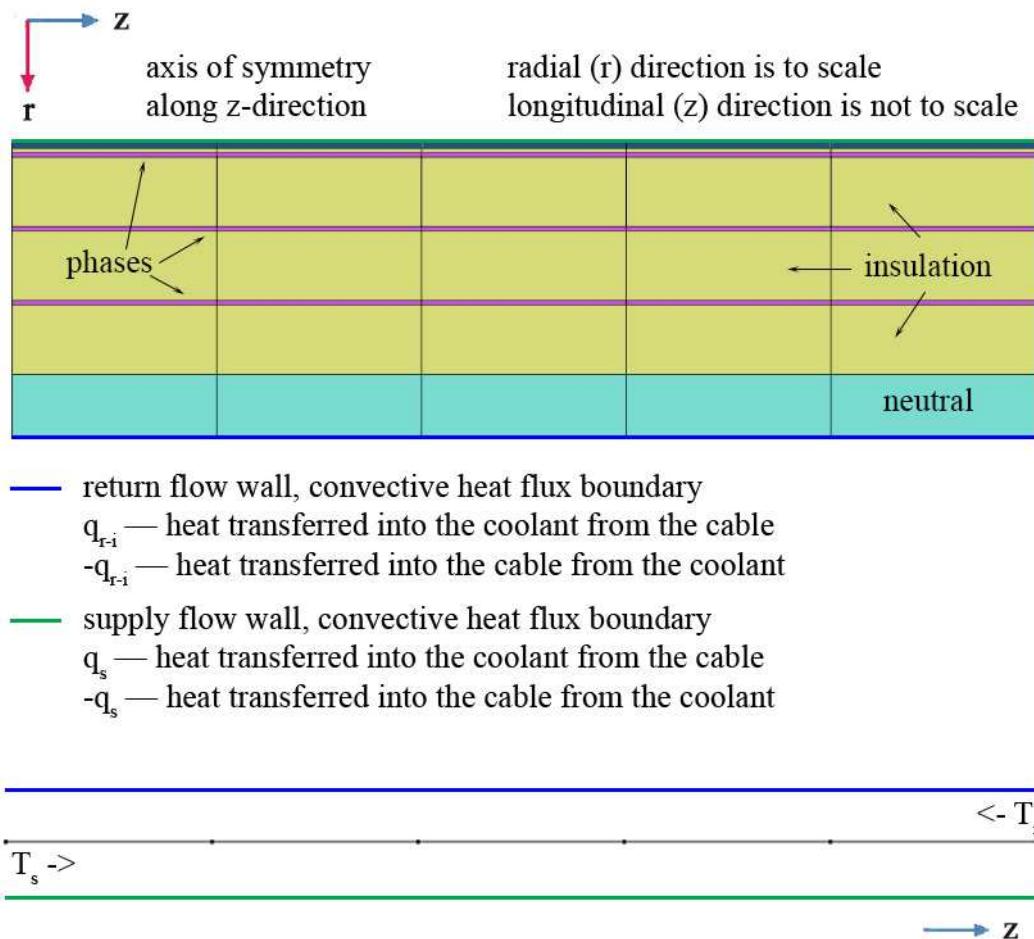


Figure 7.5: The coupling of the coolant supply and return flow temperatures and the body temperature.

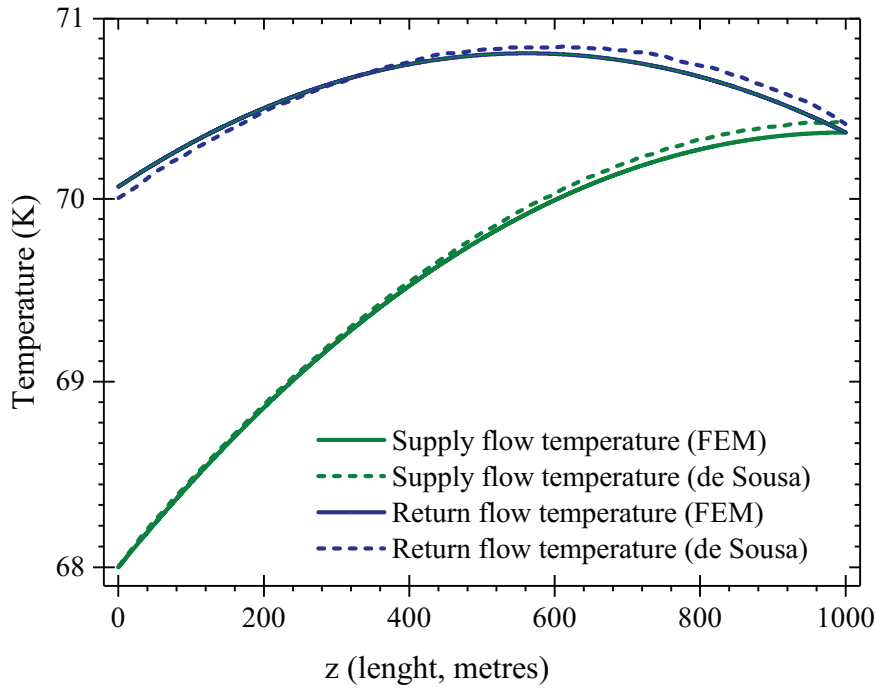


Figure 7.6: The steady-state temperature along the AmpaCity cable. The comparison is between the simulated values via FEM and the finite differences model in [57].

seconds.

The result of the simulation, together with the extracted data from [57], is available in Figure 7.6. The same profile has been observed elsewhere in literature as well [122]. The temperature of the coolant at the outflow of the cable is 70.07 K, marginally above the prescribed value of 70 K; the maximum temperature is 70.8 K which is a little under the 70.85 K from the FD model in [57]. The length at which the maximum temperature occurs is 562 metres instead of 610-620 metres, and the temperature at the end of the cable is 70.37 K instead of 70.42 K.

The inequalities may be attributed to the different model construction. Furthermore, the temperature at the end of the cable (turn-around point for the coolant flow), but not the temperature at the return flow outlet, is influenced significantly by the thermal conductivity of the PPLP insulation.

## 7.4 Overcurrent response of the AmpaCity cable

The main goal of the model is to utilize 2D FEM physics to simulate the overcurrent response using tape homogenization as described in Chapter 5. As such, at the core of the entire model are the  $H$ -formulation ('General Form PDE') and the 'Heat Transfer in Solids' physics module. The former introduces the in-plane magnetic field defined by  $H_x$ ,  $H_y$ , and the latter contains the local cross-sectional temperature  $T$ .

### 7.4.1 Construction of the 3-phase cable and physics

Only one quarter of the AmpaCity's cross-section is simulated, due to symmetry. Other cable models may require the simulation of one half depending on the number of tapes and layers.

The geometry is built step-by-step to ensure it conforms to Table 7.1.

The  $H$ -formulation used in this Chapter is defined in Chapter 4.2.1 and used in subsequent Chapters via the 'General Form PDE'. The symmetry conditions are implemented via Dirichlet boundary conditions on the x ( $H_x = 0$ ) and y ( $H_y = 0$ ) axes. The  $H$ -formulation starts with  $H_x = 0$ ;  $H_y = 0$  and  $dH_x/dt = 0$ ;  $dH_y/dt = 0$  everywhere.

#### Heat transfer

Heat transfer is again implemented in accordance with Equation 7.4 in the 'Heat Transfer in Solids' module. The simulated domains are only the three phases, the insulation and the neutral conductor. Then, there are three boundary conditions — the thermal insulation along the symmetry boundaries, the convective heat flux towards the supply flow ( $T_s \rightleftharpoons T$ ) and the convective heat flux towards the return flow ( $T_r \rightleftharpoons T$ ). The latter two are again implemented via the 'Heat Flux' nodes. Heat generation within the conductors is achieved via the product of current density and electric field  $JE$ .

Regarding the convective heat flux boundaries, the heat transfer coefficients are  $h_s^*$  and  $h_r$  as calculated in the previous section. The external temperature at the boundaries is equal to the liquid nitrogen temperature of the supply  $T_s$  or return flow  $T_r$ , which are taken at the corresponding (six) points along the length of the cable.

$$q_s = h_s^*(T_s - T) \quad (7.25)$$

$$q_{r-i} = h_r(T_r - T) \quad (7.26)$$

If the values above are positive, heat is flowing into the cable, and if they are negative, heat is flowing into the coolant. An illustration of all boundary conditions in the system is shown in Figure 7.7.

As the initial conditions are calculated using the 1D coolant model and the 2D-axisymmetric model, there is no temperature distribution within the 2D cross-sectional model initially. The cross-sectional model needs to somehow obtain that distribution at the correct location along the cable. To achieve this, only the heat transfer module is allowed to run from  $T(0) = 68 \text{ K}$ , using the final values of  $T_s$  and  $T_r$  at the appropriate length along the cable as boundary conditions, until steady state is reached.

### 7.4.2 Equivalent resistance and temperature dependencies

Let  $A_t$  – area of a tape’s cross-section,  $A_{hts}$  – area of the tape’s *actual* superconducting material,  $A_{hom}$  – area of the tape’s homogenized superconducting domain,  $A_{Ag}$  – area of the tape’s *actual* matrix material (silver).

#### Critical current and resistivity

The local critical current of the superconductor is, based on Equation 4.5 and [123]:

$$J_c(B, T) = \begin{cases} 0, & \text{if } T \geq T_c \\ J_{c0} \times f(B_{\perp})g(B_{\parallel})m(T), & \text{otherwise} \end{cases} \quad (7.27)$$

which is essentially the same equation as in Equation 4.31 but with an added condition that when the temperature is higher than the critical temperature, the critical current density is zero. Here  $m(T)$  is the critical current temperature dependence function as

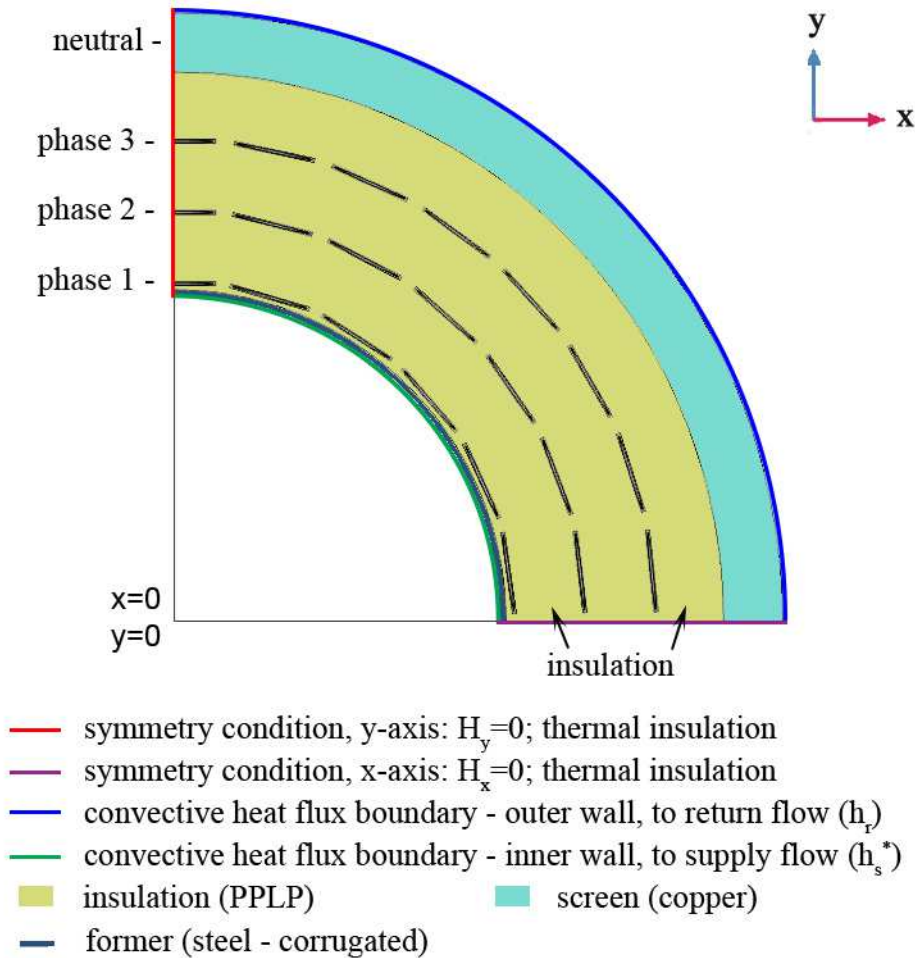


Figure 7.7: The 2D cross-section for  $H$ -formulation and heat transfer, including boundary conditions.

per Equation 4.16 but normalized by  $J_{c0}$ :

$$m(T) = \frac{T_{LN2}}{(1 - T_{LN2}/T_c)^{3/2}} \times \left(1 - \frac{T}{T_c}\right)^{3/2} \quad (7.28)$$

where  $T_{LN2}$  is the reference temperature.

When applying Equation 7.27 in COMSOL, internal conditions may be necessary in order to ensure that no numerical problems are caused by  $T \geq T_c$  and  $J_c(B, T) = 0$ .

The value of the exponent  $n$  is as in Equation 4.32 but with the expanded field dependence:

$$n(B, T) = \begin{cases} 3, & \text{if } T \geq T_c \\ n_0 \times f(B_\perp)g(B_\parallel) \frac{T_{LN2}}{T}, & \text{otherwise} \end{cases} \quad (7.29)$$

Let  $\rho_{hom}$  be the resistivity that the  $H$ -formulation model uses within the homogenized superconducting domain,  $\rho_n(T)$  – the normal state resistivity of the superconducting material,  $\rho_{hts}$  – the resistivity of the *actual* superconducting material,  $\rho_{Ag}(T)$  – the resistivity of the silver matrix material.

Then, if  $\rho_{plaw}$  holds the power law:

$$\rho_{plaw} = \frac{E_c}{J_c(B, T)} \left| \frac{J}{J_c(B, T)} \right|^{n-1} \quad (7.30)$$

The resistivity of the *actual* superconducting material  $\rho_{hts}$  follows Equation 4.4 and the provisions in Section 4.1.1:

$$\rho_{hts} = \frac{\rho_{plaw}\rho_n}{\rho_{plaw} + \rho_n} \quad (7.31)$$

If  $s_{hom,ag}$  is the fraction of silver in the domain:

$$s_{hom,ag} = \frac{A_{hom} - A_{hts}}{A_{hom}} \quad (7.32)$$

Then:

$$\rho_{hom} = \frac{1}{(1 - s_{hom,ag})/\rho_{hts} + s_{hom,ag}/\rho_{Ag}} \quad (7.33)$$

$\rho_{hom}$  is used within the model to calculate the resistivity within the homogenized domain and  $\rho_{hts}$  is used within the macroscopic resistance equations in order to estimate the correct value of the cable's resistance. This separation is needed because the homogenized domain approximation only makes sense within the FEM environment, and using circuit equations requires the values for the material's cross-sectional area and resistance as they would be in reality. Equation 7.31 is in line with Equations 4.4 and 4.30.

Additionally, the temperature dependencies of the normal state resistivity  $\rho_n$  and silver resistivity  $\rho_{Ag}$  must be defined:

$$\rho_n = aT_{hts} + b \quad (7.34)$$



$$\rho_{Ag} = cT_{Ag} + d \quad (7.35)$$

Where  $T_{hts}$  and  $T_{ag}$  are the temperatures of the HTS and silver material, respectively. Also,  $a = 4.53 \times 10^{-8}$ ,  $b = 1.15 \times 10^{-6}$ ,  $c = 7 \times 10^{-11}$  and  $d = -2 \times 10^{-9}$ . All these values are graciously provided by Dr Wesley Tiago Batista de Sousa from KIT through private communication.

The last remaining question is what effective values to assign the homogenized HTS domain for the thermal capacity  $k_{hom}$ , specific heat  $C_{p,hom}$  and density  $\rho_{v,hom}$ . The weighed values are taken based on the fraction of each material within the homogenized domain:

$$C_{p,hom} = C_{p,hts}(1 - s_{hom,ag}) + C_{p,Ag}s_{hom,ag} \quad (7.36)$$

$$\rho_{v,hom} = \rho_{v,hts}(1 - s_{hom,ag}) + \rho_{v,Ag}s_{hom,ag} \quad (7.37)$$

And finally, the thermal conductivity of the homogenized domain is allowed equal to the superconductor value, such that  $k_{hom} = k_{hts}$  as per [52].

### Resistance of the cable

The average resistance per metre of the superconductor material of the cable  $R_{k,hts}$  at a given time can be found by obtaining the average value of the resistivity  $\rho_{k,hts,ave}$  within the homogenized superconducting domain. Then:

$$R_{k,hts} = \frac{\rho_{k,hts,ave}}{nA_{hts}} \quad (7.38)$$

where  $k = 1; 2; 3$  indicates the phase and  $n = 22; 26; 30$  is the corresponding number of tapes per phase.

Similarly, for the matrix material:

$$R_{k,Ag} = \frac{\rho_{k,Ag,ave}}{nA_{Ag}} \quad (7.39)$$

where  $\rho_{k,Ag,ave}$  is the average value of the resistivity within the silver matrix material. Then, the total resistance of a phase  $k$  can be expressed as two resistances connected in parallel:

$$R_k = l_k \frac{R_{k,hts}R_{k,Ag}}{R_{k,hts} + R_{k,Ag}} \quad (7.40)$$

where  $l_k$  is the actual length of the tapes within the cable. When the layers are twisted,  $l_k$  is always a little larger than the total length of the cable:

$$l_k = \frac{l}{p_k} \sqrt{p_k^2 + c_k^2} \quad (7.41)$$

where  $p_k$  is the pitch length of the layer  $k$  and  $c_k$  is the layer circumference (where the radius is taken through the exact middle of the layer).

The resistance with which the transient fault is simulated  $R_{k,tot}$  must also include the lumped resistance of the grid upstream from the HTS cable  $R_{grid}$ :

$$R_{k,tot} = R_k + R_{grid} \quad (7.42)$$

### 7.4.3 Solving for the duration of the fault

As was mentioned before, the cable was split in five equal parts of 200 m each. These are bounded by six individual cross-sections, and each one of these is modelled separately. Such a split is required since the temperature rise along the cable may differ. There are two ways to simulate these six cross-sections.

1. Distributed parametric sweep, simulated in parallel (requires computing cluster for effective speed-up). Here, each cross-section is decoupled from the rest and assigned a parameter. The difference between the values of the calculated damped transient current between each cross-section is assumed negligible — calculation for the current value at each cross-section is done solely within that cross-section.
2. Simultaneously running all six cross-sections within one simulation. Here the current depends on the whole cable, which is more accurate, but at the cost of simulation time and model complexity. Each cross-section requires its own variables, e.g.  $H_{x1}, H_{x2}, H_{x3}, \dots, H_{y1}, H_{y2}, H_{y3}, \dots, T_1, T_2, T_3, \dots, J_1, J_2, J_3, \dots$ , which increases the number of physics nodes. The solution may take advantage of the segregated solver option in COMSOL to simulate all  $H$ -formulation variables first and all temperature variables second, in order to speed up timestepping and decrease memory usage. On an office PC with Intel i7-6700 CPU, 3.40GHz, with 16 GB of RAM, the simulation completed in 55 hours, compared to 15 hours for the parallel-solved parametric sweep on a cluster. However, if a cluster is not available, then a simultaneous simulation would be considerably faster than a parametric one. In the case of the AmpaCity cable, simultaneously solving all cross-sections did not yield any noticeable differences in the results compared to the parallel simulation.

If the first option is chosen, six parameters are introduced:  $p_0, p_{200}, p_{400}, p_{600}, p_{800}, p_{1000}$ . Each parameter can take the value of 1 or 0 and the number in the subscript indicates the distance from the beginning of the cable (coolant inlet). If  $p_k = 1$  then all other parameters are equal to 0 and the cross-section presently simulated is at length  $l = k$ . This is implemented in the model via modifying Equations 7.25 and 7.26:

$$q_s = h_s^* [(T_{s,0} - T)p_0 + (T_{s,200} - T)p_{200} + (T_{s,400} - T)p_{400} + (T_{s,600} - T)p_{600} + (T_{s,800} - T)p_{800} + (T_{s,1000} - T)p_{1000}] \quad (7.43)$$

$$q_{r-i} = h_r [(T_{r,0} - T)p_0 + (T_{r,200} - T)p_{200} + (T_{r,400} - T)p_{400} + (T_{r,600} - T)p_{600} + (T_{r,800} - T)p_{800} + (T_{r,1000} - T)p_{1000}] \quad (7.44)$$

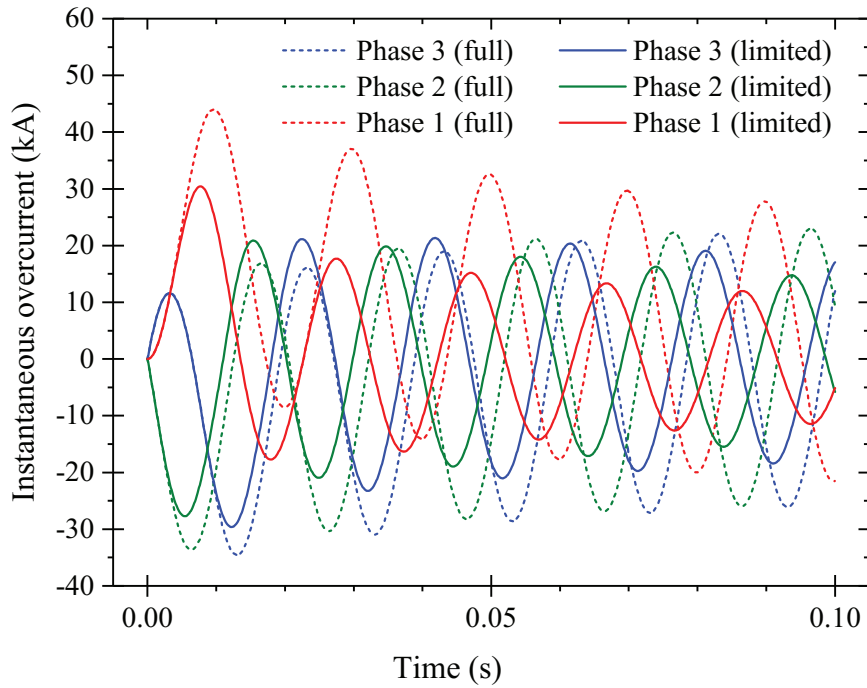


Figure 7.8: The simulated full and limited fault currents in the AmpaCity model.

Here  $T_{s,k}$  and  $T_{r,k}$  indicate the temperature of the supply and return flows, respectively, at length  $l = k$ . This allows a parametric sweep to be performed easily.

The default MUMPS solver in COMSOL can efficiently perform the simulation without further settings. However, care must be taken to ensure the correct values are used for the initial conditions.

In Figure 7.8 the values of the simulated currents are presented for the entire duration of the fault. The values are very close to those obtained in [57], with the first peak of the limited current being calculated as 30,420 V and the value from literature equal to about 32,000 V. This also shows the method of calculation of the resistance is reasonable.

However, on Figure 7.8 there is a phase angle shift between the predicted transient current and the limited fault current. This phenomenon can be best explained by the change of the X/R ratio of the cable, and in particular the change of the resistance R. As per Section 7.1.1, Equation 7.3 describes Kirchoff's Law for a simple cable system:

$$V_s \sin(\omega t + \phi) = RI + L \frac{dI}{dt} \quad (7.45)$$

The general solution to this first-order ordinary differential equation is (via substitution and integration by parts where necessary):

$$I(t) = \frac{V_s}{R^2 + L^2\omega^2} (R \sin(\omega t + \phi) - L\omega \cos(\omega t + \phi)) + Ae^{-\frac{R}{L}t} \quad (7.46)$$

where  $A$  is a constant, residual from integration. The value of  $A$  may be calculated by assuming that at  $t = 0$ ,  $I(0) = 0$ , but doing so is beyond the scope of this explanation. Let  $L\omega = X \Omega$  (reactance):

$$I(t) = \frac{V_s}{R^2 + X^2} (R \sin(\omega t + \phi) - X \cos(\omega t + \phi)) + Ae^{-\frac{R}{L}t} \quad (7.47)$$

Modifying the above equation via a number of arithmetic and trigonometrical transformations leads to:

$$I(t) = \frac{V_s}{\sqrt{R^2 + X^2}} \sin \left( \omega t + \phi - \tan^{-1} \left( \frac{X}{R} \right) \right) + Ae^{-\frac{R}{L}t} \quad (7.48)$$

Here, it can be easily seen that the phase of the fault current is directly influenced by the X/R ratio, which changes as the resistance of the HTS cable increases.

As per Equation 7.3 and considering the variables described throughout the previous sections:

$$V_{s,k} \sin(\omega t + \phi_k) = R_{k,tot} I_k + L \frac{dI_k}{dt} \quad (7.49)$$

$\phi_k$  is the phase shift and  $\phi_k = 0^\circ; 120^\circ; 240^\circ$  for  $k = 1; 2; 3$  respectively.  $I_k$  is the total current flowing in each phase, calculated by integration over all tapes of that phase, as described in Equation 4.28 (and multiplying the result by four to account for 1/4 symmetry). The inductance  $L$  includes both the inductance upstream along the grid and the inductance of the cable. Neither of these values are dependent on current or temperature and as such  $L$  is constant for the purposes of this study.

In COMSOL, the above equation is implemented via a Global Equation subnode within the General Form PDE.

If  $R_{k,tot} = R_{grid}$ , then the non-damped transient fault current can be obtained.

#### 7.4.4 Temperature distribution within the 2D-axisymmetric model

To effectively analyze the temperature profiles in the coupled 1D-to-2D-axisymmetric system, similarly to Section 7.3, it is needed to adapt the results of the discrete simulation of each cross-section.

The 2D-axisymmetric model is already split in five sectors, that is one less than the number of cross-sections — each sector is bound by an upper (towards the end of the cable) and lower (towards the beginning of the cable) cross-section. The heat generated along the cable length in phase  $k$  in each of those sectors can be defined in the following way:

$$Q_{k,axi}(y, z) = \frac{Q_{k,y}}{A_k} \times \frac{y - z}{l_{dz}} + \frac{Q_{k,(y+l_{dz})}}{A_k} \times \frac{1 + (z - y)}{l_{dz}} \quad (7.50)$$

where  $z$  is the longitudinal spatial variable (the equation does not depend on the radial distance),  $A_k$  is the cross-sectional area of the phase  $k$  as seen in the 2D-axisymmetric model,  $l_{dz} = 200$  in metres is the distance between each simulated cross-section,  $y =$

200; 400; 600; 800; 1000 is the location of the upper boundary of the sector for which the heat generation is currently analyzed, and  $Q_{k,y}$  is the heat generated in the cross-section at a length  $y$  metres for phase  $k$ .

To break down Equation 7.50: it has two main arguments, divided by the plus sign: The first argument decreases in value with increasing length and the second argument increases with increasing length — this is a type of interpolation. If  $y = 200$ , the first sector is being analyzed — that is between  $z = 0$  and  $z = 200$  metres — and the idea is the same for all other sectors.

At a length  $z = 0$ , the first argument is  $(200 - 0)/l_{dz} = 1$  while the second is  $1 + (0 - 200)/l_{dz} = 0$ , hence the function takes the value of the first argument  $Q_{k,axi}(y, z) = Q_{k,y}$ . On the other hand, at a length  $z = 200$ , the first argument is  $(200 - 200)/l_{dz} = 0$  while the second is  $1 + (200 - 200)/l_{dz} = 1$  and thus the value of the function is equal to the value of the second argument:  $Q_{k,axi}(y, z) = Q_{k,(y+l_{dz})}$ .

If the length is  $0 < z < 200$ , an interpolation between the two times is taken.

$Q_{k,axi}(y, z)$ , in  $W/m^3$ , is entered as a heat source in each phase of the cable (in COMSOL via the General Source option within the Heat Source domain node); it is also possible to obtain the heat generation within the neutral conductor via the same method.

If the cross-sections are simulated using a distributed parametric sweep, because of the full decoupling of each cross-section it is impossible to obtain  $Q_{k,axi}(y, z)$  during the simulation — the results become available only after all simulations have concluded. To overcome this, the heat generation in the 2D-axisymmetric model may be raised "post-factum", e.g. through looking up the already calculated values of generated heat in each parametric cross-section simulation at specified times  $t$  such that  $0 \leq t \leq 0.1$  seconds. This is achievable in COMSOL via the "withsol" operator. If the value of heat is required at a time that falls between two stored timesteps, the operator uses interpolation.

The 1D heat transfer in fluids model is ran in conjunction with the 2D-axisymmetric model, simulating for the temperature of the coolant.

## Results

The temperature distribution along the cable is shown on Figures 7.9 and 7.10, for three instances in time while the duration of the fault is on-going. The solid lines represent the simulated temperatures along the cable in the 2D-axisymmetric model, the dashed — the values for the temperatures from literature, and the crosses — the maximum phase temperatures in the 2D cross-section model at the corresponding length.

Each phase's temperature increase is predicted in line with literature.

The first phase sees the largest increase due to having the lowest critical current; this is also recognized in [57]. Experiencing the highest initial peak does not contribute greatly to the generated heat in the first phase, as in this case the initial peaks in the other

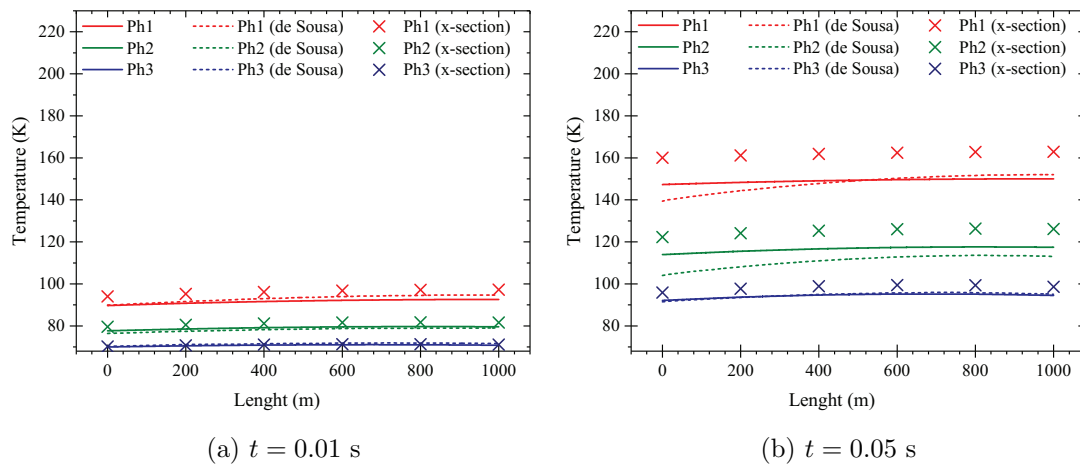


Figure 7.9: The temperature distribution in each phase along the cable length for two times during the fault, taken from the 2D-axisymmetric solution (solid lines) and the 2D-cross-section solution (crosses), compared with the published values from [57] (dashed lines).

two phases are not significantly smaller (in phase three due to its phase delay the initial peak is smaller than the second peak). Another result coming from the lower critical current is that the first phase also experiences the strongest current limitation.

Phase two generates heat faster than the third phase and slower than the first. This holds true from the onset of the fault to its clearing.

The calculated temperature at the time of clearing of the fault is higher than the results presented in literature.

Notably, the expected difference between the phase temperatures at the beginning and at the end of the cable has not materialized. The literature suggests a 10-25 K difference along the length of the cable for phase one, however the simulation shows only 5 K. This temperature difference of 5 K is in line with the difference along each phase, before the onset of the fault, of about 2 K. The result is not affected by the approximation that the current may be simulated within each cross-section without regard to the remaining parts of the cable (running all cross-sections as one model, as opposed to a decoupled parametric sweep, yielded results with negligible change). This shows that a single cross-section may be more than sufficient to simulate fault current in the entire cable, however, this may not be the case for other cable designs or for simulating normal operation.

Otherwise, the difference with calculated temperatures at distance where the temperature from the literature is highest is 1.5%, 4.9%, 1.4% for phases one through three respectively; and at the beginning of the cable is 8.9%, 10.7%, 5.9%.

Another notable result is the visibly higher temperature obtained from the cross-section model when compared to the axisymmetric model.

This is to be expected, since the way the two models handle the area of conducting

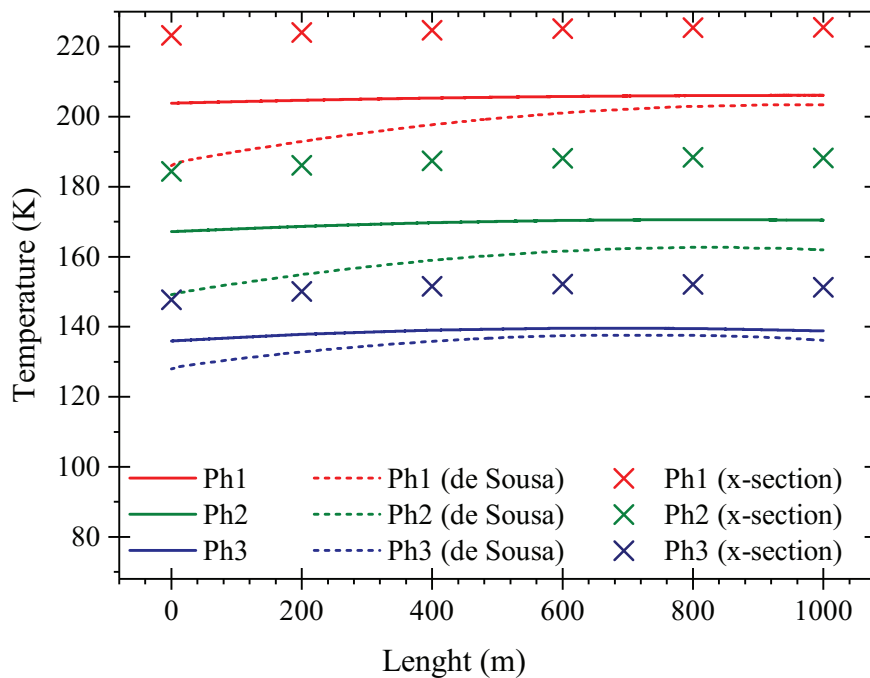


Figure 7.10: The temperature distribution in each phase along the cable length at the time of clearing the fault ( $t = 0.1$  s), taken from the 2D-axisymmetric solution (solid lines) and the 2D-cross-section solution (crosses), compared with the published values from [57] (dashed lines).

material differs. In the cross-section model, each tape is defined and has finite dimensions, while in the axisymmetric model, the conducting material is approximated as a monoblock mixture of silver and HTS taking the shape of a hollow cylinder. As this hollow cylinder is a solid body, its cross-sectional area is larger than the area of individual tapes that, in reality, occupy that space. So, when a certain amount of heat (in Watts) that is generated in the surface area of  $A_{hts}$   $m^2$  is applied on a larger area, for example  $1.5A_{hts}$   $m^2$ , the resulting maximum temperature would be lower in the domain with the larger area.

However, if it is kept in mind that the actual temperature within each phase may be higher than the one predicted by the axisymmetric model, it is a reasonable approximation for the purposes of identifying the cable's recovery time. That is so due to the fact the amount of heat is kept constant throughout the models and therefore the same amount of heat generated in the cross-sectional model will eventually be transferred to the coolant.

## 7.5 Recovery of the AmpaCity cable

After the fault has been cleared, the cable can begin recovery. The temperature of the superconducting material must drop to a value sufficiently below its critical value (100-110 K for first generation materials), while the temperature of the coolant must remain under its boiling value (78 K for liquid nitrogen). To meet this condition it may be

necessary to not allow any current to flow, or an upper value of permissible current may be obtained for which the cable can return to steady-state conditions.

Simulating the recovery process does not require the introduction of physics not already used. Just as in Section 7.3, a 1D heat transfer in fluids model coupled with a 2D-axisymmetric heat transfer in solids model is required. The settings of these physics remain the same as previously, with the exception of the initial conditions, which are of course set to begin the simulation from the results at  $t = 0.1$  s.

The simulation reaches  $t = 8$  hours and a number of steps are taken before that time is reached, in line with the results from [57]. The simulated versus literature temperature of each phase after the fault has been cleared is shown on Figure 7.11. Observing the obtained results (solid lines), the behaviour of the cooling of each phase is as expected. The first phase, being closest to the supply flow, has the highest rate of cooling. This is followed by the third phase. The second phase's position in the middle of the cable, sandwiched between the other phases and surrounding insulation, takes the longest to

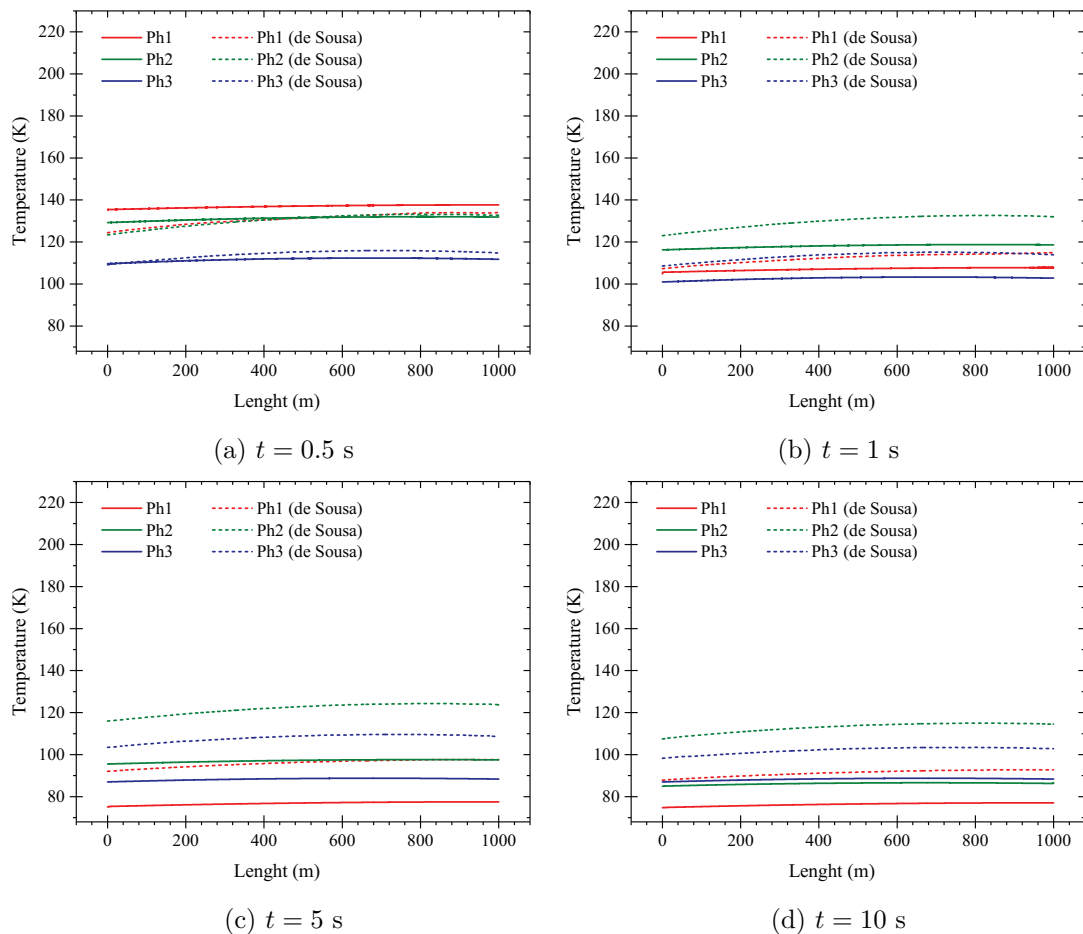


Figure 7.11: The recovery of the temperature, and its distribution, in each phase along the cable length for four times after the fault has been cleared, taken from the 2D-axisymmetric solution (solid lines) and compared with the published values from [57] (dashed lines).



cool down.

The same behaviour can be observed in the results obtained from [57] (dashed lines). However, the rate of cooling of all phases is visibly lower in the literature. This is particularly visible for the second phase which practically does not decrease in temperature between  $t = 0.5$  and  $t = 1$  seconds. Due to PPLP's low thermal conductivity, it would be extremely unlikely for the surrounding insulation to heat up and saturate to the value of the temperature of the second phase in less than one second. This is corroborated in the FEM model. What this observation may suggest is there is a difference between the finite element and finite difference model when it comes down to solving this problem, and that the way space is discretized can be very important. The finite difference model in literature may lump each material layer into a separate 1D approximation, in which case the insulation layers are more likely to saturate in the observed way. The same argument may be used to suggest why all three phases recover slower in [57] than in the simulation.

The literature suggests all phases have returned to below their critical temperature (100 K) at about 20 seconds. The simulation, on the other hand, finds that happens at about 5 seconds and by the tenth second, each phase has comfortably recovered. It must be kept in mind that the temperatures in the 2D-axisymmetric model are lower than the actual temperatures of the cable, as described at the end of Section 7.4.4. Hence, a further study may be necessary to determine the actual recovery of each phase.

Once the phases have returned to a temperature below critical, they may be subjected to current again. The magnitude of that current will dictate whether the cable will quench again or slowly return to steady state temperatures, and if it returns to steady state then how fast it will do so.

### 7.5.1 Very little or no current during recovery

If no current or current considerably smaller than the critical current (such as  $I_t = 283$  A peak or 200 A RMS) is applied, there will be a negligible amount of heat generated (Figure 7.13). This is investigated in [57] and it is discovered the temperature of the cable's liquid nitrogen approaches steady state after around 5 hours, and has practically reached steady state after around 8 hours.

The results are illustrated in Figure 7.12. The predicted temperature distributions via the coupled FEM model strongly resemble the results from literature. Both models agree — at no point does the coolant temperature exceed 77.5 K. What they disagree on are the temperatures at the end of the cable (where supply and return flow join), and at the cable outlet. The modelled temperature decreases somewhat faster than the results from [57], with the difference being comparable to the difference in the steady state results. Notably, by hour 8, the disagreement has completely vanished.

The observed temperature "peak" at the 1000 m point of the coolant between 20 seconds and 3 minutes, as seen on Figure 7.12, is essentially a temperature front. Since phase 1

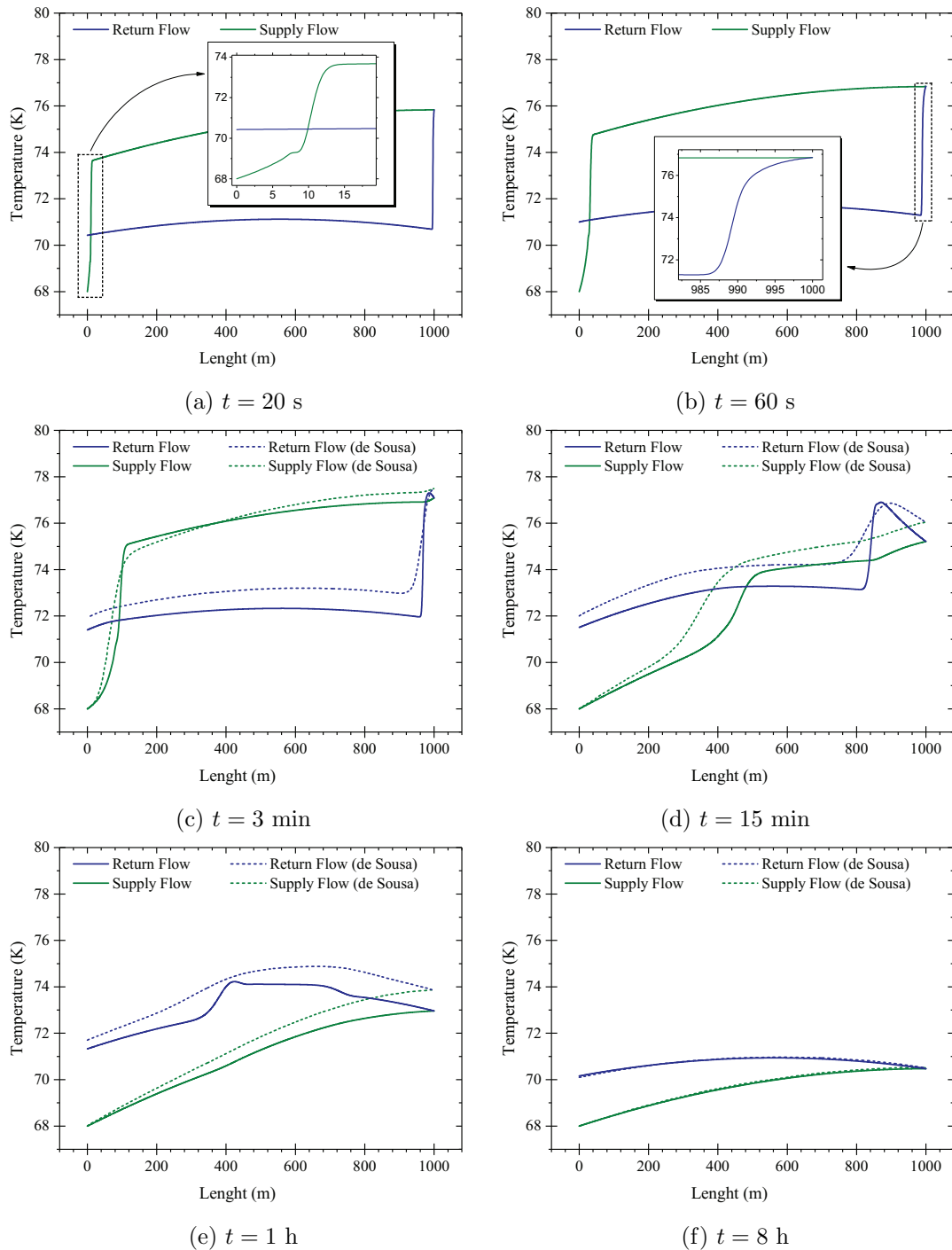


Figure 7.12: The recovery of the temperature, and its distribution, in the coolant along the cable length for six instances in time after the fault has been cleared, taken from the 1D solution (solid lines) and compared with the published values from [57] (dashed lines).

is a lot closer to the former (and the supply flow) than phase 3 is to the annular (return flow), the supply flow will experience temperature rise quickly along its entire length almost immediately. At the 1000 m point, the mass flowing in the supply tube turns and joins the return flow. Once returning, the velocity of the fluid is standing at 0.26

m/s (calculated from the constant mass flow and the geometry of the tubular channel). So after 60 seconds, the hot fluid will have moved only 15.6 meters, which is consistent with the inset graph in Figure 7.12b. Considering that the hot fluid meets a colder cable wall along those 15 or so meters, some of the heat is returned to the cable.

A similar reasoning can be used successfully for the "slope" seen between 0-14 m for the supply flow in Figure 7.12a. Analysis of the heat flux at the boundary between the cable and the supply flow shows that the highest value of heat flux is seen immediately after the fault is cleared (at 0.1 s). Afterwards the heat flux decreases because the source of heat is removed while fresh coolant comes through the supply flow which removes more heat from the cable with each passing second. This allows for the temperature increase in the supply flow to develop a temperature front. For the coolant in the supply channel, the mass velocity is 0.61 m/s and so it is capable of covering the 14 m in 20-23 seconds (the difference between the velocities of the supply and return flows is due to the different geometries of the each channel and the constant mass flow).

All differences are directly linked to the rate of cooling of each phase (Figure 7.11), and it was discussed above that the 2D-axisymmetric FEM model achieves a faster cooling rate. This, naturally, projects onto the temperature profile of the liquid nitrogen.

### 7.5.2 Large current during recovery

An investigation is performed to see how the cable's operation will be affected during recovery if the applied current is non-negligible. Four RMS transport current values are selected: 900 A, 1500 A, 2200 A and 3000 A. These correspond to 0.29, 0.48, 0.70 and 0.96 of phase one's 4400 A peak critical current, respectively. The 2D cross-section model is then used to estimate the losses in W/m in each phase while under isothermal conditions for temperatures from 75 K to 97.5 K with a step of 2.5 K. An interpolated

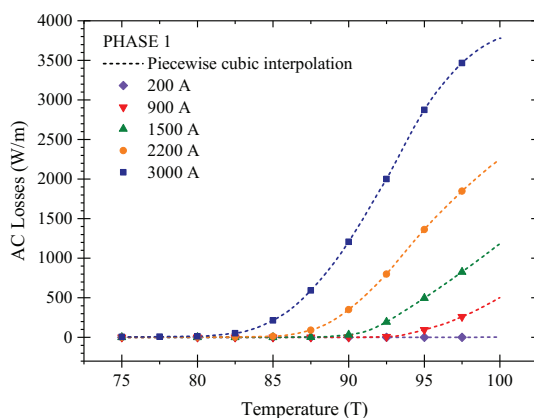


Figure 7.13: The estimated losses for a number of transport RMS currents for phase one of the AmpaCity cable, against temperature.

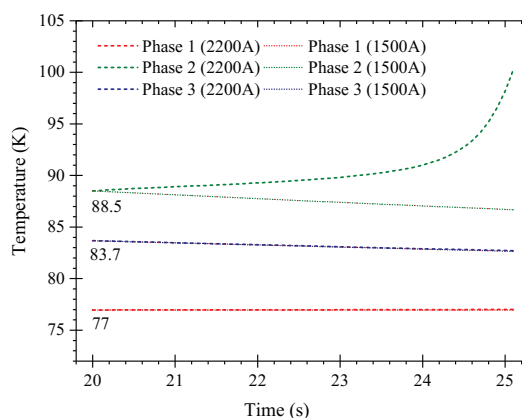


Figure 7.14: A demonstration of how the second phase drives the re-quench. Current is applied at 20 seconds.

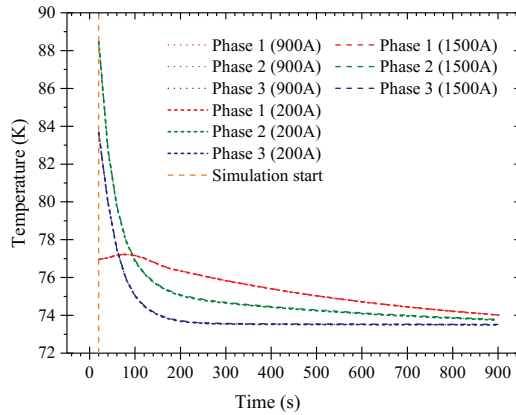


Figure 7.15: The temperature of each phase for 900 s across several values for transport current. Current is applied at 20 seconds.

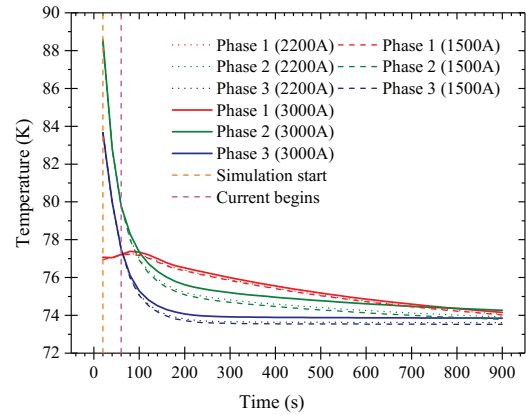


Figure 7.16: The temperature of each phase for 900 s across several values for transport current. Current is applied at 60 seconds.

function can be extracted from these results, for the purposes of obtaining the value of losses against temperature, for each phase for a given transport current. Such an approximation for the AmpaCity cable from [52, 57] is displayed in Figure 7.13, where the datapoints are transformed into a continuous function through a piecewise cubic interpolation (COMSOL Interpolation function).

The computationally expensive simulation of the  $H$ -formulation for periods longer than several cycles can now be avoided; the remaining simulation can be entirely performed using the 2D cross-section Heat Transfer model. Only one cross-section needs to be simulated as it was shown the longitudinal change in temperature of each phase was insignificant in the FEM model — the cross-section at 600 metres was chosen as it is closest to the peak temperature from both literature and this work.

If a review of the coolant recovery is needed, it can be achieved similarly to previous sections by applying the same amount of generated heat in the axisymmetric model as in the cross-section model.

It is very important to note that if the axisymmetric model is allowed to generate its own heat, the final results may inaccurately show a current may run without re- quenching the cable. This is discussed in the previous sections — it is because the axisymmetric model underestimates the maximum achievable temperature due to the difference between conductor areas.

Let current be applied at  $t = 20$  s. 900 A and 1500 A may run effectively without a noticeable change in temperature — thus, in practice they do not affect the recovery of the cable (Figure 7.15). However, at the next simulated value (2200 A), the heat generated becomes large enough to throw off the thermal balance and quench the superconductor. A closer look at the temperature rise shows that the rise is driven by the second (middle) phase, because it has the highest temperature. This can be seen

in Figure 7.14 — portrayed are the temperature recoveries during a 1500 A and 2200 A. The heat generated in phase two of the 2200 A simulation increases the temperature steadily.

The actual upper limit of current that would not re-quench the superconductor is between 1500 A and 2200 A, and its value may be determined more precisely if necessary.

Let current be applied at  $t = 60$  s. At that point in time, the temperature of each layer has dropped sufficiently and no re-quench occurs even with the highest value of 3000 A RMS. However, as illustrated in Figure 7.16, the introduction of the 3000 A current increases the temperature in each layer such that the recovery takes longer than when a lower current value is applied.

## 7.6 Summary

This Chapter discussed the finite element multiphysics modelling of a three-phase cable in the Triax configuration. Using existing publications in literature, it was shown that a FEM model is viable and may be constructed robustly using existing COMSOL tools. No external additions are necessary. Moreover, the simulation may be performed over a reasonable amount of time using low computational resources when certain approximations are exploited.

### Contributions

- Constructing a multiphysics model through a novel combination of existing modules and techniques as well as implementing new techniques.
- Estimating the cable's total resistance, per phase, at any given point during a transient fault simulation in a finite element environment. Particularly when a homogenized model for first generation superconductors is used.
- Achieving a sufficiently accurate simulation of both cable and coolant using a finite element model in a reasonable amount of time, through the application of moderate approximations.
- The majority of this Chapter has been submitted for review in IEEE Transactions on Applied Superconductivity under the title "Efficient multiphysics finite element simulation of a transient fault in a first generation HTS power cable".

## Chapter 8

# Conclusion

This thesis follows through the necessary steps to construct a full-fledged and efficient multiphysics model.

Firstly, an  $H$ -formulation was built in COMSOL. Published literature provides the information required to build that formulation, which can be used to simulate an individual tape. The main obstacle in first generation tapes is the large number of filaments, and it was shown that it can be overcome by adapting an existing technique — the homogenized multifilamentary domain — from other areas of modelling into the area of AC power loss estimation. The technique uses one homogeneous domain to represent all superconducting filaments and essentially takes the shape of the multifilamentary region, though it may be approximated as an ellipse. Overall, the homogenization technique was proven to work with more than one tape and just as well as a fully multifilamentary model, yet being considerably faster and easier to construct.

Once a tape can be robustly simulated, the model can be scaled up to systems of tapes and cables. Here, to achieve a balanced current distribution in a power cable, each layer must be twisted at a varying angle which also introduces a geometry that is inherently 3D. In order to ensure the model is computationally efficient, 3D modelling of superconductors is not admissible. Using simple mathematical adjustments to account for the twist of each layer can allow it to be approximated in a simple 2D cross-section. The results of that research show the widely known rule claiming layer twist requires 3D modelling [15] may be bypassed — most common angles of twist used in power cables could be simulated accurately, yet with increasing angle the inaccuracy of the result also increases. This also expands on the result in [81] which shows the longitudinal magnetic field may sometimes be neglected. Models built with this method are easier and faster to construct and simulate than a corresponding 3D model, which can have significant implications when the level of detail a FEM model can provide is desirable but has previously been impractical to obtain.

Another question is, given the different twist angle of each layer, at what length along a

multi-layer cable should its cross-section be taken for simulation in order to achieve an accurate 2D cross-sectional model. This question was also answered.

The last and most important stage of this thesis is the simulation of the response of the power cable when a transient fault current has flown through it and its recovery once the fault has been cleared. Using the knowledge accumulated in the previous two stages of the thesis allows for the construction of a 2D electromagnetic model of the AmpaCity cable [52, 53, 57]. Heat transfer within the cable and the coolant must accompany the electromagnetic model, and are introduced to the model through using existing COMSOL physics and component couplings such that the entire model can run from steady-state initialization before the fault to full recovery. Estimating the effective resistance of the cable from a 2D cross-section model so that the fault current limitation may be calculated accurately while using the homogenization technique and the twisted-tape approximation is an important challenge that has been overcome. Other important questions that have been answered are how to achieve in practice the above mentioned coupling between the physics and how to split the model in a way that may be readily simulated in a distributed parametric sweep on a computing cluster.

The response and recovery of the AmpaCity cable [57] was modelled successfully and the results were compared with literature; additionally the recovery of the cable under varying transport current was investigated. The simulation time of the entire model was within 1 day when a computing cluster was used and less than 3 days otherwise, which is objectively acceptable. The same model may easily be used to simulate both steady-state and transient conditions.

The main contributions of this thesis may be summarised as follows:

- Showing the Kim-Anderson approximation may introduce an error, which is noticeable in DC applied fields, and that using an interpolation for the critical current dependence on the magnetic field will result in more accurate simulations.
- Reintroducing a domain homogenization method for the estimation of AC power loss of multifilamentary tapes with fully-coupled filaments, as well as cables built with such.
- A method for approximating the losses of tapes wound over a circular former, taking into account the twist angle, is developed and verified.
- The introduction and verification of a technique for the estimation of AC power loss of multi-layer power cables with layers with varying twist pitches in a purely 2D cross-sectional model.
- Achieving in COMSOL a smooth and continuous split of the magnetic field into parallel and perpendicular components over the full rotation of a cross-section, in order to effectively take into account the anisotropy of the tape.

- Constructing and simulating the AC power loss in a single-phase two-layer power cable in 3D for a range of transport currents including above critical.
- Constructing a complex multiphysics model in COMSOL through a novel combination of existing modules and techniques as well as implementing new ones.
- Estimating the cable's total resistance, per phase, at any given point in time during a transient fault simulation in a finite element environment (particularly with a homogenized multifilamentary domain) which allows for the live calculation of the fault current limiting ability of the cable.
- Achieving a sufficiently accurate simulation of both cable and coolant using a finite element model in a reasonable amount of time, through the application of moderate approximations based on modelling experience.

## Publications

The majority of Chapter 5, in the shape of a full length research article, has been accepted in *Physica C: Superconductivity and its Applications* [104]. An oral presentation at the *6th International Workshop on Numerical Modelling of High Temperature Superconductors*, 25<sup>th</sup>-29<sup>th</sup> June 2018, addressed one part of the publication, and the other part was presented as a poster at the *Applied Superconductivity Conference*, 29<sup>th</sup> October to 2<sup>nd</sup> November 2018.

The research described in Chapter 6 was be presented in poster format at the *14th European Conference on Applied Superconductivity*, 1<sup>st</sup>—5<sup>th</sup> September 2019. A conference paper is published at the *IOP Conference Series* under the title "*2D finite element modelling of the AC transport power loss in multi-layer Bi-2223 cables*" [111].

A full length research article under the name "*Efficient multiphysics finite element simulation of a transient fault in a first generation HTS power cable*", covering Chapter 7, is under review at the *IEEE Transactions on Applied Superconductivity*.

## Future work

- This thesis as well as models from literature assume the coolant to be a 1D body, which may not necessarily be an accurate approximation in all cases and applications — a temperature rise is not instantaneous across the entire channel width. It would be interesting to introduce complete fluid flow physics together with heat transfer in fluids, in the coolant model. A particular challenge observed while working on this thesis is that low viscosity materials can cause very long simulation times or outright numerical instability in COMSOL.



- The extension of the knowledge from Chapters 6 and 7 may be applied to the simulation of second generation tapes and cables, which may bear an immediate application in the modelling of power cables.
- The element order of the physics in the models, particularly in the  $H$ -formulation, influences the accuracy of the results as well as the simulation time. Its influence on the multiphysics model at hand may be investigated in the future.
- The circuit equation for the transient fault current estimation assumes the mutual inductances of each phase are negligible when compared to the grid inductance and the rise of the resistance in the superconductor. Future work may explore whether the addition of mutual inductances to the circuit equations of each phase may provide different results.





# References

- [1] “Energy network costs: transparent and fair?” House of Commons Energy and Climate Change Committee, Report, 2015. [Online]. Available: <https://publications.parliament.uk/pa/cm201415/cmselect/cmenergy/386/386.pdf>
- [2] “Digest of UK Energy Statistics, Chapter 5: Electricity,” UK Department for Business, Energy and Industrial Strategy, Report, 2019. [Online]. Available: [https://assets.publishing.service.gov.uk/government/uploads/system/uploads/attachment\\_data/file/820708/Chapter\\_5.pdf](https://assets.publishing.service.gov.uk/government/uploads/system/uploads/attachment_data/file/820708/Chapter_5.pdf)
- [3] “UK Power Networks’ Distribution Losses Strategy,” UK Power Networks, Report, 2019. [Online]. Available: <https://www.ukpowernetworks.co.uk/losses/static/pdfs/uk-power-networks-distribution-losses-strategy-july-2019.c520b6d.pdf>
- [4] C. Rey, *Superconductors in the Power Grid: Materials and Applications*, ser. Woodhead Publishing Series in Energy: Number 65. Elsevier Ltd., 2015.
- [5] D. I. Doukas, “Superconducting transmission systems: Review, classification, and technology readiness assessment,” *IEEE Transactions on Applied Superconductivity*, vol. 29, no. 5, pp. 1–5, 2019.
- [6] D. v. Delft, “History and significance of the discovery of superconductivity by Kamerlingh Onnes in 1911,” *Physica C: Superconductivity*, vol. 479, pp. 30–35, 2012.
- [7] M. Sjoström, “Hysteresis modelling of high temperature superconductors,” Thesis, Swiss Federal Institute of Technology Lausanne, 2001.
- [8] M. Cyrot, “Ginzburg-Landau theory for superconductors,” *Reports on Progress in Physics*, vol. 36, no. 2, p. 103, 1973.
- [9] A. M. Forrest, “Meissner and Ochsenfeld revisited,” *European Journal of Physics*, vol. 4, no. 2, p. 117, 1983.
- [10] J. Bardeen, L. N. Cooper, and J. R. Schrieffer, “Theory of superconductivity,” *Phys. Rev.*, vol. 108, pp. 1175–1204, Dec 1957.
- [11] F. Grilli, “Numerical modelling of high temperature superconducting tapes and cables,” Thesis, Swiss Federal Institute of Technology Lausanne, 2003.
- [12] S. Stavrev, “Modelling of high temperature superconductors for AC power applications,” Thesis, Swiss Federal Institute of Technology Lausanne, 2002.
- [13] A. A. Abrikosov, “On the magnetic properties of superconductors of the second group,” *JETP*, vol. 5, no. 6, p. 1174, 1957.
- [14] Y. Wang, *Fundamental Elements of Applied Superconductivity in Electrical Engineering*. John Wiley & Sons Singapore Pte. Ltd., 2013.
- [15] F. Grilli, E. Pardo, A. Stenvall, D. N. Nguyen, Y. Weijia, and F. Gomory, “Computation of losses in HTS under the action of varying magnetic fields and currents,” *IEEE Transactions on Applied Superconductivity*, vol. 24, no. 1, pp. 78–110, 2014.
- [16] P. W. Anderson and Y. B. Kim, “Hard superconductivity: Theory of the motion of Abrikosov flux lines,” *Rev. Mod. Phys.*, vol. 36, pp. 39–43, Jan 1964.

- [17] M. V. Feigel'man, V. B. Geshkenbein, A. I. Larkin, and V. M. Vinokur, "Theory of collective flux creep," *Phys. Rev. Lett.*, vol. 63, pp. 2303–2306, Nov 1989.
- [18] J. Bardeen and M. J. Stephen, "Theory of the motion of vortices in superconductors," *Phys. Rev.*, vol. 140, pp. A1197–A1207, Nov 1965.
- [19] C. P. Bean, "Magnetization of hard superconductors," *Phys. Rev. Lett.*, vol. 8, pp. 250–253, Mar 1962.
- [20] M. K. Wu, J. R. Ashburn, C. J. Torng, and et al., "Superconductivity at 93 K in a new mixed-phase Yb-Ba-Cu-O compound system at ambient pressure," *Phys Rev Lett*, vol. 58, no. 9, pp. 908–910, 1987.
- [21] P. W. G. J. L. Tallon, R. G. Buckley and et al., "High-Tc superconducting phases in the series  $\text{Bi}_{2.1}(\text{Ca}, \text{Sr})_n\text{ICu}_n\text{O}_{2n+4+\delta}$ ," *Nature*, vol. 333, 1988.
- [22] M. F. H. Maeda, Y. Tanaka and T. Asano, "A new high-Tc oxide superconductor without a rare earth element," *J. Appt. Phys. Pt. 2*, no. 27, pp. 209–10, 1988.
- [23] R. M. Scanlan, A. P. Malozemoff, and D. C. Larbalestier, "Superconducting materials for large scale applications," *Proceedings of the IEEE*, vol. 92, no. 10, pp. 1639–1654, 2004.
- [24] M. D. Brown, J. Jiang, C. Tarantini, D. Abraimov, G. Bradford, J. Jaroszynski, E. E. Hellstrom, and D. C. Larbalestier, "Prediction of the JC (B) behavior of Bi-2212 wires at high field," *IEEE Transactions on Applied Superconductivity*, vol. 29, no. 5, pp. 1–4, 2019.
- [25] T. Arndt, A. Aubele, B. Fischer, H. Krauth, B. Sailer, and A. Szulczyk, "Bi-2223 tapes for applications at high temperatures and/or high fields—designs, long length processing and properties," *Physica C: Superconductivity*, 2002.
- [26] N. H. M. Noe and et al., "Common characteristics and emerging test techniques for high temperature superconducting power equipment," CIGRE, Report, 2015.
- [27] S. Kobayashi, K. Yamazaki, T. Kato, and et al., "Controlled over-pressure sintering process of Bi-2223 wires," *Physica C: Superconductivity and its Applications*, vol. 426–431, Part 2, pp. 1132–1137, 2005.
- [28] P. Li, L. Zhao, T. M. Qu, X. C. Wang, and Z. Han, "Fabrication and study of thin Bi-2223 round wires," *Physica C: Superconductivity and its Applications*, vol. 463–465, pp. 837–840, 2007.
- [29] W. Martienssen and H. Warlimont, *Springer Handbook of Condensed Matter and Materials Data*. Berlin: Springer, 2005.
- [30] G. Villard, F. Legendre, S. Poissonnet, P. Régnier, C. Bifulco, and G. Giunchi, "Enhancement of the critical current density of Bi-2212 electrodeposited tapes through microstructure control," *Physica C: Superconductivity*, vol. 341, pp. 2007–2008, 2000.
- [31] N. Hu, K. Cao, D. Wang, M. Song, D. Miyagi, M. Tsuda, and T. Hamajima, "Transient thermal analysis of a tri-axial HTS cable on fault current condition," *Physica C: Superconductivity*, vol. 494, pp. 276–279, 2013.
- [32] H. Sun-Kyoung, K. Sung-Kyu, K. Jin-Geun, P. Minwon, Y. In-Keun, L. Sangjin, S. Kideok, and A. R. Kim, "Transient characteristic analysis of a tri-axial HTS power cable using PSCAD/EMTDC," *IEEE Transactions on Applied Superconductivity*, vol. 23, no. 3, pp. 5 400 104–5 400 104, 2013.
- [33] N. Hu, M. Toda, T. Watanabe, M. Tsuda, and T. Hamajima, "Recovery time analysis in a tri-axial HTS cable after an over-current fault," *Physica C: Superconductivity and its Applications*, vol. 471, no. 21–22, pp. 1295–1299, 2011.
- [34] N. Hu, M. Toda, A. N. Ozcivan, T. Yagai, M. Tsuda, and T. Hamajima, "Fault current analysis in a tri-axial HTS cable," *IEEE Transactions on Applied Superconductivity*, vol. 20, no. 3, pp. 1288–1291, 2010.

- [35] Z. Zhuonan, Z. Jiahui, L. Huifeng, Q. Ming, L. Zhenming, D. Kaizhong, and W. Yasen, "Magnetic-thermal coupling analysis of the cold dielectric high temperature superconducting cable," *IEEE Transactions on Applied Superconductivity*, vol. 23, no. 3, pp. 5 400 404–5 400 404, 2013.
- [36] B. Shu, F. M. Wang, Z. Y. Liu, J. T. Li, Z. J. Zhao, J. H. Li, and Z. Liang, "Fault analysis of HTS power transmission cables," in *2013 IEEE International Conference on Applied Superconductivity and Electromagnetic Devices*, 2013, Conference Proceedings, pp. 543–545.
- [37] J. Li, Z. Zhao, B. Shu, X. Han, X. Ma, B. Bian, J. Li, and Z. Liang, "Fault analysis for 110 kV HTS power cables," *IEEE Transactions on Applied Superconductivity*, vol. 24, no. 5, pp. 1–5, 2014.
- [38] J. Fang, H. F. Li, J. H. Zhu, Z. N. Zhou, Y. X. Li, Z. Shen, D. L. Dong, T. Yu, Z. M. Li, and M. Qiu, "Numerical analysis of the stability of HTS power cable under fault current considering the gaps in the cable," *Physica C: Superconductivity*, vol. 494, pp. 319–323, 2013.
- [39] Z. M. Li, W. Liu, J. H. Zhu, M. Qiu, X. D. Zheng, and J. Fang, "Temperature and current distribution of high temperature superconducting cable itself under large fault current," in *2015 IEEE International Conference on Applied Superconductivity and Electromagnetic Devices (ASEMD)*, 2015, Conference Proceedings, pp. 151–152.
- [40] J. Zhu, H. Li, M. Qiu, J. Fang, X. Chen, and W. Yuan, "Magneto-thermal coupling modeling for the stability analysis of a 110 kV/3 kA high temperature superconducting cable under fault current conditions," *Journal of Superconductivity and Novel Magnetism*, vol. 28, no. 2, pp. 607–613, 2014.
- [41] Z. Y. Li, D. Y. Hu, Z. H. Yao, Y. W. Wang, Z. Y. Hong, K. Ryu, Y. H. Ma, and H. S. Yang, "Inductance evaluation of a 22.9 kV/50 MVA HTS cable with shield by electrical method," in *2015 IEEE International Conference on Applied Superconductivity and Electromagnetic Devices (ASEMD)*, Conference Proceedings, pp. 568–570.
- [42] L. Yin, X. F. Ma, X. N. Li, K. Zhang, X. D. Zheng, J. Fang, J. H. Zhu, and M. Qiu, "Analysis of high temperature superconducting cable model under fault current," in *2015 IEEE International Conference on Applied Superconductivity and Electromagnetic Devices (ASEMD)*, 2015, Conference Proceedings, pp. 266–267.
- [43] Y. Sato, K. Agatsuma, X. Wang, and A. Ishiyama, "Temperature and pressure simulation of a high-temperature superconducting cable cooled by subcooled LN<sub>2</sub> with fault current," *IEEE Transactions on Applied Superconductivity*, vol. 25, no. 3, pp. 1–5, 2015.
- [44] T. Yasui, Y. Sato, K. Agatsuma, A. Ishiyama, X. Wang, M. Ohya, T. Masuda, and S. Honjo, "Temperature and pressure simulation of a 1.5-km HTS power cable cooled by subcooled LN<sub>2</sub> with a fault current," *IEEE Transactions on Applied Superconductivity*, vol. 26, no. 3, pp. 1–5, 2016.
- [45] Y. Yokoo, T. Yasui, N. Takeda, K. Agatsuma, A. Ishiyama, X. Wang, M. Yagi, and T. Takagi, "Temperature simulation of a 20 m HTS power model cable system in a fault current for 275 kV transmission lines," *IEEE Transactions on Applied Superconductivity*, vol. 27, no. 4, pp. 1–6, 2017.
- [46] Y. Yokoo, N. Takeda, D. Horita, K. Agatsuma, A. Ishiyama, X. Wang, T. Takagi, and M. Yagi, "Safety verification of a 275-kV HTS cable system under short-circuit current accidents," *IEEE Transactions on Applied Superconductivity*, vol. 28, no. 4, pp. 1–5, 2018.
- [47] N. Takeda, T. Yasui, Y. Yokoo, K. Agatsuma, A. Ishiyama, X. Wang, T. Masuda, T. Morimura, and T. Mimura, "Temperature and pressure simulations of 66 kV 40 m HTS cable system in short-circuit current accidents compared with experimental results," *IEEE Transactions on Applied Superconductivity*, vol. 27, no. 4, pp. 1–5, 2017.
- [48] T. Yasui, N. Takeda, Y. Yokoo, K. Agatsuma, A. Ishiyama, X. Wang, T. Masuda, T. Morimura, and T. Mimura, "Temperature and pressure distribution simulations of 3 km long high-temperature superconducting power cable system with fault current for 66 kV class transmission lines," *IEEE Transactions on Applied Superconductivity*, vol. 27, no. 4, pp. 1–5, 2017.

- [49] X. Wang, A. Ishiyama, M. Ohya, and N. Fujiwara, "Over-current characteristics of 66-kV RE123 HTS power cable," *IEEE Transactions on Applied Superconductivity*, vol. 21, no. 3, pp. 1013–1016, 2011.
- [50] X. Wang, H. Ueda, A. Ishiyama, M. Yagi, S. Mukoyama, M. Ohya, T. Masuda, N. Kashima, S. Nagaya, and Y. Shiohara, "Over-current characteristics of a 20-m-long YBCO model cable," *IEEE Transactions on Applied Superconductivity*, vol. 19, no. 3, pp. 1722–1726, 2009.
- [51] A. Ishiyama, X. Wang, H. Ueda, T. Uryu, M. Yagi, and N. Fujiwara, "Over-current characteristics of 275-kV class YBCO power cable," *IEEE Transactions on Applied Superconductivity*, vol. 21, no. 3, pp. 1017–1020, 2011.
- [52] E. Shabagin, C. Heidt, S. Strauß, and S. Grohmann, "Modelling of 3D temperature profiles and pressure drop in concentric three-phase HTS power cables," *Cryogenics*, vol. 81, pp. 24–32, 2017.
- [53] M. Stemmler, F. Merschel, M. Noe, and A. Hobl, "AmpaCity - advanced superconducting medium voltage system for urban area power supply," in *2014 IEEE PES T&D Conference and Exposition*, 2014, Conference Proceedings, pp. 1–5.
- [54] D. Miyagi, R. Sakakibara, Y. Shinozaki, M. Tsuda, and T. Hamajima, "Suitable cable structure of HTS triaxial cable cooled by counter flow cooling method for long-distance power transmission," *IEEE Transactions on Applied Superconductivity*, vol. 28, no. 4, pp. 1–5, 2018.
- [55] K. Adachi, K. Shiohara, H. Sugane, T. Kitamura, N. Mido, T. Hasegawa, M. Konno, and M. Iwakuma, "Sudden short-circuit test of 22kv ybco triaxial superconducting cable," *IEEE Transactions on Applied Superconductivity*, pp. 1–1, 2018.
- [56] W. T. B. d. Sousa, D. Kottonau, J. Bock, and M. Noe, "Investigation of a concentric three-phase HTS cable connected to an SFCL device," *IEEE Transactions on Applied Superconductivity*, vol. 28, no. 4, pp. 1–5, 2018.
- [57] W. T. Batista de Sousa, D. Kottonau, and M. Noe, "Transient simulation and recovery time of a three-phase concentric HTS cable," *IEEE Transactions on Applied Superconductivity*, vol. 29, no. 5, pp. 1–5, 2019.
- [58] S. Fu, M. Qiu, J. Zhu, H. Zhang, J. Gong, X. Zhao, W. Yuan, and J. Guo, "Numerical study on AC loss properties of HTS cable consisting of YBCO coated conductor for HTS power devices," *IEEE Transactions on Applied Superconductivity*, vol. 28, no. 4, pp. 1–5, 2018.
- [59] S. Fetisov, V. Zubko, S. Zanev, A. A. Nosov, and V. S. Vysotsky, "Numerical simulation and cold test of a compact 2G HTS power cable," *IEEE Transactions on Applied Superconductivity*, pp. 1–1, 2018.
- [60] W. Ta, T. Shao, and Y. Gao, "Comparison study of cable geometries and superconducting tape layouts for high-temperature superconductor cables," *Cryogenics*, vol. 91, pp. 96–102, 2018.
- [61] W. Ta and Y. Gao, "Numerical simulation of the electro-thermo-mechanical behaviors of a high-temperature superconducting cable," *Composite Structures*, vol. 192, pp. 616–625, 2018.
- [62] S. Zhang, X. Ma, L. Cui, G. Liu, H. Zheng, Y. Huang, J. Feng, C. Li, and P. Zhang, "Improving transport properties of Bi-2223 superconducting tapes with the optimization of packing atmosphere," *IEEE Transactions on Applied Superconductivity*, vol. 30, no. 3, pp. 1–8, 2020.
- [63] M. Stemmler, F. Merschel, M. Noe, and A. Hobl, "AmpaCity - installation of advanced superconducting 10 kV system in city center replaces conventional 110 kV cables," in *2013 IEEE International Conference on Applied Superconductivity and Electromagnetic Devices*, 2013, Conference Proceedings, pp. 323–326.
- [64] J. F. Maguire, F. Schmidt, S. Bratt, T. E. Welsh, J. Yuan, A. Allais, and F. Hamber, "Development and demonstration of a HTS power cable to operate in the long island power authority transmission grid," *IEEE Transactions on Applied Superconductivity*, vol. 17, no. 2, pp. 2034–2037, 2007.
- [65] S. Stavrev, "Modelling of high temperature superconductors for AC power applications," PhD Thesis, Swiss Federal Institute of Technology Lausanne, 2002.

- [66] S. Stavrev, B. Dutoit, and N. Nibbio, "Geometry considerations for use of Bi-2223/Ag tapes and wires with different models of  $J_c(B)$ ," *IEEE Transactions on Applied Superconductivity*, vol. 12, no. 3, pp. 1857–1865, 2002.
- [67] S. Stavrev, B. Dutoit, N. Nibbio, and L. L. Lay, "Eddy current self-field loss in Bi-2223 tapes with AC transport current," *Physica C: Superconductivity*, vol. 307, no. 1, pp. 105–116, 1998.
- [68] S. Choi, W. Nah, J. H. Kim, J. Joo, Y. H. Jo, and K. W. Ryu, "AC transport current loss of horizontally attached Bi-2223/Ag tapes," *IEEE Transactions on Applied Superconductivity*, vol. 14, no. 2, pp. 1894–1897, 2004.
- [69] K. Kajikawa, D. Nakamura, T. Hayashi, and K. Funaki, "Numerical evaluation of AC loss property in Bi-2223 tapes affected by multifilament structure," *IEEE Transactions on Applied Superconductivity*, vol. 17, no. 2, pp. 2410–2413, 2007.
- [70] Y. H. Ma, Z. Y. Li, K. Ryu, S. H. Sohn, and S. D. Hwang, "Influence of transport mode on AC loss characteristics of a Bi-2223 tape in a multi-tape conductor," *IEEE Transactions on Applied Superconductivity*, vol. 18, no. 2, pp. 725–728, 2008.
- [71] T. Hayashi, K. Kajikawa, M. Iwakuma, and K. Funaki, "Numerical calculations of AC losses in parallel tape conductors with fixed share of transport current in external magnetic field," *Physica C: Superconductivity and its Applications*, vol. 426–431, pp. 1328–1332, 2005.
- [72] F. Gömöry, J. Šouc, E. Seiler, M. Vojenčiak, and X. Granados, "Modification of critical current in HTSC tape conductors by a ferromagnetic layer," *Journal of Physics: Conference Series*, vol. 97, p. 012096, 2008.
- [73] N. Amemiya, S. ichi Murasawa, N. Banno, and K. Miyamoto, "Numerical modelings of superconducting wires for AC loss calculations," *Physica C: Superconductivity*, vol. 310, no. 1–4, pp. 16 – 29, 1998.
- [74] S. Honjo, N. Hobara, Y. Takahashi, H. Hashimoto, K. Narita, and T. Yamada, "Efficient finite element analysis of electromagnetic properties in multi-layer superconducting power cables," *IEEE Transactions on Applied Superconductivity*, vol. 13, no. 2, pp. 1894–1897, 2003.
- [75] J. Zhao, Y. Li, and Y. Gao, "3D simulation of AC loss in a twisted multi-filamentary superconducting wire," *Cryogenics*, vol. 84, pp. 60–68, 2017.
- [76] N. Amemiya, N. Enomoto, and S. Shirai, "FEM analysis of AC loss in twisted Bi-2223 multi-filamentary tapes carrying AC transport current in AC transverse magnetic field with arbitrary orientation," *IEEE Transactions on Applied Superconductivity*, vol. 14, no. 2, pp. 782–785, 2004.
- [77] A. Stenvall, M. Siahraang, F. Grilli, and F. Sirois, "Computation of self-field hysteresis losses in conductors with helicoidal structure using a 2D finite element method," *Superconductor Science and Technology*, vol. 26, no. 4, p. 045011, 2013.
- [78] A. Kameni, L. Makong, F. Bouillault, and P. J. Masson, "Reduced model to compute AC losses of twisted multifilamentary superconductors," *IEEE Transactions on Applied Superconductivity*, vol. 29, no. 7, pp. 1–6, 2019.
- [79] T. Nakamura, H. Kanzaki, K. Higashikawa, T. Hoshino, and I. Muta, "Analysis of shielding layers in HTS cable taking account of spiral structure," *IEEE Transactions on Applied Superconductivity*, vol. 15, no. 2, pp. 1747–1750, 2005.
- [80] F. Grilli, "Numerical modeling of HTS applications," *IEEE Transactions on Applied Superconductivity*, vol. 26, no. 3, pp. 1–8, 2016.
- [81] K. Takeuchi, N. Amemiya, T. Nakamura, O. Maruyama, and T. Ohkuma, "Model for electromagnetic field analysis of superconducting power transmission cable comprising spiraled coated conductors," *Superconductor Science and Technology*, vol. 24, no. 11, p. 119501, 2011.
- [82] J. Rhyner, "Magnetic properties and AC losses of superconductors with power law current — voltage characteristics," *Physica C: Superconductivity*, vol. 212, no. 3, pp. 292–300, 1993.



- [83] N. Nibbio, S. Stavrev, and B. Dutoit, "Finite element method simulation of AC loss in HTS tapes with B-dependent E-J power law," *IEEE Transactions on Applied Superconductivity*, vol. 11, no. 1, pp. 2631–2634, 2001.
- [84] F. Gömöry, J. Šouc, M. Vojenčiak, and B. Klinčok, "Phenomenological description of flux pinning in non-uniform high-temperature superconductors in magnetic fields lower than the self-field," *Superconductor Science and Technology*, vol. 20, no. 9, pp. S271–S277, 2007.
- [85] J. Duron, F. Grilli, B. Dutoit, and S. Stavrev, "Modelling the E–J relation of high-T<sub>c</sub> superconductors in an arbitrary current range," *Physica C: Superconductivity*, vol. 401, no. 1-4, pp. 231–235, 2004.
- [86] Y. B. Kim, C. F. Hempstead, and A. R. Strnad, "Critical persistent currents in hard superconductors," *Physical Review Letters*, vol. 9, no. 7, pp. 306–309, 1962.
- [87] P. W. Anderson, "Theory of flux creep in hard superconductors," *Physical Review Letters*, vol. 9, no. 7, pp. 309–311, 1962.
- [88] B. Dutoit, M. Sjostrom, and S. Stavrev, "Bi(2223)/Ag sheathed tape I<sub>c</sub> and exponent n characterization and modelling under DC applied magnetic field," *IEEE Transactions on Applied Superconductivity*, vol. 9, no. 2, pp. 809–812, 1999.
- [89] N. Schönborg and S. Hörnfeldt, "Model of the temperature dependence of the hysteresis losses in a high-temperature superconductor," *Physica C: Superconductivity*, vol. 372, pp. 1734 – 1738, 2002.
- [90] J. Kvitkovic, R. Hatwar, S. V. Pamidi, S. Fleshler, and C. Thieme, "Temperature dependence of critical current and transport current losses of 4 mm YBCO coated conductors manufactured using nonmagnetic substrate," *IOP Conference Series: Materials Science and Engineering*, vol. 102, p. 012033, 2015.
- [91] M. Ohmukai, T. Fujita, and T. Ohno, "The temperature dependence of critical current in YBa<sub>2</sub>Cu<sub>3</sub>O<sub>7-d</sub> thin films deposited on MgO by an eclipse PLD," *Brazilian Journal of Physics*, vol. 31, pp. 511–513, 2001.
- [92] K. Berger, J. Leveque, D. Netter, B. Douine, and A. Rezzoug, "AC transport losses calculation in a Bi-2223 current lead using thermal coupling with an analytical formula," *IEEE Transactions on Applied Superconductivity*, vol. 15, no. 2, pp. 1508–1511, 2005.
- [93] R. Brambilla, F. Grilli, and L. Martini, "Development of an edge-element model for AC loss computation of high-temperature superconductors," *Superconductor Science and Technology*, vol. 20, no. 1, pp. 16–24, 2007.
- [94] M. Zhang and T. A. Coombs, "3D modeling of high-T<sub>c</sub> superconductors by finite element software," *Superconductor Science and Technology*, vol. 25, no. 1, p. 015009, 2012.
- [95] Z. Hong, A. M. Campbell, and T. A. Coombs, "Numerical solution of critical state in superconductivity by finite element software," *Superconductor Science and Technology*, vol. 19, no. 12, pp. 1246–1252, 2006.
- [96] R. Zermeno, V. M. Sørensen, M. P. Pedersen, N. F. Mijatovic, and A. B. Abrahamsen, "Fast 2D simulation of superconductors: a multiscale approach," in *Proceedings of the COMSOL Conference Milan*. COMSOL, 2009.
- [97] F. Grilli, S. Stavrev, Y. LeFloch, M. Costa-Bouzo, E. Vinot, I. Klutsch, G. Meunier, P. Tixador, and B. Dutoit, "Finite-element method modeling of superconductors: From 2-D to 3-D," *IEEE Transactions on Applied Superconductivity*, vol. 15, no. 1, pp. 17–25, 2005.
- [98] *COMSOL Multiphysics User's Guide, 5.2a*, Comsol Inc., Burlington, USA.
- [99] V. M. R. Zermeno, A. B. Abrahamsen, N. Mijatovic, B. B. Jensen, and M. P. Sørensen, "Calculation of alternating current losses in stacks and coils made of second generation high temperature superconducting tapes for large scale applications," *Journal of Applied Physics*, vol. 114, no. 17, p. 173901, 2013.

- [100] S. Stavrev, F. Grilli, B. Dutoit, N. Nibbio, E. Vinot, I. Klutsch, G. Meunier, P. Tixador, Y. Yifeng, and E. Martinez, "Comparison of numerical methods for modeling of superconductors," *IEEE Transactions on Magnetics*, vol. 38, no. 2, pp. 849–852, 2002.
- [101] F. Grilli and P. Masson. (2015) 2-D homogeneous model to estimate AC losses in coated conductor stacks and coils. [Online]. Available: [http://www.htsmodelling.com/?page\\_id=748#2D\\_H.formulation](http://www.htsmodelling.com/?page_id=748#2D_H.formulation)
- [102] R. A. Matula, "Electrical resistivity of copper, gold, palladium, and silver," *Journal of Physical and Chemical Reference Data*, vol. 8, no. 4, pp. 1147–1298, 1979.
- [103] N. Amemiya, K. Miyamoto, S. Murasawa, H. Mukai, and K. Ohmatsu, "Finite element analysis of AC loss in non-twisted Bi-2223 tape carrying AC transport current and/or exposed to DC or AC external magnetic field," *Physica C: Superconductivity*, vol. 310, no. 1–4, pp. 30 – 35, 1998.
- [104] A. Petrov, J. Pilgrim, and I. Golosnoy, "Revisiting the homogenized domain model for fast simulation of AC transport power losses in first generation high temperature superconducting tapes and cables," *Physica C: Superconductivity and its Applications*, vol. 557, pp. 33 – 40, 2019.
- [105] S. Choi, S. J. Suh, W. Nah, Y. H. Ma, K. W. Ryu, J. H. Kim, J. Joo, M. H. Sohn, and Y. K. Kwon, "Influence of non-uniform current distribution on AC transport current loss in Bi-2223/Ag tapes," *IEEE Transactions on Applied Superconductivity*, vol. 16, no. 2, pp. 154–157, 2006.
- [106] K. Ryu, H. J. Song, H. J. Kim, and K. C. Seong, "Transport loss characteristics of the Bi-2223 tapes in an external AC magnetic field," *IEEE Transactions on Applied Superconductivity*, vol. 16, no. 2, pp. 1011–1014, 2006.
- [107] Y. H. Ma, Z. Y. Li, K. Ryu, S. Choi, K. B. Park, I. S. Oh, H. J. Song, and G. Cha, "AC loss characteristics of a cylindrical high temperature superconductor," *IEEE Transactions on Applied Superconductivity*, vol. 17, no. 2, pp. 3140–3143, 2007.
- [108] P. Seidel, *Applied Superconductivity Handbook on Devices and Applications*. Weinheim, Germany: Wiley-VCH Verlag GmbH & Co., 2015.
- [109] S. K. Olsen, C. Traeholt, A. Kuhle, O. Tonnesen, M. Daumling, and J. Ostergaard, "Loss and inductance investigations in a 4-layer superconducting prototype cable conductor," *IEEE Transactions on Applied Superconductivity*, vol. 9, no. 2, pp. 833–836, 1999.
- [110] T. Ravach. (2007) 2-D homogeneous model to estimate AC losses in coated conductor stacks and coils.
- [111] A. N. Petrov, J. A. Pilgrim, and I. O. Golosnoy, "2D finite element modelling of the AC transport power loss in multi-layer Bi-2223 cables," *Journal of Physics: Conference Series*, vol. 1559, p. 012134, 2020.
- [112] S. Sato and N. Amemiya, "Electromagnetic field analysis of YBCO coated conductors in multi-layer HTS cables," *IEEE Transactions on Applied Superconductivity*, vol. 16, no. 2, pp. 127–130, 2006.
- [113] X. Wu and B. Ni, "Longitudinal magnetic field effect in critical current characteristics of Bi-2223 superconducting tape," *Journal of Physics: Conference Series*, vol. 1054, p. 012043, 2018.
- [114] S. Honjo, M. Shimodate, Y. Takahashi, T. Masuda, H. Yumura, C. Suzawa, S. Isojima, and H. Suzuki, "Electric properties of a 66 kV 3-core superconducting power cable system," *IEEE Transactions on Applied Superconductivity*, vol. 13, no. 2, pp. 1952–1955, 2003.
- [115] K. Sung-Kyu, H. Sun-Kyoung, K. Jin-Geun, J. Bo-Geun, P. Minwon, Y. In-Keun, L. Sangjin, S. Kideok, and A. R. Kim, "Development and performance analysis of a 22.9 kV/50 MVA tri-axial HTS power cable core," *IEEE Transactions on Applied Superconductivity*, vol. 23, no. 3, pp. 5 400 804–5 400 804, 2013.
- [116] R. Bryans, "Calculation of system fault levels," SP Energy Networks, Report ESDD-02-006, 07/08/2017 2017. [Online]. Available: '<https://www.spenergynetworks.co.uk/userfiles/file/ESDD-02-006.pdf>'

- 
- [117] “IEC 60909 - Short circuit currents in three-phase a.c. systems,” IEC, Standard, 2016.
- [118] M. S. S. J. Duncan Glover, Thomas J. Overbye, *Series R-L Circuit Transients*, 6th ed. Boston, MA, USA: Cengage Learning, 2017, p. Symmetrical Faults.
- [119] S. Elschner, E. Demencik, B. Douine, F. Grilli, A. Kudymow, M. Stemmler, S. Strauss, V. Zermeno, and W. Goldacker, “New experimental method for investigating AC losses in concentric HTS power cables,” *IEEE Transactions on Applied Superconductivity*, vol. 25, no. 3, pp. 1–5, 2015.
- [120] H. Jie, T. Yuejin, W. Bin, L. Jingdong, R. Li, S. Jing, K. Wu, L. Xiaoyu, X. Ying, and W. Shu, “Thermal analysis of HTS power cable using 3-D FEM model,” *IEEE Transactions on Applied Superconductivity*, vol. 23, no. 3, pp. 5 402 404–5 402 404, 2013.
- [121] M. Furuse, S. Fuchino, K. Agatsuma, T. Masuda, M. Ohya, S. Honjo, T. Mimura, and Y. Noguchi, “Stability analysis of HTS power cable with fault currents,” *IEEE Transactions on Applied Superconductivity*, vol. 21, no. 3, pp. 1021–1024, 2011.
- [122] M. Kalsia and R. S. Dondapati, “Influence of flow rate and heat flux on the temperature distribution in long length counter flow cooled cold dielectric HTS cables,” *Physica C: Superconductivity and its Applications*, vol. 567, p. 1353549, 2019.
- [123] Z.-F. Jiang, X.-F. Gou, and T.-M. Shen, “Numerical simulation of quench initiation and propagation in multi-filamentary Bi<sub>2</sub>Sr<sub>2</sub>CaCu<sub>2</sub>O<sub>x</sub> round wires at high magnetic fields,” *Journal of Applied Physics*, vol. 125, no. 16, p. 163901, 2019.